Dynamical Systems in Neuroscience

Computational Neuroscience

Terrence J. Sejnowski and Tomaso A. Poggio, editors

Neural Nets in Electric Fish, Walter Heiligenberg, 1991

The Computational Brain, Patricia S. Churchland and Terrence J. Sejnowski, 1992

Dynamic Biological Networks: The Stomatogastric Nervous System, edited by Ronald M. Harris-Warrick, Eve Marder, Allen I. Selverston, and Maurice Maulins, 1992

The Neurobiology of Neural Networks, edited by Daniel Gardner, 1993

Large-Scale Neuronal Theories of the Brain, edited by Christof Koch and Joel L. Davis, 1994

The Theoretical Foundations of Dendritic Function: Selected Papers of Wilfrid Rall with Commentaries, edited by Idan Segev, John Rinzel, and Gordon M. Shepherd, 1995

Models of Information Processing in the Basal Ganglia, edited by James C. Houk, Joel L. Davis, and David G. Beiser, 1995

Spikes: Exploring the Neural Code, Fred Rieke, David Warland, Rob de Ruyter van Stevenick, and William Bialek, 1997

Neurons, Networks, and Motor Behavior, edited by Paul S. Stein, Sten Grillner, Allen I. Selverston, and Douglas G. Stuart, 1997

Methods in Neuronal Modeling: From Ions to Networks, second edition, edited by Christof Koch and Idan Segev, 1998

Fundamentals of Neural Network Modeling: Neuropsychology and Cognitive Neuroscience, edited by Randolph W. Parks, Daniel S. Levin, and Debra L. Long, 1998

Neural Codes and Distributed Representations: Foundations of Neural Computation, edited by Laurence Abbott and Terrence J. Sejnowski, 1999

Unsupervised Learning: Foundations of Neural Computation, edited by Geoffrey Hinton and Terrence J. Sejnowski, 1999

Fast Oscillations in Cortical Circuits, Roger D. Traub, John G.R. Jefferys, and Miles Al Whittington, 1999

Computational Vision: Information Processing in Perception and Visual Behavior, Hanspeter A. Mallot, 2000

Graphical Models: Foundations of Neural Computation, edited by Michael I. Jordan and Terrence J. Sejnowski, 2001

Self-Organizing Map Formation: Foundation of Neural Computation, edited by Klaus Obermayer and Terrence J. Sejnowski, 2001

Theoretical Neuroscience: Computational and Mathematical Modeling of Neural Systems, Peter Dayan and L. F. Abbott, 2001

Neural Engineering: Computation, Representation, and Dynamics in Neurobiological Systems, Chris Eliasmith and Charles H. Anderson, 2003

The Computational Neurobiology of Reaching and Pointing, edited by Reza Shadmehr and Steven P. Wise, 2005

Dynamical Systems in Neuroscience: The Geometry of Excitability and Bursting, Eugene M. Izhikevich, 2007

Dynamical Systems in Neuroscience:
The Geometry of Excitability and Bursting

Eugene M. Izhikevich

The MIT Press
Cambridge, Massachusetts
London, England

This book was set in LaTeX by the author. Printed and bound in the United States of America.

Library of Congress Cataloging-in-Publication Data

Izhikevich, Eugene M., 1967–
Dynamical systems in neuroscience: the geometry of excitability and bursting / Eugene M. Izhikevich.
p. cm. — (Computational neuroscience)
Includes bibliographical references and index.
ISBN 978-0-262-09043-8 (hc. : alk. paper)
1. Neural networks (Neurobiology) 2. Neurons - computer simulation. 3. Dynamical systems. 4. Computational neuroscience. I. Izhikevich, E. M. II Title. III. Series.

QP363.3.I94 2007
573.8'01'13—DC21 2006040349

10 9 8 7 6 5 4 3 2 1

To my beautiful daughters, Liz and Kate.

Contents

Preface

Historically, much of theoretical neuroscience research concerned neuronal circuits and synaptic organization. The neurons were divided into excitatory and inhibitory types, but their electrophysiological properties were largely neglected or taken to be identical to those of Hodgkin-Huxley's squid axon. The present awareness of the importance of the electrophysiology of individual neurons is best summarized by David McCormick in the fifth edition of Gordon Shepherd's book *The Synaptic Organization of the Brain*:

> Information-processing depends not only on the *anatomical* substrates of synaptic circuits but also on the *electrophysiological* properties of neurons... Even if two neurons in different regions of the nervous system possess identical morphological features, they may respond to the same synaptic input in very different manners because of each cell's intrinsic properties.
>
> McCormick (2004)

Much of present neuroscience research concerns voltage- and second-messenger-gated currents in individual cells, with the goal of understanding the cell's intrinsic neurocomputational properties. It is widely accepted that knowing the currents suffices to determine what the cell is doing and why it is doing it. This, however, contradicts a half-century–old observation that cells having similar currents can nevertheless exhibit quite different dynamics. Indeed, studying isolated axons having presumably similar electrophysiology (all are from the crustacean *Carcinus maenas*), Hodgkin (1948) injected a DC-current of varying amplitude, and discovered that some preparations could exhibit repetitive spiking with arbitrarily low frequencies, while the others discharged in a narrow frequency band. This observation was largely ignored by the neuroscience community until the seminal paper by Rinzel and Ermentrout (1989), who showed that the difference in behavior is due to different *bifurcation* mechanisms of excitability.

Let us treat the amplitude of the injected current in Hodgkin's experiments as a bifurcation parameter: When the amplitude is small, the cell is quiescent; when the amplitude is large, the cell fires repetitive spikes. When we change the amplitude of the injected current, the cell undergoes a transition from quiescence to repetitive spiking. From the dynamical systems point of view, the transition corresponds to a bifurcation from equilibrium to a limit cycle attractor. The type of bifurcation determines the most fundamental computational properties of neurons, such as the class of excitability, the existence or nonexistence of threshold, all-or-none spikes, subthreshold oscillations, the ability to generate postinhibitory rebound spikes, bistability of resting and spiking states, whether the neuron is an integrator or a resonator, and so on.

This book is devoted to a systematic study of the relationship between electrophysiology, bifurcations, and computational properties of neurons. The reader will learn why cells having nearly identical currents may undergo distinct bifurcations, and hence they will have fundamentally different neurocomputational properties. (Conversely, cells

having quite different currents may undergo identical bifurcations, and hence they will have similar neurocomputational properties.) The major message of the book can be summarized as follows (compare with the McCormick statement above):

> Information-processing depends not only on the electrophysiological properties of neurons but also on their *dynamical properties*. Even if two neurons in the same region of the nervous system possess similar electrophysiological features, they may respond to the same synaptic input in very different manners because of each cell's bifurcation dynamics.

Nonlinear dynamical system theory is a core of computational neuroscience research, but it is not a standard part of the graduate neuroscience curriculum. Neither is it taught in most math/physics departments in a form suitable for a general biological audience. As a result, many neuroscientists fail to grasp such fundamental concepts as equilibrium, stability, limit cycle attractor, and bifurcations, even though neuroscientists constantly encounter these nonlinear phenomena.

This book introduces dynamical systems starting with simple one- and two-dimensional spiking models and continuing all the way to bursting systems. Each chapter is organized from simple to complex, so everybody can start reading the book; only the reader's background will determine where he or she stops. The book emphasizes the geometrical approach, so there are few equations but a lot of figures. Half of them are simulations of various neural models, so there are hundreds of possible exercises such as "Use MATLAB (GENESIS, NEURON, XPPAUT, etc.) and parameters in the caption of figure X to simulate the figure." Additional problems are provided at the end of each chapter; the reader is encouraged to solve at least some of them and to look at the solutions of the others at the end of the book. Problems marked [**M.S.**] or [**Ph.D.**] are suggested thesis topics.

Acknowledgments. I thank the scientists who reviewed the first draft of the book: Pablo Achard, Jose M. Amigo, Vlatko Becanovic, Brent Doiron, George Bard Ermentrout, Richard FitzHugh, David Golomb, Andrei Iacob, Paul Kulchenko, Maciej Lazarewicz, Georgi Medvedev, John Rinzel, Anil K. Seth, Gautam C Sethia, Arthur Sherman, Klaus M. Stiefel, and Takashi Tateno. I also thank the anonymous referees who peer-reviewed the book and made quite a few valuable suggestions instead of just rejecting it. Special thanks go to Niraj S. Desai, who made most of the in vitro recordings used in the book (the data are available on the author's Web page `www.izhikevich.com`), and to Bruno van Swinderen, who drew the cartoons. I enjoyed the hospitality of The Neurosciences Institute – a monastery of interdisciplinary science – and I benefited greatly from the expertise and support of its fellows.

Finally, I thank my wife, Tatyana, and my wonderful daughters, Elizabeth and Kate, for their support and patience during the five-year gestation of this book.

Eugene M. Izhikevich `www.izhikevich.com`
San Diego, California December 19, 2005

Chapter 1

Introduction

This chapter highlights some of the most important concepts developed in the book. First, we discuss several common misconceptions regarding the spike generation mechanism of neurons. Our goal is to motivate the reader to think of a neuron not only in terms of ions and channels, as many biologists do, and not only in terms of an input/output relationship, as many theoreticians do, but also as a nonlinear dynamical system that looks at the input through the prism of its own intrinsic dynamics. We ask such questions as "What makes a neuron fire?" or "Where is the threshold?", and then outline the answers, using the geometrical theory of dynamical systems.

From a dynamical systems point of view, neurons are excitable because they are near a transition, called bifurcation, from resting to sustained spiking activity. While there is a huge number of possible ionic mechanisms of excitability and spike generation, there are only four bifurcation mechanisms that can result in such a transition. Considering the geometry of phase portraits at these bifurcations, we can understand many computational properties of neurons, such as the nature of threshold and all-or-none spiking, the coexistence of resting and spiking states, the origin of spike latencies, postinhibitory spikes, and the mechanism of integration and resonance. Moreover, we can understand how these properties are interrelated, why some are equivalent, and why some are mutually exclusive.

1.1 Neurons

If somebody were to put a gun to the head of the author of this book and ask him to name the single most important concept in brain science, he would say it is the concept of a *neuron*. There are only 10^{11} or so neurons in the human brain, much fewer than the number of non-neural cells such as glia. Yet neurons are unique in the sense that only they can transmit electrical signals over long distances. From the neuronal level we can go down to cell biophysics and to the molecular biology of gene regulation. From the neuronal level we can go up to neuronal circuits, to cortical structures, to the whole brain, and finally to the behavior of the organism. So let us see how much we understand of what is going on at the level of individual neurons.

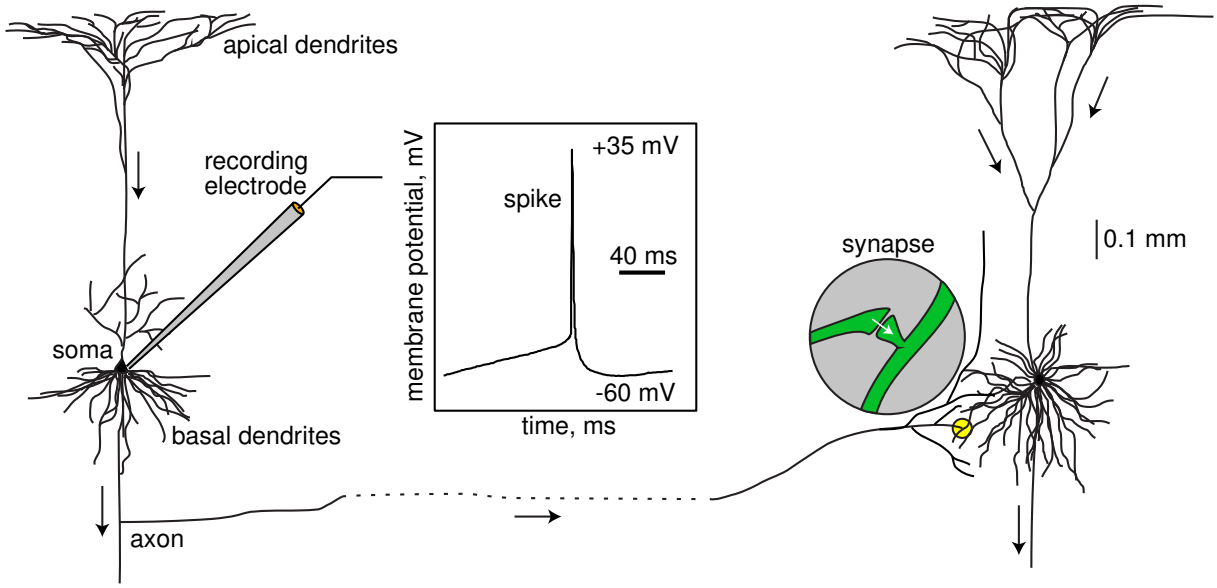

Figure 1.1: Two interconnected cortical pyramidal neurons (hand drawing) and in vitro recorded spike.

1.1.1 What Is a Spike?

A typical neuron receives inputs from more than $10,000$ other neurons through the contacts on its dendritic tree called synapses; see Fig.1.1. The inputs produce electrical transmembrane currents that change the membrane potential of the neuron. Synaptic currents produce changes, called postsynaptic potentials (PSPs). Small currents produce small PSPs; larger currents produce significant PSPs that can be amplified by the voltage-sensitive channels embedded in the neuronal membrane and lead to the generation of an *action potential* or *spike* – an abrupt and transient change of membrane voltage that propagates to other neurons via a long protrusion called an axon.

Such spikes are the main means of communication between neurons. In general, neurons do not fire on their own; they fire as a result of incoming spikes from other neurons. One of the most fundamental questions of neuroscience is *What, exactly, makes neurons fire?* What is it in the incoming pulses that elicits a response in one neuron but not in another? Why can two neurons have different responses to exactly the same input and identical responses to completely different inputs? To answer these questions, we need to understand the dynamics of spike generation mechanisms of neurons.

Most introductory neuroscience books describe neurons as integrators with a threshold: neurons sum incoming PSPs and "compare" the integrated PSP with a certain voltage value, called the firing threshold. If it is below the threshold, the neuron remains quiescent; when it is above the threshold, the neuron fires an all-or-none spike, as in Fig.1.3, and resets its membrane potential. To add theoretical plausibility to this argument, the books refer to the Hodgkin-Huxley model of spike generation in squid

Figure 1.2: What makes a neuron fire?

giant axons, which we study in chapter 2. The irony is that the Hodgkin-Huxley model does not have a well-defined threshold; it does not fire all-or-none spikes; and it is not an integrator, but a resonator (i.e., it prefers inputs having certain frequencies that resonate with the frequency of subthreshold oscillations of the neuron). We consider these and other properties in detail in this book.

1.1.2 Where Is the Threshold?

Much effort has been spent trying to experimentally determine the firing thresholds of neurons. Here, we challenge the classical view of a threshold. Let us consider two typical experiments, depicted in Fig.1.4, that are designed to measure the threshold. in Fig.1.4a, we shock a cortical neuron (i.e., we inject brief but strong pulses of current of various amplitudes to depolarize the membrane potential to various values). Is there a clear-cut voltage value, as in Fig.1.3, above which the neuron fires but below which no spikes occur? If you find one, let the author know! In Fig.1.4b we inject long but weak pulses of current of various amplitudes, which results in slow depolarization and a spike. The firing threshold, if it exists, must be somewhere in the shaded region, but where? Where does the slow depolarization end and the spike start? Is it meaningful to talk about firing thresholds at all?

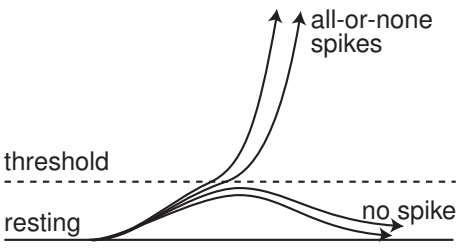

Figure 1.3: The concept of a firing threshold.

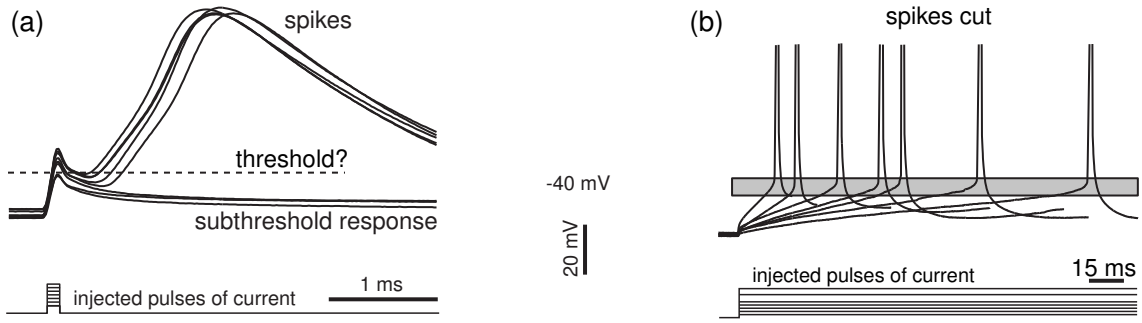

Figure 1.4: Where is the firing threshold? Shown are in vitro recordings of two layer 5 rat pyramidal neurons. Notice the differences of voltage and time scales.

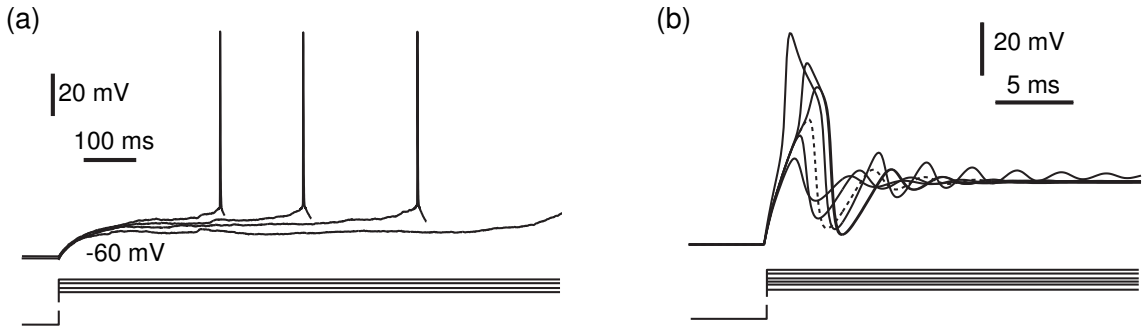

Figure 1.5: Where is the rheobase (i.e., the minimal current that fires the cell)? (a) in vitro recordings of the pyramidal neuron of layer 2/3 of a rat's visual cortex show increasing latencies as the amplitude of the injected current decreases. (b) Simulation of the $I_{\mathrm{Na,p}}$+I_{K} −model (pronounced: *persistent sodium plus potassium model*) shows spikes of graded amplitude.

Perhaps, we should measure current thresholds instead of voltage thresholds. The current threshold (i.e., the minimal amplitude of injected current of infinite duration needed to fire a neuron) is called the *rheobase*. In Fig.1.5 we decrease the amplitudes of injected pulses of current to find the minimal one that still elicits a spike or the maximal one that does not. In Fig.1.5a, progressively weaker pulses result in longer latencies to the first spike. Eventually the neuron does not fire because the latency is longer than the duration of the pulse, which is 1 second in the figure. Did we really measure the neuronal rheobase? What if we waited a bit longer? How long is long enough? In Fig.1.5b the latencies do not grow, but the spike amplitudes decrease until the spikes do not look like spikes at all. To determine the current threshold, we need to draw the line and separate spike responses from "subthreshold" ones. How can we do that if the spikes are not all-or-none? Is the response denoted by the dashed line a spike?

Risking adding more confusion to the notion of a threshold, consider the following. If excitatory inputs depolarize the membrane potential (i.e., bring it closer to

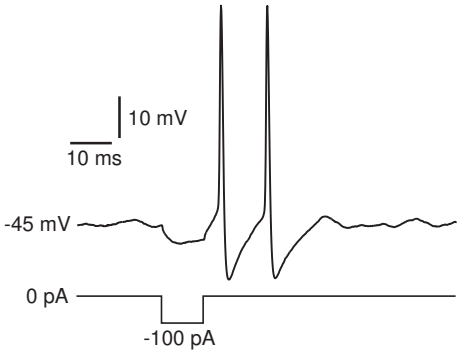

Figure 1.6: In vitro recording of rebound spikes of a rat's brainstem mesV neuron in response to a brief hyperpolarizing pulse of current.

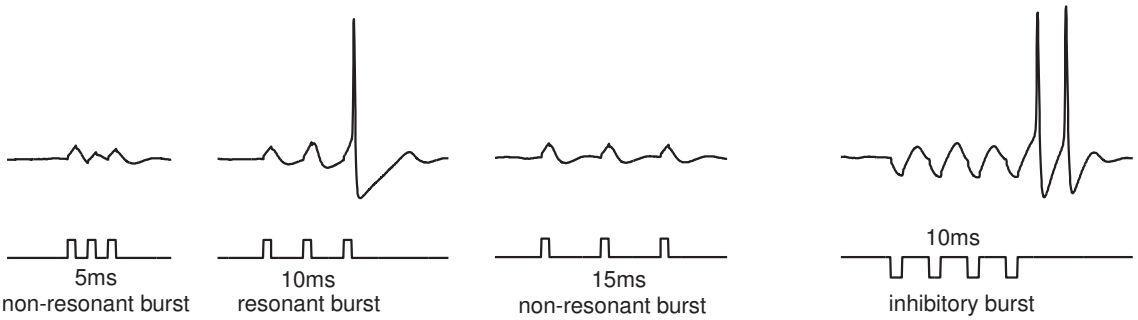

Figure 1.7: Resonant response of the mesencephalic V neuron of a rat's brainstem to pulses of injected current having a 10 ms period (in vitro).

the "firing threshold"), and inhibitory inputs hyperpolarize the potential and move it away from the threshold, then *how can the neuron in Fig.1.6 fire in response to the inhibitory input?* This phenomenon, also observed in the Hodgkin-Huxley model, is called anodal break excitation, rebound spike, or postinhibitory spike. Many biologists say that rebound responses are due to the activation and inactivation of certain slow currents, which bring the membrane potential over the threshold or, equivalently, lower the threshold upon release from the hyperpolarization – a phenomenon called a low-threshold spike in thalamocortical neurons. The problem with this explanation is that neither the Hodgkin-Huxley model nor the neuron in Fig.1.6 has these currents, and even if they did, the hyperpolarization is too short and too weak to affect the currents.

Another interesting phenomenon is depicted in Fig.1.7. The neuron is stimulated with brief pulses of current mimicking an incoming burst of three spikes. When the stimulation frequency is high (5 ms period), presumably reflecting a strong input, the neuron does not fire at all. However, stimulation with a lower frequency (10 ms period) that resonates with the frequency of subthreshold oscillation of the neuron evokes a spike response, regardless of whether the stimulation is excitatory or inhibitory. Stimulation with even lower frequency (15 ms period) cannot elicit spike response again. Thus, the neuron is sensitive only to the inputs having resonant frequency. The same pulses applied to a cortical pyramidal neuron evoke a response only in the first case (small period), but not in the other cases.

1.1.3 Why Are Neurons Different, and Why Do We Care?

Why would two neurons respond completely differently to the same input? A biologist would say that the response of a neuron depends on many factors, such as the type of voltage- and Ca^{2+}-gated channels expressed by the neuron, the morphology of its dendritic tree, the location of the input, and other factors. These factors are indeed important, but they do not determine the neuronal response per se. Rather they determine the rules that govern dynamics of the neuron. Different conductances and currents can result in the same rules, and hence in the same responses; conversely, similar currents can result in different rules and in different responses. The currents define what kind of dynamical system the neuron is.

We study ionic transmembrane currents in chapter 2. In subsequent chapters we investigate how the types of currents determine neuronal dynamics. We divide all currents into two major classes: amplifying and resonant, with the persistent Na^+ current $I_{Na,p}$ and the persistent K^+ current I_K being the typical examples of the former and the latter, respectively. Since there are tens of known currents, purely combinatorial argument implies that there are millions of different electrophysiological mechanisms of spike generation. We will show later that any such mechanism must have at least one amplifying and one resonant current. Some mechanisms, called minimal in this book, have one resonant and one amplifying current. They provide an invaluable tool in classifying and understanding the electrophysiology of spike generation.

Many illustrations in this book are based on simulations of the reduced $I_{Na,p} + I_K$-model (pronounced *persistent sodium plus potassium model*), which consists of a fast persistent Na^+ (amplifying) current and a slower persistent K^+ (resonant) current. It is equivalent to the famous and widely used Morris-Lecar $I_{Ca}+I_K$-model (Morris and Lecar 1981). We show that the model exhibits quite different dynamics, depending on the values of the parameters, e.g., the half-activation voltage of the K^+ current: in one case, it can fire in a narrow frequency range, it can exhibit coexistence of resting and spiking states, and it has damped subthreshold oscillations of membrane potential. In another case, it can fire in a wide frequency range and show no coexistence of resting and spiking and no subthreshold oscillations. Thus, seemingly inessential differences in parameter values could result in drastically distinct behaviors.

1.1.4 Building Models

To build a good model of a neuron, electrophysiologists apply different pharmacological blockers to tease out the currents that the neuron has. Then they apply different stimulation protocols to measure the kinetic parameters of the currents, such as the Boltzmann activation function, time constants, and maximal conductances. We consider all these functions in chapter 2. Next, they create a Hodgkin-Huxley-type model and simulate it using the NEURON, GENESIS, or XPP environment or MATLAB (the first two are invaluable tools for simulating realistic dendritic structures).

The problem is that the parameters are measured in different neurons and then put together into a single model. As an illustration, consider two neurons having the same

Figure 1.8: Neurons are dynamical systems.

currents, say $I_{\mathrm{Na,p}}$ and I_{K}, and exhibiting excitable behavior; that is, both neurons are quiescent but can fire a spike in response to a stimulation. Suppose the second neuron has stronger $I_{\mathrm{Na,p}}$, which is balanced by stronger I_{K}. If we measure Na^+ conductance using the first neuron and K^+ conductance using the second neuron, the resulting $I_{\mathrm{Na,p}} + I_{\mathrm{K}}$-model will have an excess of K^+ current and probably will not be able to fire spikes at all. Conversely, if we measure Na^+ and K^+ conductances using the second neuron and then the first neuron, respectively, the model would have too much Na^+ current and probably would exhibit sustained pacemaking activity. In any case, the model fails to reproduce the excitable behavior of the neurons whose parameters we measured.

Some of the parameters cannot be measured at all, so many arbitrary choices are made via a process called "fine-tuning". Navigating in the dark, possibly with the help of some biological intuition, the researcher modifies parameters, compares simulations with experiment, and repeats this trial-and-error procedure until he or she is satisfied with the results. Since seemingly similar values of parameters can result in drastically different behaviors, and quite different parameters can result in seemingly similar behaviors, how do we know that the resulting model is correct? How do we know that its behavior is equivalent to that of the neuron we want to study? And what is *equivalent* in this case? Now, you are primed to consider dynamical systems. If not, see Fig.1.8.

1.2 Dynamical Systems

In chapter 2 we introduce the Hodgkin-Huxley formalism to describe neuronal dynamics in terms of activation and inactivation of voltage-gated conductances. An important result of the Hodgkin-Huxley studies is that *neurons are dynamical systems*, so they should be studied as such. Below we mention some of the important concepts of dynamical systems theory. The reader does not have to follow all the details of this section because the concepts are explained in greater detail in subsequent chapters.

A dynamical system consists of a set of variables that describe its state and a law that describes the evolution of the state variables with time (i.e., how the state of the system in the next moment of time depends on the input and its state in the previous moment of time). The Hodgkin-Huxley model is a four-dimensional dynamical system because its state is uniquely determined by the membrane potential, V, and so-called gating variables n, m, and h for persistent K^+ and transient Na^+ currents. The evolution law is given by a four-dimensional system of ordinary differential equations.

Typically, all variables describing neuronal dynamics can be classified into four classes, according to their function and the time scale.

1. *Membrane potential*.

2. *Excitation variables*, such as activation of a Na^+ current. These variables are responsible for the upstroke of the spike.

3. *Recovery variables*, such as inactivation of a Na^+ current and activation of a fast K^+ current. These variables are responsible for the repolarization (downstroke) of the spike.

4. *Adaptation variables*, such as activation of slow voltage- or Ca^{2+}-dependent currents. These variables build up during prolonged spiking and can affect excitability in the long run.

The Hodgkin-Huxley model does not have variables of the fourth type, but many neuronal models do, especially those exhibiting bursting dynamics.

1.2.1 Phase Portraits

The power of the dynamical systems approach to neuroscience, as well as to many other sciences, is that we can tell something, or many things, about a system without knowing all the details that govern the system evolution. We do not even use equations to do that! Some may even wonder why we call it a mathematical theory.

As a start, let us consider a quiescent neuron whose membrane potential is resting. From the dynamical systems point of view, there are no changes of the state variables of such a neuron; hence it is at an equilibrium point. All the inward currents that depolarize the neuron are balanced, or equilibrated, by the outward currents that hyperpolarize it. If the neuron remains quiescent despite small disturbances and membrane noise, as in Fig.1.9a (top), then we conclude that the equilibrium is stable. Isn't

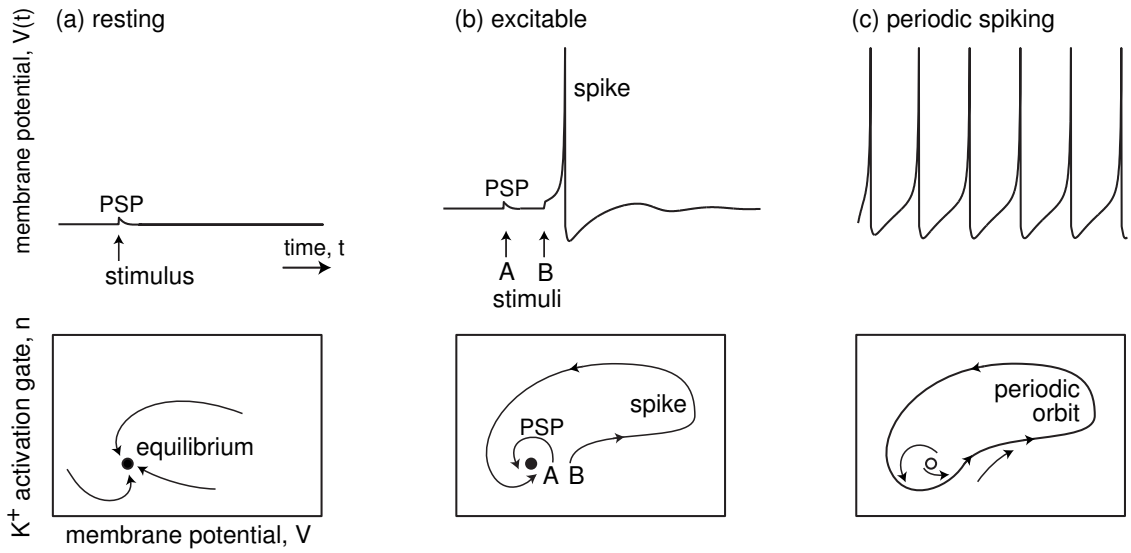

Figure 1.9: Resting, excitable, and periodic spiking activity correspond to a stable equilibrium (a and b) or limit cycle (c), respectively.

it amazing that we can reach such a conclusion without knowing the equations that describe the neuron's dynamics? We do not even know the number of variables needed to describe the neuron; it could be infinite, for all we care.

In this book we introduce the notions of equilibria, stability, threshold, and attraction domains using one- and two-dimensional dynamical systems, e.g., the $I_{\mathrm{Na,p}}$+I_{K}-model with instantaneous Na^+ kinetics. The state of this model is described by the membrane potential, V, and the activation variable, n, of the persistent K^+ current, so it is a two-dimensional vector (V, n). Instantaneous activation of the Na^+ current is a function of V, so it does not result in a separate variable of the model. The evolution of the model is a trajectory $(V(t), n(t))$ on the $V \times n-$plane. Depending on the initial point, the system can have many trajectories, such as those depicted in Fig.1.9a (bottom). Time is not explicitly present in the figure, but units of time may be thought of as plotted along each trajectory. All of the trajectories in the figure are attracted to the stable equilibrium denoted by the black dot, called an *attractor*. The overall qualitative description of dynamics can be obtained through the study of the *phase portrait* of the system, which depicts certain special trajectories (equilibria, separatrices, limit cycles) that determine the topological behavior of all the other trajectories in the phase space. Probably 50 percent of illustrations in this book are phase portraits.

A fundamental property of neurons is *excitability*, illustrated in Fig.1.9b. The neuron is resting, i.e., its phase portrait has a stable equilibrium. Small perturbations, such as A, result in small excursions from the equilibrium, denoted as PSP (postsynaptic potential). Larger perturbations, such as B, are amplified by the neuron's intrinsic dynamics and result in the spike response. To understand the dynamic mechanism of such amplification, we need to consider the geometry of the phase portrait near the resting equilibrium, i.e., in the region where the decision to fire or not to fire is made.

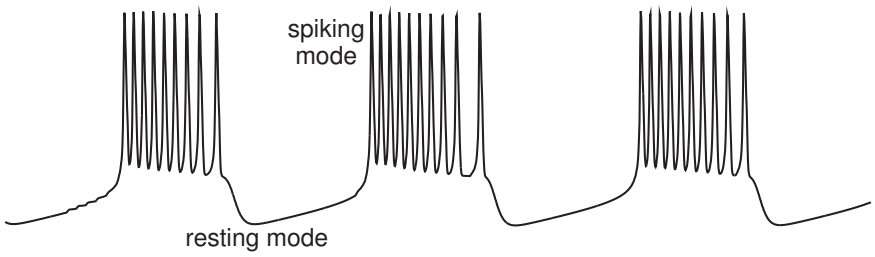

Figure 1.10: Rhythmic transitions between resting and spiking modes result in bursting behavior.

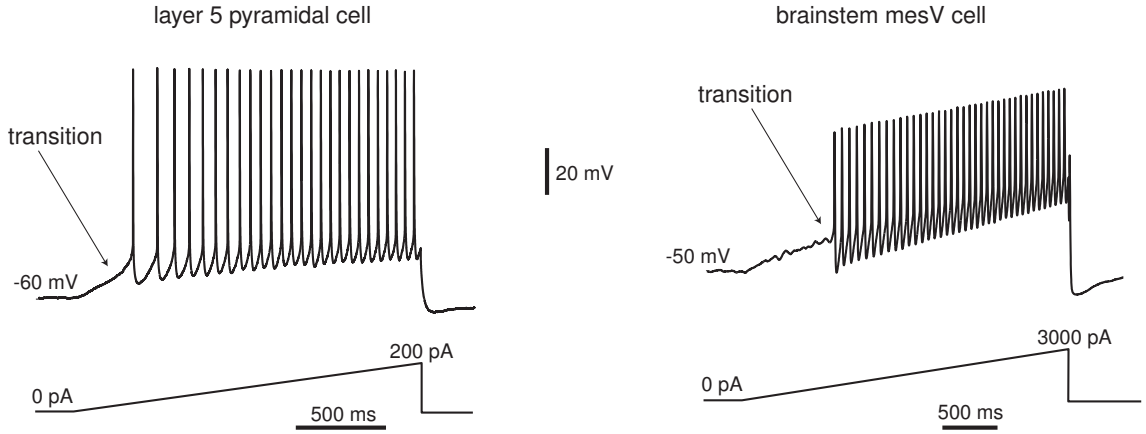

Figure 1.11: As the magnitude of the injected current slowly increases, the neurons bifurcate from resting (equilibrium) mode to tonic spiking (limit cycle) mode.

If we inject a sufficiently strong current into the neuron, we bring it to a pacemaking mode, so that it exhibits periodic spiking activity, as in Fig.1.9c. From the dynamical systems point of view, the state of such a neuron has a stable limit cycle, also known as a stable periodic orbit. The electrophysiological details of the neuron (i.e., the number and the type of currents it has, their kinetics, etc.) determine only the location, the shape, and the period of the limit cycle. As long as the limit cycle exists, the neuron can have periodic spiking activity. Of course, equilibria and limit cycles can coexist, so a neuron can be switched from one mode to another by a transient input. The famous example is the permanent extinguishing of ongoing spiking activity in the squid giant axon by a brief transient depolarizing pulse of current applied at a proper phase (Guttman et al. 1980) – a phenomenon predicted by John Rinzel (1978) purely on the basis of theoretical analysis of the Hodgkin-Huxley model. The transition between resting and spiking modes could be triggered by intrinsic slow conductances, resulting in the bursting behavior in Fig.1.10.

1.2.2 Bifurcations

Now suppose that the magnitude of the injected current is a parameter that we can control, e.g., we can ramp it up, as in Fig.1.11. Each cell in the figure is quiescent at the beginning of the ramps, so its phase portrait has a stable equilibrium and it may look like the one in Fig.1.9a or Fig.1.9b. Then it starts to fire tonic spikes, so its phase portrait has a limit cycle attractor and it may look like the one in Fig.1.9c, with a white circle denoting an unstable resting equilibrium. Apparently there is some intermediate level of injected current that corresponds to the transition from resting to sustained spiking, i.e., from the phase portrait in Fig.1.9b to Fig.1.9c. What does the transition look like?

From the dynamical systems point of view, the transition corresponds to a *bifurcation* of neuron dynamics, i.e., a qualitative change of phase portrait of the system. For example, there is no bifurcation going from the phase portrait in Fig.1.9a to that in Fig.1.9b, since both have one globally stable equilibrium; the difference in behavior is quantitative but not qualitative. In contrast, there is a bifurcation going from Fig.1.9b to Fig.1.9c, since the equilibrium is no longer stable and another attractor, limit cycle, has appeared. The neuron is not excitable in Fig.1.9a but it is in Fig.1.9b, simply because the former phase portrait is far from the bifurcation and the latter is near.

In general, neurons are excitable *because* they are near bifurcations from resting to spiking activity, so the type of the bifurcation determines the excitable properties of the neuron. Of course, the type depends on the neuron's electrophysiology. An amazing observation is that there could be millions of different electrophysiological mechanisms of excitability and spiking, but there are only four – yes, *four* – different types of bifurcations of equilibrium that a system can undergo without any additional constraints, such as symmetry. Thus, considering these four bifurcations in a general setup, we can understand excitable properties of many models, even those that have not been invented yet. What is even more amazing, we can understand excitable properties of neurons whose currents are not measured and whose models are not known, provided we can experimentally identify which of the four bifurcations the resting state of the neuron undergoes.

The four bifurcations are summarized in Fig.1.12, which plots the phase portrait before (left), at (center), and after (right) a particular bifurcation occurs. Mathematicians refer to these bifurcations as being of codimension-1 because we need to vary only one parameter, e.g., the magnitude of the injected DC current I, to observe the bifurcations reliably in simulations or experiments. There are many more codimension-2, 3, (etc.), bifurcations, but they need special conditions to be observed. We discuss these in chapter 6.

Let us consider the four bifurcations and their phase portraits in Fig.1.12. The horizontal and vertical axes are the membrane potential with instantaneous activation variable and a recovery variable, respectively. At this stage, the reader is not required to fully understand the intricacies of the phase portraits in the figure, since they will be explained systematically in later chapters.

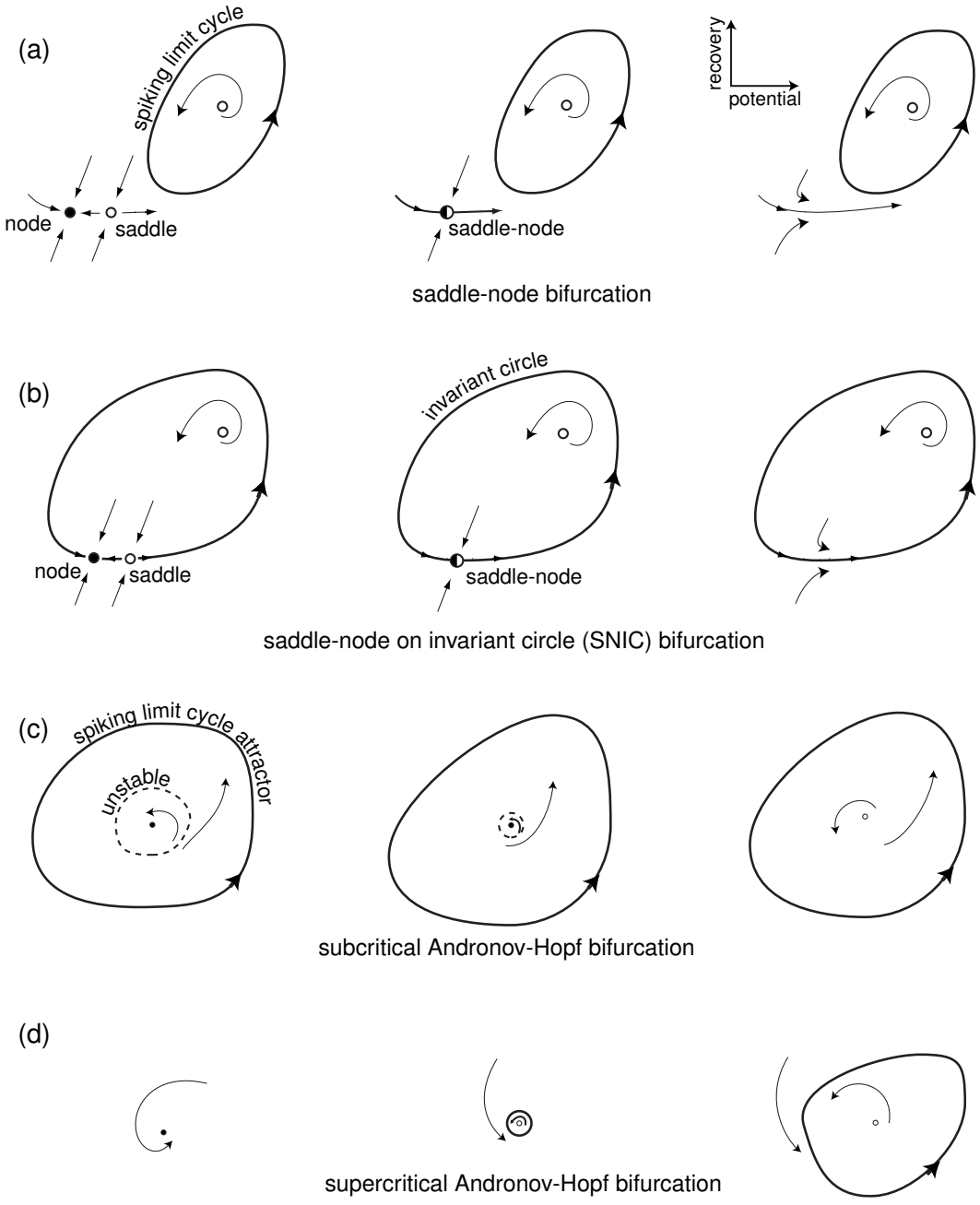

Figure 1.12: Four generic (codimension-1) bifurcations of an equilibrium state leading to the transition from resting to periodic spiking behavior in neurons.

- *Saddle-node bifurcation.* As the magnitude of the injected current or any other bifurcation parameter changes, a stable equilibrium corresponding to the resting state (black circle marked "node" in Fig.1.12a) is approached by an unstable equilibrium (white circle marked "saddle"); they coalesce and annihilate each other, as in Fig.1.12a (middle). Since the resting state no longer exists, the trajectory describing the evolution of the system jumps to the limit cycle attractor, indicating that the neuron starts to fire tonic spikes. Notice that the limit cycle, or some other attractor, must coexist with the resting state in order for the transition resting → spiking to occur.

- *Saddle-node on invariant circle bifurcation* is similar to the saddle-node bifurcation except that there is an invariant circle at the moment of bifurcation, which then becomes a limit cycle attractor, as in Fig.1.12b.

- *Subcritical Andronov-Hopf bifurcation.* A small unstable limit cycle shrinks to a stable equilibrium and makes it lose stability, as in Fig.1.12c. Because of instabilities, the trajectory diverges from the equilibrium and approaches a large-amplitude spiking limit cycle or some other attractor.

- *Supercritical Andronov-Hopf bifurcation.* The stable equilibrium loses stability and gives birth to a small-amplitude limit cycle attractor, as in Fig.1.12d. As the magnitude of the injected current increases, the amplitude of the limit cycle increases and it becomes a full-size spiking limit cycle.

Notice that there is a coexistence of resting and spiking states in the case of saddle-node and subcritical Andronov-Hopf bifurcations, but not in the other two cases. Such a coexistence reveals itself via a hysteresis behavior when the injected current slowly increases and then decreases past the bifurcation value, because the transitions "resting → spiking" and "spiking → resting" occur at different values of the current. In addition, brief stimuli applied at the appropriate times can switch the activity from spiking to resting and back. There are also spontaneous noise-induced transitions between the two modes that result in the stuttering spiking that, for instance, is exhibited by the so-called fast spiking (FS) cortical interneurons when they are kept close to the bifurcation (Tateno et al. 2004). Some bistable neurons have a slow adaptation current that activates during the spiking mode and impedes spiking, often resulting in bursting activity.

Systems undergoing Andronov-Hopf bifurcations, whether subcritical or supercritical, exhibit damped oscillations of membrane potential, whereas systems near saddle-node bifurcations, whether on or off an invariant circle, do not. The existence of small amplitude oscillations creates the possibility of resonance to the frequency of the incoming pulses, as in Fig.1.7, and other interesting features.

We refer to neurons with damped subthreshold oscillations as *resonators* and to those that do not have this property as *integrators*. We refer to the neurons that exhibit the coexistence of resting and spiking states, at least near the transition from

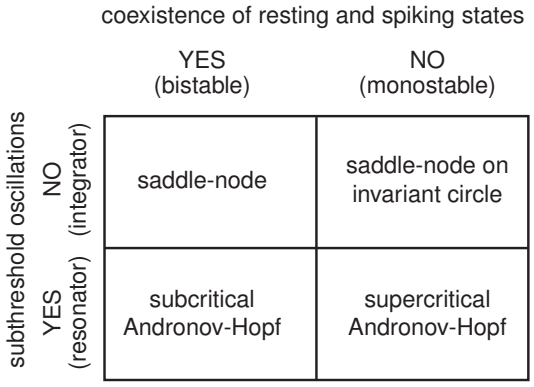

Figure 1.13: Classification of neurons into monostable/bistable integrators/resonators according to the bifurcation of the resting state in Fig.1.12.

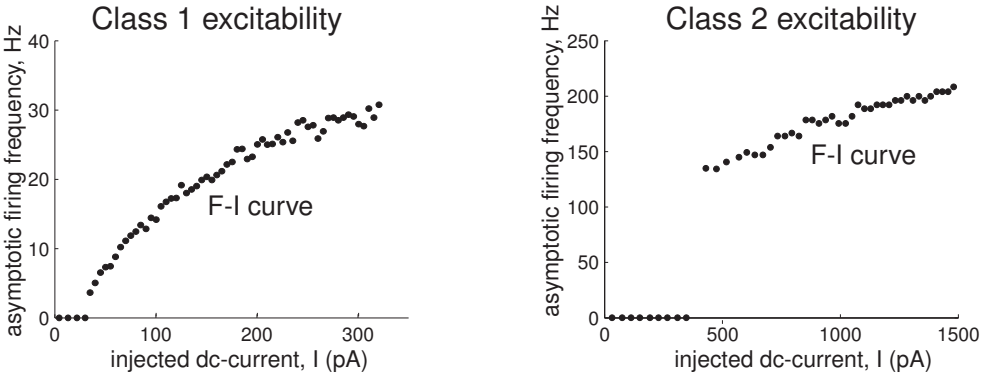

Figure 1.14: Frequency-current (F-I) curves of cortical pyramidal neuron and brainstem mesV neuron from Fig.7.3. These are the same neurons used in the ramp experiment in Fig.1.11.

resting to spiking, as *bistable*, and to those that do not, *monostable*. The four bifurcations in Fig.1.12 are uniquely defined by these two features. For example, a bistable resonator is a neuron undergoing subcritical Andronov-Hopf bifurcation, and a monostable integrator is a neuron undergoing saddle-node on invariant circle bifurcation (see Fig.1.13). Cortical fast spiking (FS) and regular spiking (RS) neurons, studied in chapter 8, are typical examples of the former and the latter, respectively.

1.2.3 Hodgkin Classification

Hodgkin (1948) was the first to study bifurcations in neuronal dynamics, years before the mathematical theory of bifurcations was developed. He stimulated squid axons with pulses of various amplitudes and identified three classes of responses:

- *Class 1 neural excitability.* Action potentials can be generated with arbitrarily low frequency, depending on the strength of the applied current.

- *Class 2 neural excitability.* Action potentials are generated in a certain frequency band that is relatively insensitive to changes in the strength of the applied current.

- *Class 3 neural excitability.* A single action potential is generated in response to a pulse of current. Repetitive (tonic) spiking can be generated only for extremely strong injected currents or not at all.

The qualitative distinction between the classes is that the frequency-current relation (the F-I curve in Fig.1.14) starts from zero and continuously increases for Class 1 neurons, is discontinuous for Class 2 neurons, and is not defined at all for Class 3 neurons.

Obviously, neurons belonging to different classes have different neurocomputational properties. Class 1 neurons, which include cortical excitatory pyramidal neurons, can smoothly encode the strength of the input into the output firing frequency, as in Fig.1.11 (left). In contrast, Class 2 neurons, such as fast-spiking (FS) cortical inhibitory interneurons, cannot do that; instead, they fire in a relatively narrow frequency band, as in Fig.1.11 (right). Class 3 neurons cannot exhibit sustained spiking activity, so Hodgkin regarded them as "sick" or "unhealthy". There are other distinctions between the classes, which we discuss later.

Different classes of excitability occur because neurons have different bifurcations of resting and spiking states – a phenomenon first explained by Rinzel and Ermentrout (1989). If ramps of current are injected to measure the F-I curves, then Class 1 excitability occurs when the neuron undergoes the saddle-node bifurcation on an invariant circle depicted in Fig.1.12b. Indeed, the period of the limit cycle attractor is infinite at the bifurcation point, and then it decreases as the bifurcation parameter – say, the magnitude of the injected current – increases. The other three bifurcations result in Class 2 excitability. Indeed, the limit cycle attractor exists and has a finite period when the resting state in Fig.1.12 undergoes a subcritical Andronov-Hopf bifurcation, so emerging spiking has a nonzero frequency. The period of the small limit cycle attractor appearing via supercritical Andronov-Hopf bifurcation is also finite, so the frequency of oscillations is nonzero, but their amplitudes are small. In contrast to the common and erroneous folklore, the saddle-node bifurcation (off-limit cycle) also results in Class 2 excitability because the limit cycle has a finite period at the bifurcation. There is a considerable latency (delay) to the first spike in this case, but the subsequent spiking has nonzero frequency. Thus, the simple scheme "Class 1 = saddle-node, Class 2 = Hopf" that permeates many publications is unfortunately incorrect.

When pulses of current are used to measure the F-I curve, as in Hodgkin's experiments, the firing frequency depends on factors besides the type of the bifurcation of the resting state. In particular, low-frequency firing can be observed in systems near Andronov-Hopf bifurcations, as we show in chapter 7. To avoid possible confusion, we define the class of excitability only on the basis of slow ramp experiments.

Hodgkin's classification has an important historical value, but it is of little use for the dynamic description of a neuron, since naming a class of excitability of a neuron does not tell much about the bifurcations of the resting state. Indeed, it says only that saddle-node on invariant circle bifurcation (Class 1) is different from the other three bifurcations (Class 2), and only when ramps are injected. Dividing neurons into

integrators and resonators with bistable or monostable activity is more informative, so we adopt the classification in Fig.1.13 in this book. In this classification, a Class 1 neuron is a monostable integrator, whereas a Class 2 neuron can be a bistable integrator or a resonator.

1.2.4 Neurocomputational properties

Using the same arrangement as in Fig.1.13, we depict typical geometry of phase portraits near the four bifurcations in Fig.1.15. Let us use the portraits to explain what happens "near the threshold", i.e., near the place where the decision to fire or not to fire is made. To simplify our geometrical analysis, we assume here that neurons receive shock inputs, i.e., brief but strong pulses of current that do not change the phase portraits, but only push or reset the state of the neuron into various regions of the phase space. We consider these and other cases in detail in chapter 7.

The horizontal axis in each plot in Fig.1.15 corresponds to the membrane potential V with instantaneous Na^+ current, and the vertical axis corresponds to a recovery variable, say activation of K^+ current. Black circles denote stable equilibria corresponding to the neuronal resting state. Spiking limit cycle attractors correspond to sustained spiking states, which exist in the two cases depicted in the left half of the figure corresponding to the bistable dynamics. The limit cycles are surrounded by shaded regions – their attraction domains. The white region is the attraction domain of the equilibrium. To initiate spiking, the external input should push the state of the system into the shaded region, and to extinguish spiking, the input should push the state back into the white region.

There are no limit cycles in the two cases depicted in the right half of the figure, so the entire phase space is the attraction domain of the stable equilibrium, and the dynamics are monostable. However, if the trajectory starts in the shaded region, it makes a large-amplitude rotation before returning to the equilibrium – a transient spike. Apparently, to elicit such a spike, the input should push the state of the system into the shaded region.

Now let us contrast the upper and lower halves of the figure, corresponding to integrators and resonators, respectively. We distinguish these two modes of operation on the basis of the existence of subthreshold oscillations near the equilibrium.

First, let us show that *inhibition impedes spiking in integrators, but can promote it in resonators.* In the integrator, the shaded region is in the depolarized voltage range, i.e., to the right of the equilibrium. Excitatory inputs push the state of the system toward the shaded region, while inhibitory inputs push it away. In resonators, both excitation and inhibition push the state toward the shaded region, because the region wraps around the equilibrium and can be reached along any direction. This explains the rebound spiking phenomenon depicted in Fig.1.6.

Integrators have all-or-none spikes; resonators may not. Indeed, any trajectory starting in the shaded region in the upper half of Fig.1.15 has to rotate around the

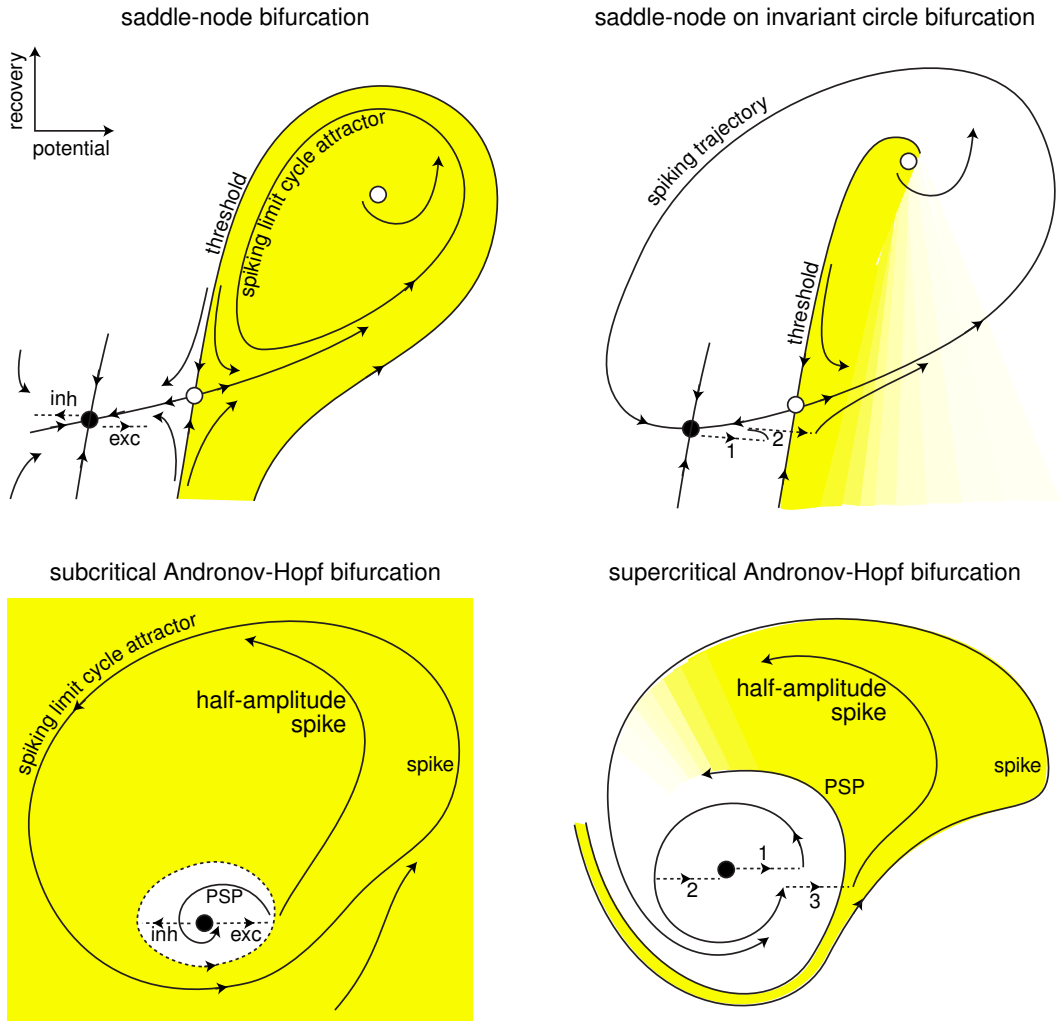

Figure 1.15: The geometry of phase portraits of excitable systems near four bifurcations can explain many neurocomputational properties (see section 1.2.4 for details).

white circle at the top that corresponds to an unstable equilibrium. Moreover, the state of the system is quickly attracted to the spiking trajectory and moves along that trajectory, thereby generating a stereotypical spike. A resonator neuron also can fire large amplitude spikes when its state is pushed to or beyond the trajectory denoted "spike". Such neurons generate subthreshold responses when the state slides along the smaller trajectory denoted PSP; they also can generate spikes of an intermediate amplitude when the state is pushed between the PSP and "spike" trajectories, which explains the partial-amplitude spiking in Fig.1.5b or in the squid axon in Fig.7.26. The set of initial conditions corresponding to such spiking is quite small, so typical spikes have large amplitudes and partial spikes are rare.

Integrators have well-defined thresholds; resonators may not. The white circles near the resting states of integrators in Fig.1.15 are called saddles. They are stable along the

vertical direction and unstable along the horizontal direction. The two trajectories that lead to the saddle along the vertical direction are called separatrices because they separate the phase space into two regions – in this case, white and shaded. The separatrices play the role of thresholds since only those perturbations that push the state of the system beyond them result in a spike. The closer the state of the system is to the separatrices, the longer it takes to converge and then diverge from the saddle, resulting in a long *latency to the spike*. Notice that the threshold is not a point, but a tilted curve that spans a range of voltage values.

Resonators have a well-defined threshold in the case of subcritical Andronov-Hopf bifurcation: it is the small unstable limit cycle that separates the attraction domains of stable equilibrium and spiking limit cycle. Trajectories inside the small cycle spiral toward the stable equilibrium, whereas trajectories outside the cycle spiral away from it and eventually lead to sustained spiking activity. When a neuronal model is far from the subcritical Andronov-Hopf bifurcation, its phase portrait may look similar to the one corresponding to the supercritical Andronov-Hopf bifurcation. The narrow shaded band in the figure is not a threshold manifold but a fuzzy threshold set called "quasi-threshold" by FitzHugh (1955). Many resonators, including the Hodgkin-Huxley model, have quasi-thresholds instead of thresholds. The width of the quasi-threshold in the Hodgkin-Huxley model is so narrow that for all practical reasons it may be assumed to be just a curve.

Integrators integrate, resonators resonate. Now consider inputs consisting of multiple pulses, e.g., a burst of spikes. Integrators prefer high-frequency inputs; the higher the frequency, the sooner they fire. Indeed, the first spike of such an input, marked "1" in the top-right phase portrait in Fig.1.15, increases the membrane potential and shifts the state to the right, toward the threshold. Since the state of the system is still in the white area, it slowly converges back to the stable equilibrium. To cross the threshold manifold, the second pulse must arrive shortly after the first one. The reaction of a resonator to a pair of pulses is quite different. The first pulse initiates a damped subthreshold oscillation of the membrane potential, which looks like a spiral in the bottom-right phase portrait in Fig.1.15. The effect of the second pulse depends on its timing. If it arrives after the trajectory makes half a rotation, marked "2" in the figure, it cancels the effect of the first pulse. If it arrives after the trajectory makes a full rotation, marked "3" in the figure, it adds to the first pulse and either increases the amplitude of subthreshold oscillation or evokes a spike response. Thus, the response of the resonator neuron depends on the frequency content of the input, as in Fig.1.7.

Integrators and resonators constitute two major modes of activity of neurons. Most cortical pyramidal neurons, including the regular spiking (RS), intrinsically bursting (IB), and chattering (CH) types considered in Chap. 8, are integrators. So are thalamocortical neurons in the relay mode of firing, and neostriatal spiny projection neurons. Most cortical inhibitory interneurons, including the FS type, are resonators. So are brainstem mesencephalic V neurons and stellate neurons of the entorhinal cortex. Some cortical pyramidal neurons and low-threshold spiking (LTS) interneurons can be at the border of transition between integrator and resonator modes. Such a transition corre-

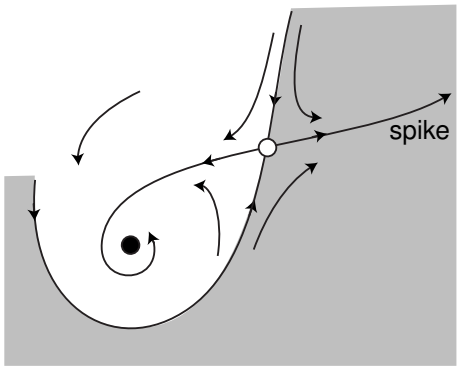

Figure 1.16: Phase portrait of a system near a Bogdanov-Takens bifurcation that corresponds to the transition from integrator to resonator mode.

sponds to another bifurcation, which has codimension-2, and hence it is less likely to be encountered experimentally. We consider this and other uncommon bifurcations in detail later. The phase portrait near the bifurcation is depicted in Fig.1.16, and it is a good exercise for the reader to explain why such a system has damped oscillations and postinhibitory responses, yet a well-defined threshold, all-or-none spikes, and possibly long latencies.

Of course, figures 1.15 and 1.16 cannot encompass all the richness of neuronal behavior, otherwise this book would be only 19pages long (this book is actually quite short; most of the space is taken by figures, exercises, and solutions). Many aspects of neuronal dynamics depend on other bifurcations, e.g., those corresponding to appearance and disappearance of spiking limit cycles. These bifurcations describe the transitions from spiking to resting, and they are especially important when we consider bursting activity. In addition, we need to take into account the relative geometry of equilibria, limit cycles, and other relevant trajectories, and how they depend on the parameters of the system, such as maximal conductances, and activation time constants. We explore all these issues systematically in subsequent chapters.

In chapter 2 we review some of the most fundamental concepts of neuron electrophysiology, culminating with the Hodgkin-Huxley model. This chapter is aimed at mathematicians learning neuroscience. In chapters 3 and 4 we use one- and two-dimensional neuronal models, respectively, to review some of the most fundamental concepts of dynamical systems, such as equilibria, limit cycles, stability, attraction domain, nullclines, phase portrait, and bifurcation. The material in these chapters, aimed at biologists learning the language of dynamical systems, is presented with the emphasis on geometrical rather than mathematical intuition. In fact, the spirit of the entire book is to explain concepts by using pictures, not equations. Chapter 5 explores phase portraits of various conductance-based models and the relations between ionic currents and dynamic behavior. In Chapter 6 we use the $I_{\mathrm{Na,p}}$+I_{K}-model to systematically introduce the geometric bifurcation theory. Chapter 7, probably the most important chapter of the book, applies the theory to explain many computational properties of neurons. In fact, all the material in the previous chapters is given so that the reader can understand this chapter. In chapter 8 we use a simple phenomenological

model to simulate many cortical, hippocampal, and thalamic neurons. This chapter contains probably the most comprehensive up-to-date review of various firing patterns exhibited by mammalian neurons. In chapter 9 we introduce the electrophysiological and topological classification of bursting dynamics, as well as some useful methods to study the bursters. Finally, the last and the most mathematically advanced chapter of the book, Chap. 10, deals with coupled neurons. There we show how the details of the spike generation mechanism of neurons affect neurons' collective properties, such as synchronization.

1.2.5 Building Models (Revisited)

To have a good model of a neuron, it is not enough to put the right kind of currents together and tune the parameters so that the model can fire spikes. It is not even enough to reproduce the right input resistance, rheobase, and firing frequencies. The model has to reproduce all the neurocomputational features of the neuron, starting with the coexistence of resting and spiking states, spike latencies, subthreshold oscillations, and rebound spikes, among others.

A good way to start is to determine what kind of bifurcations the neuron under consideration undergoes and how the bifurcations depend on neuromodulators and pharmacological blockers. Instead of or in addition to measuring neuronal responses to get the kinetic parameters, we need to measure them to get the right bifurcation behavior. Only in this case we can be sure that the behavior of the model is *equivalent* to that of the neuron, even if we omitted a current or guessed some of the parameters incorrectly.

Implementation of this research program is still a pipe dream. The people who understand the mathematical aspects of neuron dynamics – those who see beyond conductances and currents – usually do not have the opportunity to do experiments. Conversely, those who study neurons in vitro or in vivo on a daily basis – those who see spiking, bursting, and oscillations; those who can manipulate the experimental setup to test practically any aspect of neuronal activity – do not usually see the value of studying phase portraits, bifurcations, and nonlinear dynamics in general. One of the goals of this book is to change this state and bring these two groups of people closer together.

Review of Important Concepts

- Neurons are dynamical systems.
- The resting state of neurons corresponds to a stable equilibrium; the tonic spiking state corresponds to a limit cycle attractor.
- Neurons are excitable because the equilibrium is near a bifurcation.
- There are many ionic mechanisms of spike generation, but only four generic bifurcations of equilibria.
- These bifurcations divide neurons into four categories: integrators or resonators, monostable or bistable.
- Analyses of phase portraits at bifurcations explain why some neurons have well-defined thresholds, all-or-none spikes, postinhibitory spikes, frequency preference, hysteresis, and so on, while others do not.
- These features, and not ionic currents per se, determine the neuronal responses, i.e., the kind of computations neurons do.
- A good neuronal model must reproduce not only electrophysiology but also the bifurcation dynamics of neurons.

Bibliographical Notes

Richard FitzHugh at the National Institutes of Health (NIH) pioneered the phase plane analysis of neuronal models with the view to understanding their neurocomputational properties. He was the first to analyze the Hodgkin-Huxley model (FitzHugh 1955; years before they received the Nobel Prize) and to prove that it has neither threshold nor all-or-none spikes. FitzHugh (1961) introduced the simplified model of excitability (see Fig.1.18) and showed that one can get the right kind of neuronal dynamics in models lacking conductances and currents. Nagumo et al. (1962) designed a corresponding tunnel diode circuit, so the model is called the FitzHugh-Nagumo oscillator. Chapter 8 deals with such simplified models. The history of the development of FitzHugh-Nagumo model is reviewed by Izhikevich and FitzHugh (2006).

FitzHugh's research program was further developed by John Rinzel and G. Bard Ermentrout (see Fig.1.19 and Fig.1.20). In their 1989 seminal paper, Rinzel and Ermentrout revived Hodgkin's classification of excitability and pointed out the connection between the behavior of neuronal models and the bifurcations they exhibit. (They also referred to the excitability as "type I" or "type II"). Unfortunately, many people treat

Figure 1.17: Richard FitzHugh in 1984.

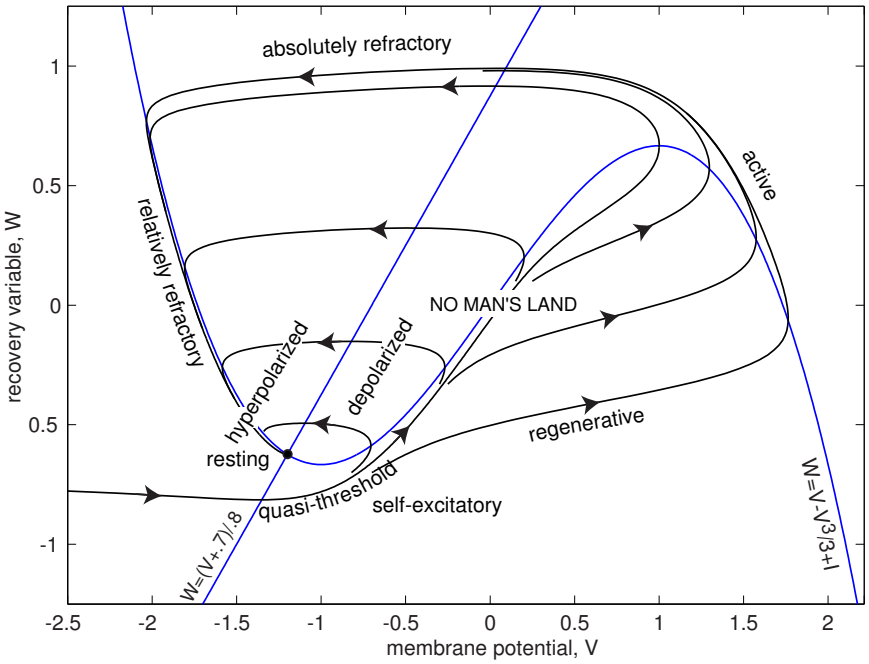

Figure 1.18: Phase portrait and physiological state diagram of FitzHugh-Nagumo model $\dot{V} = V - V^3/3 - W + I$, $\dot{W} = 0.08(V + 0.7 - 0.8W)$. The meaning of curves and trajectories is explained in chapter 4. (Reproduced from Izhikevich and FitzHugh (2006) with permission.)

Figure 1.19: John Rinzel in 2004. Depicted on his T-shirt is the cover of the first issue of *Journal of Computational Neuroscience*, in which the Pinsky-Rinzel (1994) model appeared.

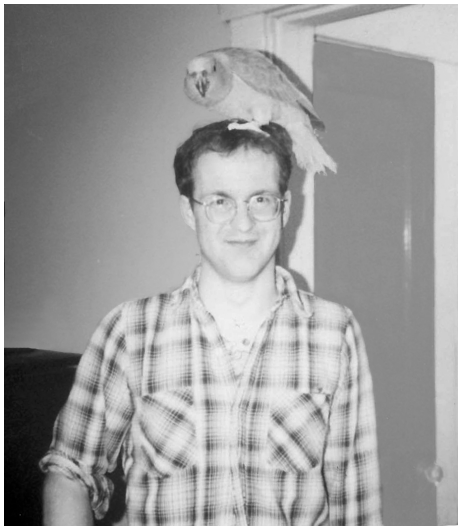

Figure 1.20: G. Bard Ermentrout (G. stands for George) with his parrot, Junior, in 1983.

the connection in a simpleminded fashion and incorrectly identify "type I = saddle-node, type II = Hopf". If only life were so simple!

The geometrical analysis of neuronal models was further developed by, among others, Izhikevich (2000a), who stressed the integrator and resonator modes of operation and made connections to other neurocomputational properties.

The neuroscience and mathematics parts of this book are standard, though many connections are new. The literature sources are listed at the end of each chapter. Among many outstanding books on computational neuroscience, the author especially recommends *Spikes, Decisions, and Actions* by Wilson (1999), *Biophysics of Computation* by Koch (1999), *Theoretical Neuroscience* by Dayan and Abbott (2001), and *Foundations of Cellular Neurophysiology* by Johnston and Wu (1995). The present volume complements these excellent books in the sense that it is more ambitious, focused, and thorough in dealing with neurons as dynamical systems. Though its views may be biased by the author's philosophy and taste, the payoffs in understanding neuronal dynamics are immense, provided the reader has enough patience and perseverance to follow the author's line of thought.

The NEURON simulation environment is described by Hines (1989) and Carnevale and Hines (2006) (`http://www.neuron.yale.edu`); the GENESIS environment, by Bower and Beeman (1995) (`http://www.genesis-sim.org`); the XPP environment, by Ermentrout (2002). The author of this book uses MATLAB, which has become a standard computational tool in science and engineering. MATLAB is the registered trademark of The MathWorks, Inc. (`http://www.mathworks.com`).

Index

Chapter 10

Synchronization (www.izhikevich.com)

This chapter is available at `www.izhikevich.com`. It supplements the book by Izhikevich E. M. (2007) *Dynamical Systems in Neuroscience: The Geometry of Excitability and Bursting*, Cambridge, Mass: MIT Press. The author's Web site also contains MATLAB programs and in vitro data used in the book. To cite this chapter, write (Izhikevich 2007, Chapter 10) in your papers (i.e., as if it were a printed part of the book).

In this chapter we consider networks of tonically spiking neurons. Like any other kind of physical, chemical, or biological oscillators, such neurons can synchronize and exhibit collective behavior that is not intrinsic to any individual neuron. For example, partial synchrony in cortical networks is believed to generate various brain oscillations, such as the alpha and gamma EEG rhythms. Increased synchrony may result in pathological types of activity, such as epilepsy. Coordinated synchrony is needed for locomotion and swim pattern generation in fish. There is an ongoing debate on the role of synchrony in neural computation, see e.g., the special issue of *Neuron* (September 1999) devoted to the binding problem.

Depending on the circumstances, synchrony can be good or bad, and it is important to know what factors contribute to synchrony and how to control it. This is the subject of the present chapter – the most advanced chapter of the book. It provides a nice application of the theory developed earlier and hopefully gives some insight into why the previous chapters may be worth mastering.

Our goal is to understand how the behavior of two coupled neurons depends on their intrinsic dynamics. First, we introduce the method of description of an oscillation by its phase. Then, we describe various methods of reduction of coupled oscillators to simple phase models. The reduction method and the exact form of the phase model depend on the type of coupling (i.e., whether it is pulsed, weak, or slow) and on the type of bifurcation of the limit cycle attractor generating tonic spiking. Finally, we show how to use phase models to understand the collective dynamics of many coupled

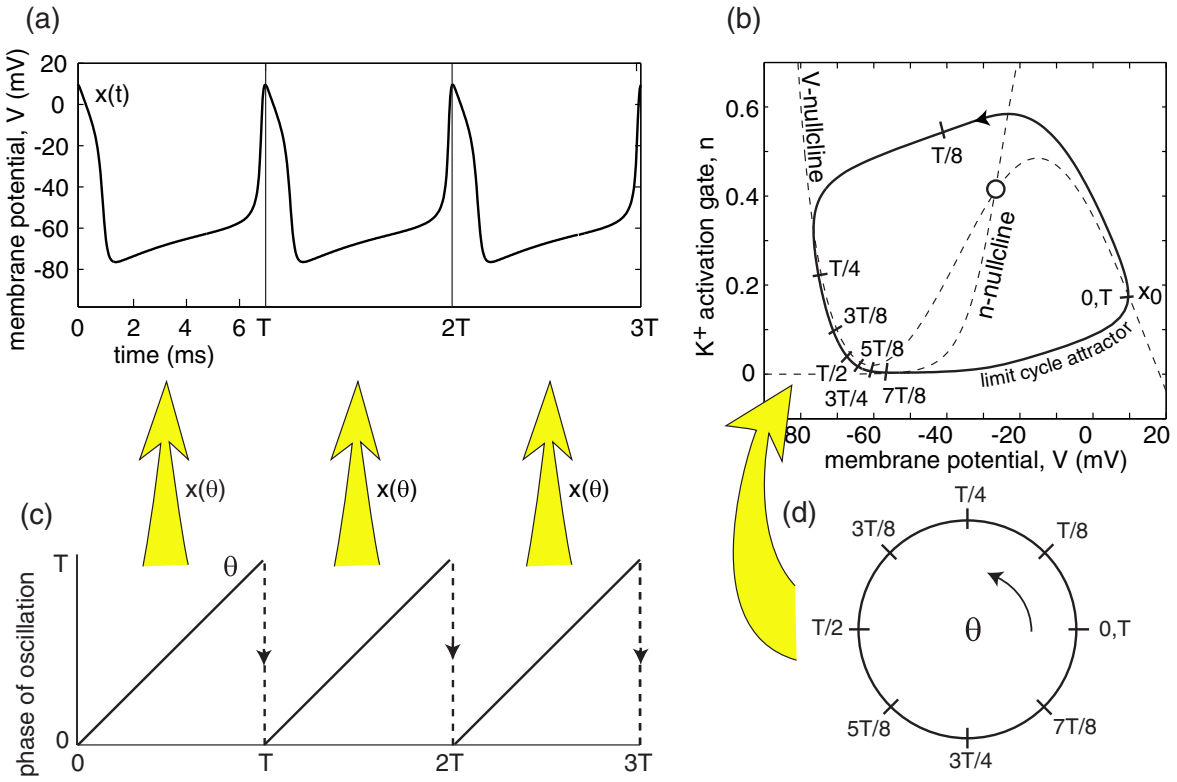

Figure 10.1: Definition of a phase of oscillation, ϑ, in the $I_{\rm Na} + I_{\rm K}$-model with parameters as in Fig.4.1a and $I = 10$.

oscillators.

10.1 Pulsed Coupling

In this section we consider oscillators of the form

$$\dot{x} = f(x) + A\delta(t - t_{\rm s}) \,, \qquad x \in \mathbb{R}^m, \tag{10.1}$$

having exponentially stable limit cycles and experiencing pulsed stimulation at times $t_{\rm s}$ that instantaneously increases the state variable by the constant A. The Dirac delta function $\delta(t)$ is a mathematical shorthand notation for resetting x by A. The strength of pulsed stimulation, A, is not assumed to be small. Most of the results of this section can also be applied to the case in which the action of the input pulse is not instantaneous, but smeared over an interval of time, typically shorter than the period of oscillation.

10.1.1 Phase of Oscillation

Many types of physical, chemical, and biological oscillators share an astonishing feature: they can be described by a single phase variable ϑ. In the context of tonic spiking, the

phase is usually taken to be the time since the last spike, as in Fig.10.1a.

We say that a function $x(t)$ is periodic if there is a constant $T > 0$ such that $x(t + T) = x(t)$ for any t. The minimal value of the constant is the period of $x(t)$. Periodic functions appear in dynamical systems having limit cycle attractors.

The notion of the phase of oscillation is related to the notion of parametrization of a limit cycle attractor, as in Fig.10.1b. Take a point x_0 on the attractor and plot the trajectory $x(t)$ with $x(0) = x_0$. Then the phase of $x(t)$ is $\vartheta = t$. As t increases past the period T, then $2T$, an so on, the phase variable ϑ wraps around the interval $[0, T]$, jumping from T to 0; see Fig.10.1c. Gluing together the points 0 and T, as in Fig.10.1d, we can treat the interval $[0, T]$ as a circle, denoted as $\mathbb{S}^1$, with circumference T. The parametrization is the mapping of $\mathbb{S}^1$ in Fig.10.1d into the phase space $\mathbb{R}^2$ in Fig.10.1b, given by $\vartheta \mapsto x(\vartheta)$.

We could put the initial point x_0 corresponding to the zero phase anywhere else on the limit cycle, and not necessarily at the peak of the spike. The choice of the initial point introduces an ambiguity in parameterizing the phase of oscillation. Different parametrizations, however, are equivalent up to a constant phase shift (i.e., translation in time). In the rest of the chapter, ϑ always denotes the phase of oscillation, the parameter T denotes the period of oscillation, and $\vartheta = 0$ corresponds to the peak of the spike unless stated otherwise. If the system has two or more coexisting limit cycle attractors, then a separate phase variable needs to be defined for each attractor.

10.1.2 Isochrons

The phase of oscillation can also be introduced outside the limit cycle. Consider, for example, point y_0 in Fig.10.2 (top). Since the trajectory $y(t)$ is not on a limit cycle, it is not periodic. However, it approaches the cycle as $t \to +\infty$. Hence, there is some point x_0 on the limit cycle, not necessarily the closest to y_0, such that

$$y(t) \to x(t) \quad \text{as} \quad t \to +\infty \,. \tag{10.2}$$

Now take the phase of the nonperiodic solution $y(t)$ to be the phase of its periodic proxy $x(t)$.

Alternatively, we can consider a point on the limit cycle x_0 and find all the other points y_0 that satisfy (10.2). The set of all such points is called *the stable manifold* of x_0. Since any solution starting on the stable manifold has an asymptotic behavior indistinguishable from that of $x(t)$, its phase is the same as that of $x(t)$. For this reason, the manifold represents solutions having equal phases, and it is often referred to as being the *isochron* of x_0 (*iso*, equal; *chronos*, time, in Greek), a notion going back to Bernoulli and Leibniz.

Every point on the plane in Fig.10.2, except the unstable equilibrium, gives rise to a trajectory that approaches the limit cycle. Therefore, every point has some phase. Let $\vartheta(x)$ denote the phase of the point x. Then, isochrons are level contours of the function $\vartheta(x)$, since the function is constant on each isochron.

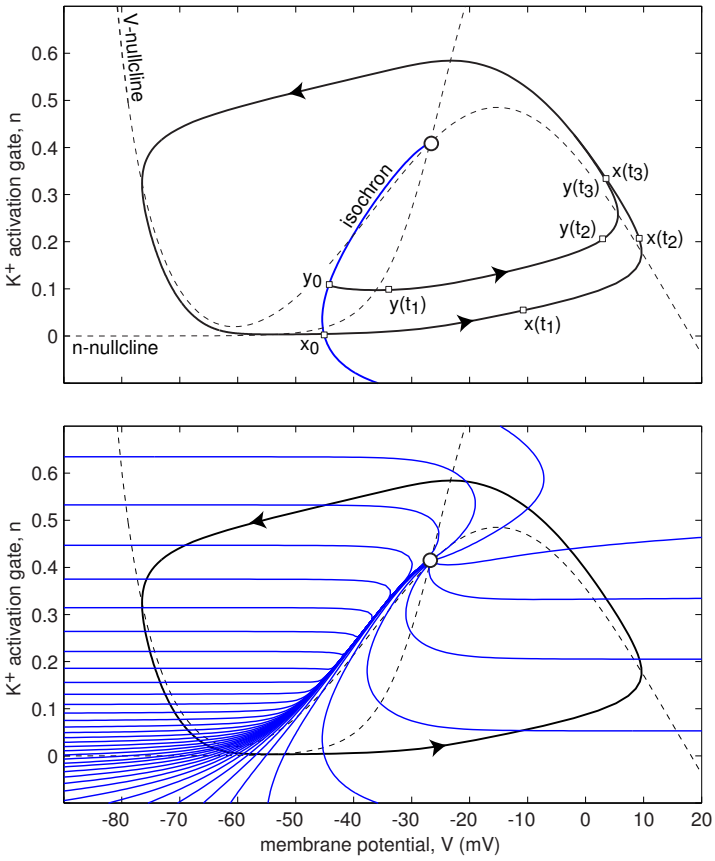

Figure 10.2: Top. An isochron, or a stable manifold, of a point x_0 on the limit cycle attractor is the set of all initial conditions y_0 such that $y(t) \to x(t)$ as $t \to +\infty$. Bottom. Isochrons of the limit cycle attractor in Fig.10.1 corresponding to 40 evenly distributed phases $nT/40$, $n = 1, \ldots, 40$.

The entire plane is foliated by isochrons. We depict only 40 representative ones in Fig.10.2. In this chapter we consider neighborhoods of exponentially stable limit cycles, where the foliation is continuous and invariant (Guckenheimer 1975):

- *Continuity.* The function $\vartheta(x)$ is continuous so that nearby points have nearby phases.
- *Invariance.* If $\vartheta(x(0)) = \vartheta(y(0))$, then $\vartheta(x(t)) = \vartheta(y(t))$ for all t. Isochrons are mapped to isochrons by the flow of the vector field.

Fig.10.3 shows the geometry of isochrons of various oscillators. The Andronov-Hopf oscillator in the figure is often called a radial isochron clock for the obvious reason. It is simple enough to be solved explicitly (see exercise 1). In general, finding isochrons is a daunting mathematical task. In exercise 3 we present a MATLAB program that finds isochrons numerically.

10.1.3 PRC

Consider a periodically spiking neuron (10.1) receiving a single brief pulse of current that increases the membrane potential by $A = 1$ mV, as in Fig.10.4 (left). Such a perturbation may not elicit an immediate spike, but it can change the timing, that is,

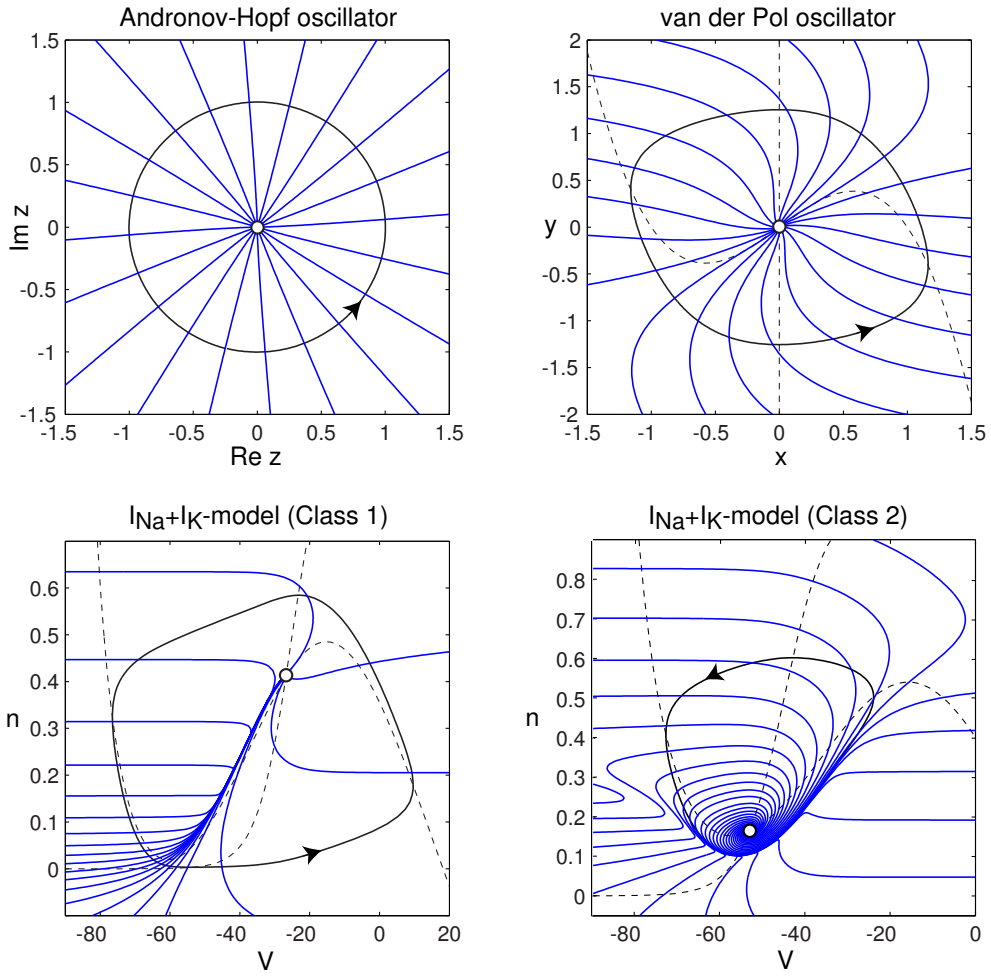

Figure 10.3: Isochrons of various oscillators. Andronov-Hopf oscillator: $\dot{z} = (1+\mathrm{i})z - z|z|^2$, $z \in \mathbb{C}$. van der Pol oscillator: $\dot{x} = x - x^3 - y$, $\dot{y} = x$. The $I_{\mathrm{Na}} + I_{\mathrm{K}}$-model with parameters as in Fig.4.1a and $I = 10$ (Class 1) and $I = 35$ (Class 2). Only isochrons corresponding to phases $nT/20$, $n = 1, \ldots, 20$, are shown.

the phase, of the following spikes. For example, the perturbed trajectory (solid line in Fig.10.4, left) fires earlier than the free-running unperturbed trajectory (dashed line). That is, right after the perturbation, the phase, ϑ_{new}, is greater than the old phase, ϑ. The magnitude of the phase shift of the spike train depends on the exact timing of the stimulus relative to the phase of oscillation ϑ. Stimulating the neuron at different phases, we can measure the *phase response curve* (also called phase-resetting curve PRC, or spike time response curve STRC)

$$\mathrm{PRC}\,(\vartheta) = \{\vartheta_{\mathrm{new}} - \vartheta\} \qquad (\text{shift} = \text{new phase} - \text{old phase})\ ,$$

depicted in Fig.10.4, right. Positive (negative) values of the function correspond to phase advances (delays) in the sense that they advance (delay) the timing of the next spike.

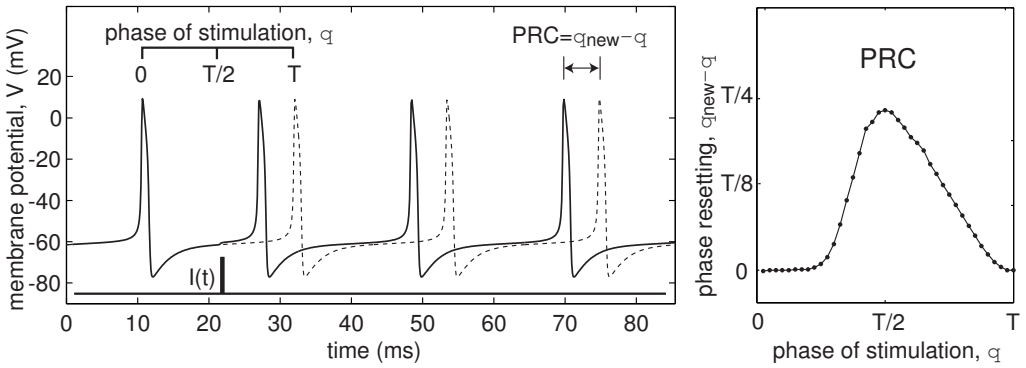

Figure 10.4: Phase response of the $I_{\rm Na}+I_{\rm K}$-model with parameters as in Fig.4.1a and $I=4.7$. The dashed voltage trace is the free-running trajectory.

In contrast to the common folklore, the function PRC(ϑ) can be measured for an arbitrary stimulus, not necessarily weak or brief. The only caveat is that to measure the new phase of oscillation perturbed by a stimulus, we must wait long enough for transients to subside. This becomes a limiting factor when PRCs are used to study synchronization of oscillators to periodic pulses, as we do in section 10.1.5.

There is a simple geometrical relationship between the structure of isochrons of an oscillator and its PRC, illustrated in Fig.10.5 (see also exercise 6). Let us stimulate the oscillator at phase ϑ with a pulse, which moves the trajectory from point x lying on the intersection of isochron ϑ and the limit cycle attractor to a point y lying on some isochron $\vartheta_{\rm new}$. From the definition of PRC, it follows that $\vartheta_{\rm new}=\vartheta+PRC(\vartheta)$.

In general, one uses simulations to determine PRCs, as we do in Fig.10.4. Using

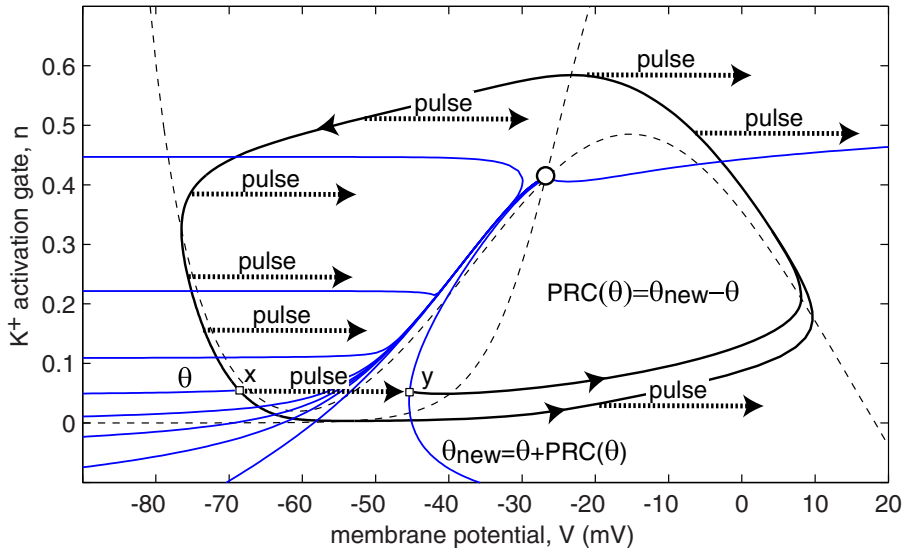

Figure 10.5: The geometrical relationship between isochrons and the phase response curve (PRC) of the $I_{\rm Na}+I_{\rm K}$-oscillator in Fig.10.1.

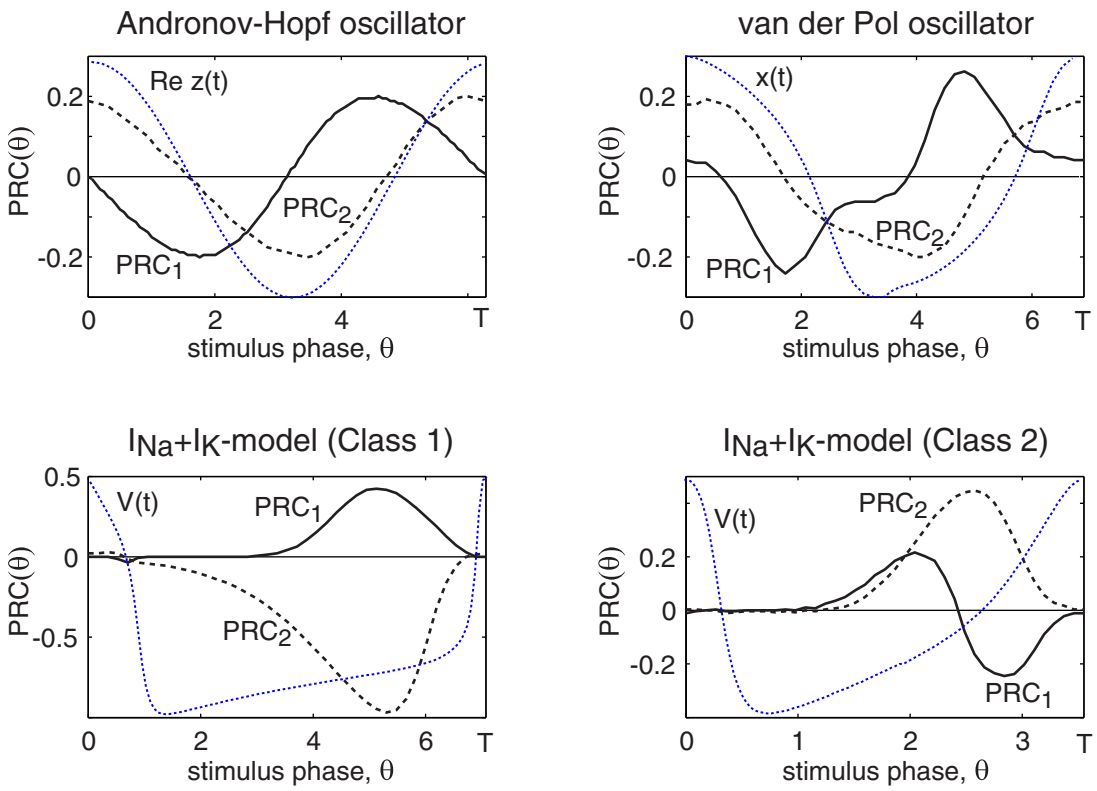

Figure 10.6: Examples of phase response curves (PRC) of the oscillators in Fig.10.3. $\mathrm{PRC}_1(\vartheta)$: Horizontal pulses (along the first variable) with amplitudes $0.2, 0.2, 2, 0.2$ for Andnronov-Hopf, van der Pol, Class 1 and Class 2 oscillators, respectively. $\mathrm{PRC}_2(\vartheta)$: Vertical pulses (along the second variable) with amplitudes $0.2, 0.2, 0.02, 0.002$, respectively. An example of oscillation is plotted as a dotted curve in each subplot (not to scale).

the MATLAB program presented in exercise 5, we can determine PRCs of all four oscillators in Fig.10.3 and plot them in Fig.10.6. It is a good exercise to explain the shape of each PRC in the figure, or at least its sign, using the geometry of isochrons of corresponding oscillators. In section 10.2.4 we discuss pitfalls of using the straightforward method in Fig.10.4 to measure PRCs in biological neurons, and we present a better technique.

Note that the PRC of the $I_{\mathrm{Na}} + I_{\mathrm{K}}$-model in Fig.10.6 is mainly positive in the Class 1 regime, that is, when the oscillations appear via saddle-node on invariant circle bifurcation, but changes sign in the Class 2 regime, corresponding in this case to the supercritical Andronov-Hopf bifurcation. In section 10.4 we find PRCs analytically in the case of weak coupling, and show that the PRC of a Class 1 oscillator has the shape $\sin^2 \vartheta$ (period $T = \pi$) or $1 - \cos \vartheta$ (period $T = 2\pi$), whereas that of a Class 2 oscillator has the shape $\sin \vartheta$ (period $T = 2\pi$). We show in section 10.1.7 how the synchronization properties of an oscillator depend on the shape of its PRC.

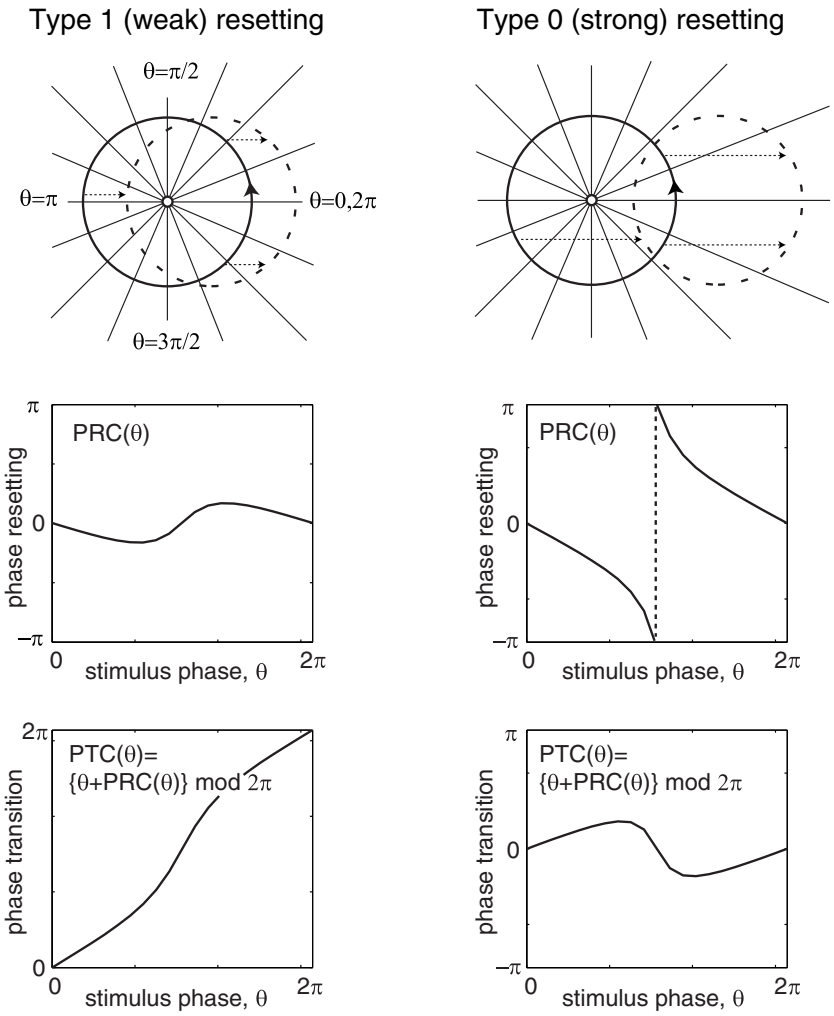

Figure 10.7: Types of phase-resetting of the Andronov-Hopf oscillator in Fig.10.3.

10.1.4 Type 0 and Type 1 Phase Response

Instead of phase-resetting curves, many researchers in the field of circadian rhythms consider *phase transition curves* (Winfree 1980)

$$\vartheta_{\text{new}} = \text{PTC}\,(\vartheta_{\text{old}}).$$

Since

$$\text{PTC}\,(\vartheta) = \{\vartheta + \text{PRC}\,(\vartheta)\} \bmod T,$$

the two approaches are equivalent. PRCs are convenient when the phase shifts are small, so that they can be magnified and seen clearly. PTCs are convenient when the phase shifts are large and comparable with the period of oscillation. We present PTCs in this section solely for the sake of review, and we use PRCs throughout the rest of the chapter.

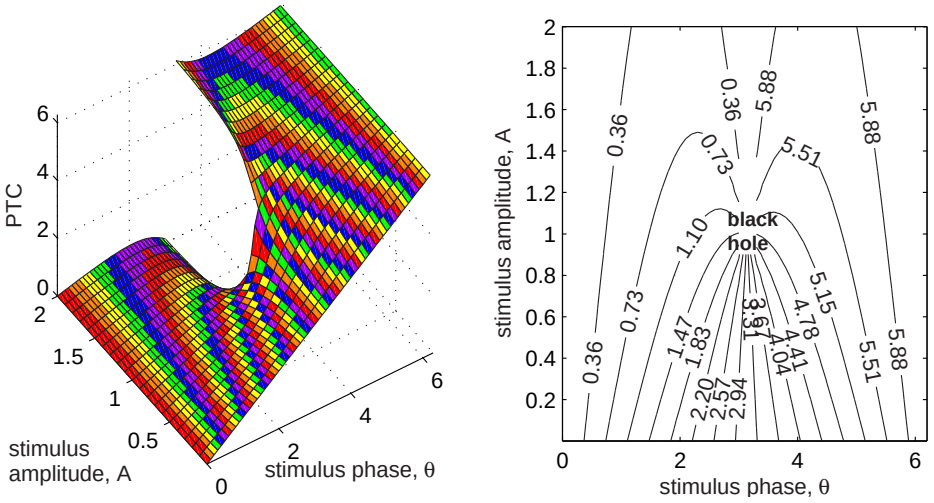

Figure 10.8: Time crystal (left) and its contour plot (right). Shown is the PTC (ϑ, A) of the Andronov-Hopf oscillator (see exercise 4).

In Fig.10.7 (top) we depict phase portraits of the Andronov-Hopf oscillator having radial isochrons and receiving pulses of magnitude $A = 0.5$ (left) and $A = 1.5$ (right). Note the drastic difference between the corresponding PRCs or PTCs. Winfree (1980) distinguishes two cases:

- *Type 1 (weak) resetting* results in continuous PRCs and PTCs with mean slope 1.

- *Type 0 (strong) resetting* results in discontinuous PRCs and PTCs with mean slope 0.

(Do not confuse these classes with Class 1, 2, or 3 excitability.) The discontinuity of the Type 0 PRC in Fig.10.7 is a topological property that cannot be removed by reallocating the initial point x_0 that corresponds to zero phase. As an exercise, prove that the discontinuity stems from the fact that the shifted image of the limit cycle (dashed circle) goes beyond the central equilibrium at which the phase is not defined.

If we vary not only the phase ϑ of the applied stimulus, but also its amplitude A, then we obtain parameterized PRC and PTC. In Fig.10.8 we plot PTC (ϑ, A) of the Andronov-Hopf oscillator (the corresponding PRC is derived in exercise 4). The surface is called *time crystal* and it can take quite amazing shapes (Winfree 1980). The contour plot of PTC (ϑ, A) in the figure contains the singularity point (black hole) that corresponds to the phaseless equilibrium of the Andronov-Hopf oscillator. Stimulation at phase $\vartheta = \pi$ with magnitude $A = 1$ pushes the trajectory into the equilibrium and stalls the oscillation.

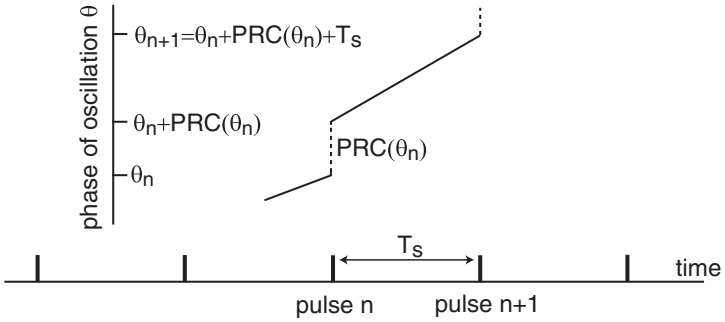

Figure 10.9: Calculation of the Poincare phase map.

10.1.5 Poincare Phase Map

The phase-resetting curve (PRC) describes the response of an oscillator to a single pulse, but it can also be used to study its response to a periodic pulse train using the following "stroboscopic" approach. Let ϑ_n denote the phase of oscillation at the time the nth input pulse arrives. Such a pulse resets the phase by $\mathrm{PRC}\,(\vartheta_n)$, so that the new phase right after the pulse is ϑ_n+$\mathrm{PRC}\,(\vartheta_n)$ (see Fig.10.9). Let T_s denote the period of pulsed stimulation. Then the phase of oscillation before the next, $(n+1)$th, pulse is ϑ_n+$\mathrm{PRC}\,(\vartheta_n) + T_\mathrm{s}$. Thus, we have a stroboscopic mapping of a circle to itself,

$$\vartheta_{n+1} = (\vartheta_n + \mathrm{PRC}\,(\vartheta_n) + T_\mathrm{s}) \mod T, \tag{10.3}$$

called the *Poincare phase map* (two pulse-coupled oscillators are considered in exercise 11). Knowing the initial phase of oscillation ϑ_1 at the first pulse, we can determine ϑ_2, then ϑ_3, and so on. The sequence $\{\vartheta_n\}$ with $n = 1, 2, \ldots$, is called the *orbit* of the map, and it is quite easy to find numerically.

Let us illustrate this concept using the $I_\mathrm{Na} + I_\mathrm{K}$-oscillator with PRC shown in Fig.10.4. Its free-running period is $T \approx 21.37$ ms, and the period of stimulation in Fig.10.10a is $T_\mathrm{s} = 18.37$, which results in the Poincare phase map depicted in Fig.10.10d. The cobweb in the figure is the orbit going from ϑ_1 to ϑ_2 to ϑ_3, and so on. Note that the phase ϑ_3 cannot be measured directly from the voltage trace in Fig.10.10a because pulse 2 changes the phase, so it is not the time since the last spike when pulse 3 arrives. The Poincare phase map (10.3) takes into account such multiple pulses. The orbit approaches a point (called a fixed point; see below) that corresponds to a synchronized or phase-locked state.

A word of caution is in order. Recall that PRCs are measured on the limit cycle attractor. However, each pulse displaces the trajectory away from the attractor, as in Fig.10.5. To use the PRC formalism to describe the effect of the next pulse, the oscillator must be given enough time to relax back to the limit cycle attractor. Thus, if the period of stimulation T_s is too small, or the attraction to the limit cycle is too slow, or the stimulus amplitude is too large, the Poincare phase map may be not an appropriate tool to describe the phase dynamics.

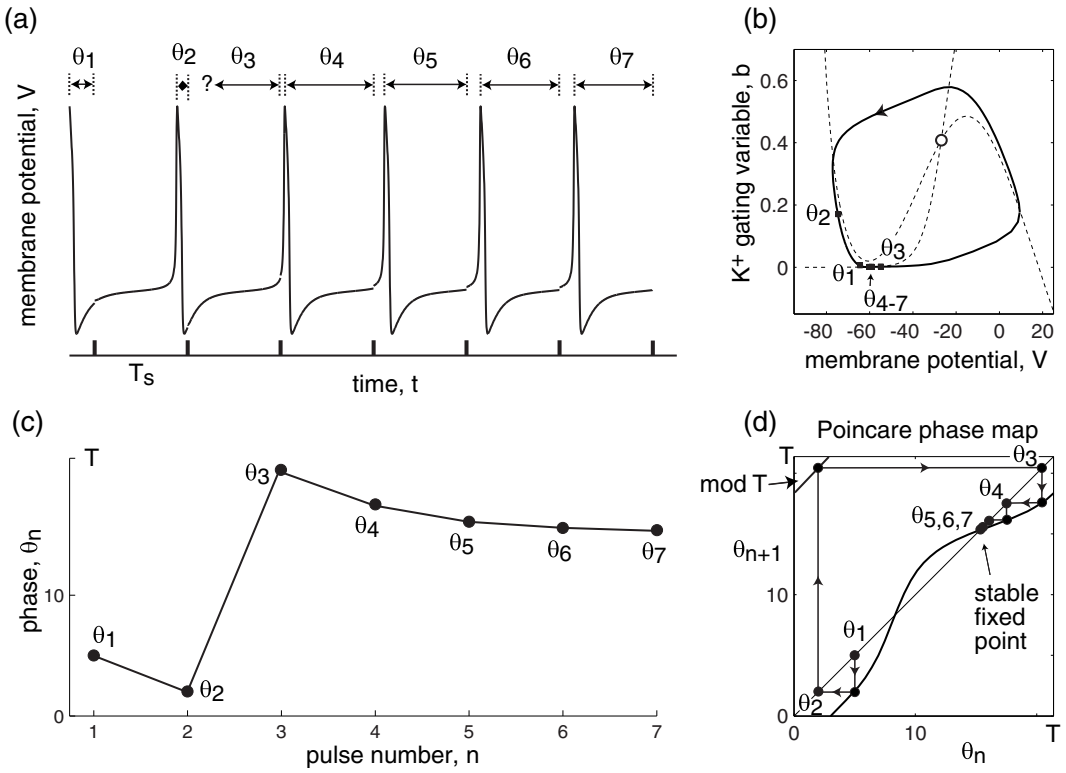

Figure 10.10: Description of synchronization of $I_{\rm Na} + I_{\rm K}$-oscillator in Fig.10.4, using Poincare phase map.

10.1.6 Fixed points

To understand the structure of orbits of the Poincare phase map (10.3), or any other map

$$\vartheta_{n+1} = f(\vartheta_n) \ , \tag{10.4}$$

we need to find its fixed points

$$\vartheta = f(\vartheta) \qquad (\vartheta \text{ is a fixed point}),$$

which are analogues of equilibria of continuous dynamical systems. Geometrically, a fixed point is the intersection of the graph of $f(\vartheta)$ with the diagonal line $\vartheta_{n+1} = \vartheta_n$ (see Fig.10.10d or Fig.10.11). At such a point, the orbit $\vartheta_{n+1} = f(\vartheta_n) = \vartheta_n$ is fixed. A fixed point ϑ is *asymptotically stable* if it attracts all nearby orbits, i.e., if ϑ_1 is in a sufficiently small neighborhood of ϑ, then $\vartheta_n \to \vartheta$ as $n \to \infty$, as in Fig.10.11, left. The fixed point is *unstable* if any small neighborhood of the point contains an orbit diverging from it, as in Fig.10.11 (right).

The stability of the fixed point is determined by the slope

$$m = f'(\vartheta)$$

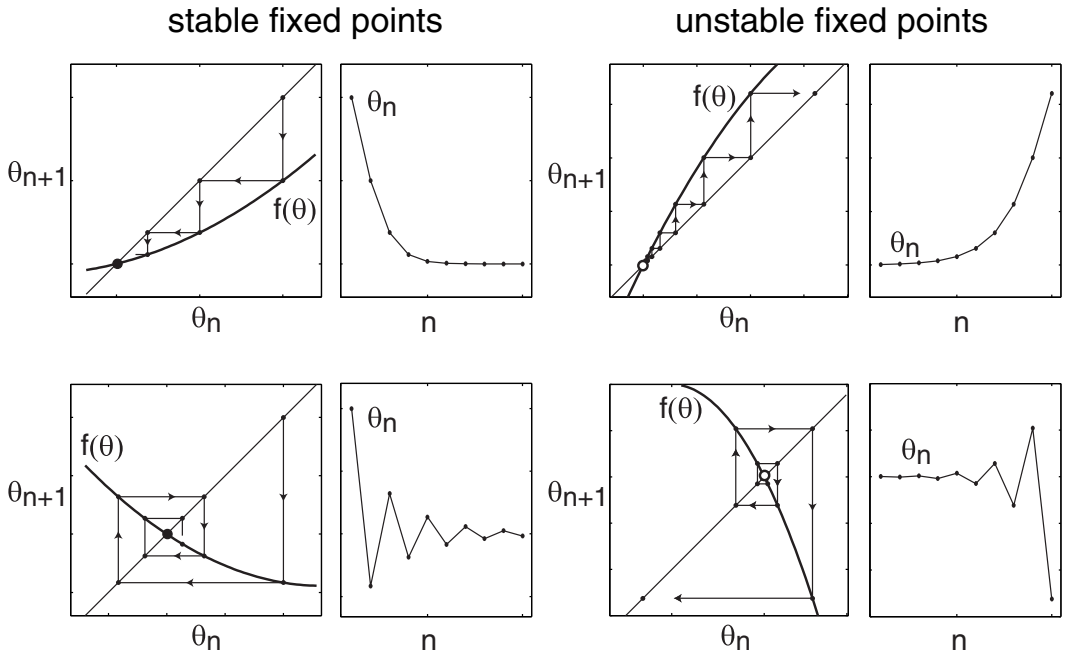

Figure 10.11: The stability of fixed points of the mapping (10.4) depends on the slope of the function f.

of the graph of f at the point, which is called the *Floquet multiplier* of the mapping. It plays the same role as the eigenvalue λ of an equilibrium of a continuous dynamical system. Mnemonically, the relationship between them is $\mu = e^{\lambda}$, to which the fixed point is stable when $|m| < 1$ ($\lambda < 0$) and unstable when $|m| > 1$ ($\lambda > 0$). Fixed points bifurcate when $|m| = 1$ (λ is zero or purely imaginary). They lose stability via flip bifurcation (a discrete analogue of Andronov-Hopf bifurcation) when $m = -1$ and disappear via fold bifurcation (a discrete analogue of saddle-node bifurcation) when $m = 1$. The former plays an important role in the period-doubling phenomenon illustrated in Fig.10.14 (bottom trace). The latter plays an important role in the cycle-slipping phenomenon illustrated in Fig.10.16.

10.1.7 Synchronization

We say that two periodic pulse trains are synchronous when the pulses occur at the same time or with a constant phase shift, as in Fig.10.12a. Each subplot in the figure contains an input pulse train (bottom) and an output spike train (top), assuming that spikes are fired at zero crossings of the phase variable, as in Fig.10.1. Such a synchronized state corresponds to a stable fixed point of the Poincare phase map (10.3). The in-phase, anti-phase, or out-of-phase synchronization corresponds to the phase shift $\vartheta = 0$, $\vartheta = T/2$, or some other value, respectively. Many scientists refer to the in-phase synchronization simply as "synchronization", and use the adjectives anti-phase and out-of-phase to denote the other types of synchronization.

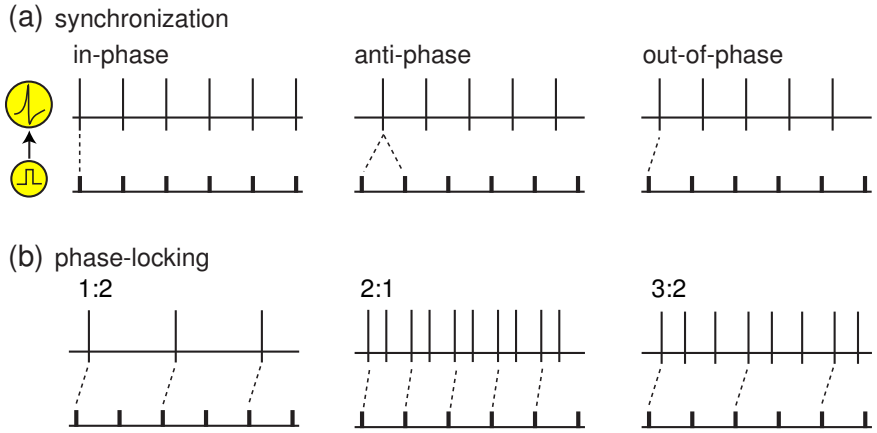

Figure 10.12: Examples of fundamental types of synchronization of spiking activity to periodic pulsed inputs (synchronization is 1:1 phase-locking).

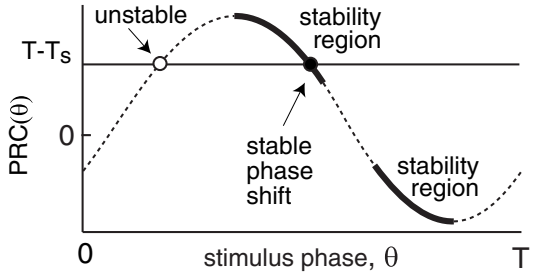

Figure 10.13: Fixed points of the Poincare phase map (10.3).

When the period of stimulation, $T_{\rm s}$, is near the free-running period of tonic spiking, T, the fixed point of (10.3) satisfies

$$\mathrm{PRC}\,(\vartheta) = T - T_{\rm s}\ ,$$

that is, it is the intersection of the PRC and the horizontal line, as in Fig.10.13. Thus, synchronization occurs with a phase shift ϑ that compensates for the input period mismatch $T - T_{\rm s}$. The maxima and the minima of the PRC determine the oscillator's tolerance of the mismatch. As an exercise, check that stable fixed points lie on the side of the graph with the slope

$$-2 < \mathrm{PRC}'(\vartheta) < 0 \qquad \text{(stability region)}$$

marked by the bold curves in Fig.10.13.

Now consider the Class 1 and Class 2 $I_{\rm Na} + I_{\rm K}$-oscillators shown in Fig.10.6. The PRC in the Class 1 regime is mostly positive, implying that such an oscillator can easily synchronize with faster inputs ($T - T_{\rm s} > 0$) but cannot synchronize with slower inputs. Indeed, the oscillator can advance its phase to catch up with faster pulse trains, but it cannot delay the phase to wait for the slower input. Synchronization with the input having $T_{\rm s} \approx T$ is only marginal. In contrast, the Class 2 $I_{\rm Na} + I_{\rm K}$-oscillator does not have this problem because its PRC has well-defined positive and negative regions.

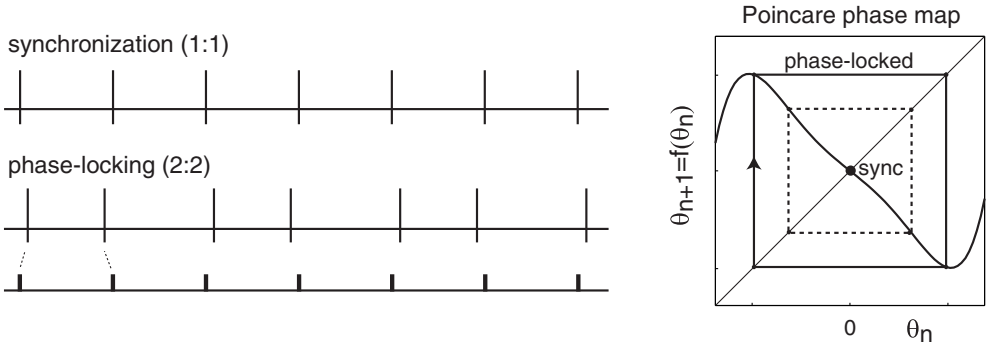

Figure 10.14: Coexistence of synchronized and phase-locked solutions corresponds to coexistence of a stable fixed point and a stable periodic orbit of the Poincare phase map.

10.1.8 Phase-Locking

The phenomenon of *p*:*q*-*phase-locking* occurs when the oscillator fires p spikes for every q input pulses, such as the 3:2-phase-locking in Fig.10.12b or the 2:2 phase-locking in Fig.10.14, which typically occurs when $pT \approx qT_{\rm s}$. The integers p and q need not be relatively prime in the case of pulsed-coupled oscillators. Synchronization, that is, 1:1 phase-locking, as well as p:1 phase-locking corresponds to a fixed point of the Poincare phase map (10.3) with p fired spikes per single input pulse. Indeed, the map tells the phase of the oscillator at each pulse, but not the number of oscillations between the pulses.

Each p:q-locked solution corresponds to a stable periodic orbit of the Poincare phase map with the period q (so that $\vartheta_n = \vartheta_{n+q}$ for any n). Such orbits in maps (10.4) correspond to stable equilibria in the iterates $\vartheta_{k+1} = f^q(\vartheta_k)$, where $f^q = f \circ f \circ \cdots \circ f$ is the composition of f with itself q times. Geometrically, studying such maps is like considering every qth input pulse in Fig.10.12b and ignoring all the intermediate pulses.

Since maps can have coexistence of stable fixed points and periodic orbits, various synchronized and phase-locking states can coexist in response to the same input pulse train, as in Fig.10.14. The oscillator converges to one of the states, depending on the initial phase of oscillation, but can be switched between states by a transient input.

10.1.9 Arnold Tongues

To synchronize an oscillator, the input pulse train must have a period $T_{\rm s}$ sufficiently near the oscillator's free-running period T so that the graph of the PRC and the horizontal line in Fig.10.13 intersect. The amplitude of the function $|\mathrm{PRC}\,(\vartheta, A)|$ decreases as the strength of the pulse A decreases, because weaker pulses produce weaker phase shifts. Hence the region of existence of a synchronized state shrinks as $A \to 0$, and it looks like a horn or a tongue on the $(T_{\rm s}, A)$-plane depicted in Fig.10.15, called *Arnold tongue*. Each p:q-phase-locked state has its own region of existence (p:q-tongue in the

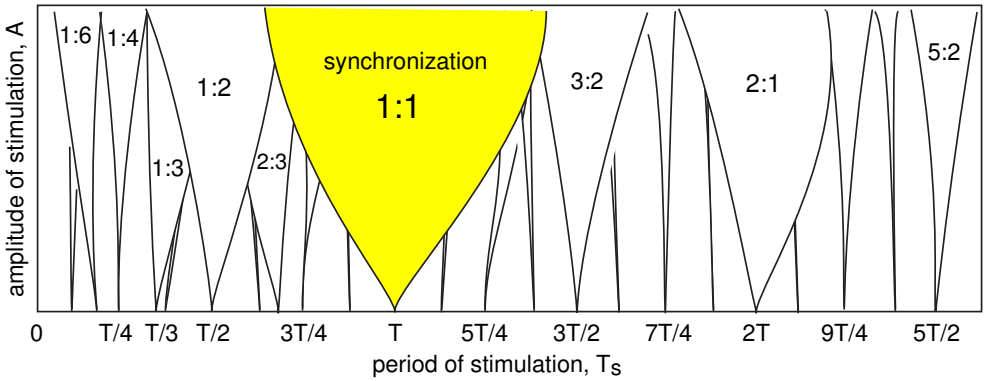

Figure 10.15: Arnold tongues are regions of existence of various phase-locked states on the "period-strength" plane.

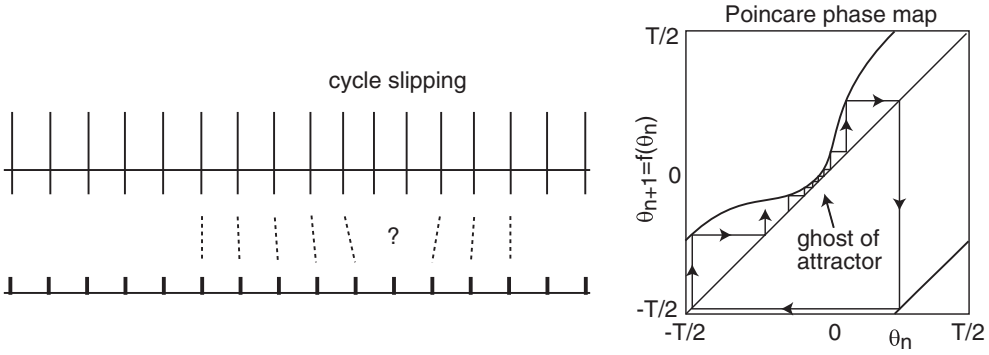

Figure 10.16: Cycle slipping phenomenon at the edge of the Arnold tongue corresponding to a synchronized state.

figure), which also shrinks to a point pT/q on the T_s-axis. The larger the order of locking, $p+q$, the narrower the tongue and the more difficult it is to observe such a phase-locked state numerically, let alone experimentally.

The tongues can overlap, leading to the coexistence of phase-locked states, as in Fig.10.14. If A is sufficiently large, the Poincare phase map (10.3) becomes noninvertible, that is, it has a region of negative slope, and there is a possibility of chaotic dynamics (Glass and Mackey 1988).

In Fig.10.16 we illustrate the *cycle slipping* phenomenon that occurs when the input period T_s drifts away from the 1:1 Arnold tongue. The fixed point of the Poincare phase map corresponding to the synchronized state undergoes a fold bifurcation and disappears. In a way similar to the case of saddle-node on invariant circle bifurcation, the fold fixed point becomes a ghost attractor that traps orbits and keeps them near the synchronized state for a long period of time. Eventually the orbit escapes, the synchronized state is briefly lost, and then the orbit returns to the ghost attractor to be trapped again. Such an intermittently synchronized orbit typically corresponds to a p:q-phase-locked state with a high order of locking $p+q$.

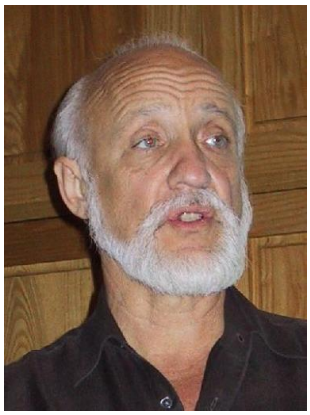

Figure 10.17: Arthur Winfree in 2001. (Photo provided by Martin Homer, University of Bristol.)

10.2 Weak Coupling

In this section we consider dynamical systems of the form

$$\dot{x} = f(x) + \varepsilon p(t) \ , \tag{10.5}$$

describing periodic oscillators, $\dot{x} = f(x)$, forced by a time-depended input $\varepsilon p(t)$, for instance, from other oscillators in a network. The positive parameter ε measures the overall strength of the input, and it is assumed to be sufficiently small, denoted as $\varepsilon \ll 1$. We do not assume $\varepsilon \to 0$ here. In fact, most of the results in this section can be cast in the form "there is an ε_0 such that for all $\varepsilon < \varepsilon_0$, the following holds. . ." (Hoppensteadt and Izhikevich 1997), with ε_0 depending on the function $f(x)$ in (10.5) and sometimes taking not so small values, such as, $\varepsilon_0 = 1$.

Note that if $\varepsilon = 0$ in (10.5), we can transform $\dot{x} = f(x)$, to $\dot{\vartheta} = 1$ using the theory presented in section 10.1. What happens when we apply the same transformation to (10.5) with $\varepsilon \neq 0$? In this section we present three different but equivalent approaches that transform (10.5) into the phase model

$$\dot{\vartheta} = 1 + \varepsilon \, \mathrm{PRC}\,(\vartheta) p(t) + o(\varepsilon) \ .$$

Here, Landau's "little oh" function $o(\varepsilon)$ denotes the error terms smaller than ε so that $o(\varepsilon)/\varepsilon \to 0$ if $\varepsilon \to 0$. For the sake of clarity of notation, we omit $o(\varepsilon)$ throughout the book, and implicitly assume that all equalities are valid up to the terms of order $o(\varepsilon)$.

Since we do not impose restrictions on the form of $p(t)$, the three methods are readily applicable to the case

$$p(t) = \sum_s g_s(x(t), x_s(t)) \ ,$$

where the set $\{x_s(t)\}$ denotes oscillators in the network connected to x, and $p(t)$ is the postsynaptic current.

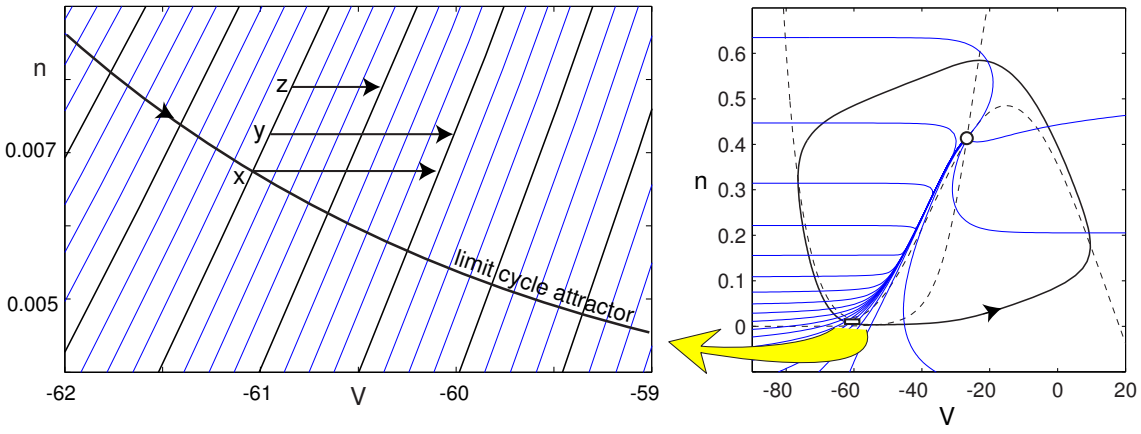

Figure 10.18: Magnification of isochrons in a small neighborhood of the limit cycle of the $I_{\rm Na} + I_{\rm K}$-model in Fig.10.3. Isochron time step: 0.025 ms on the left, 0.35 ms on the right.

10.2.1 Winfree's Approach

A sufficiently small neighborhood of the limit cycle attractor of the unperturbed ($\varepsilon = 0$) oscillator (10.5), magnified in Fig.10.18, has nearly collinear uniformly spaced isochrons. Collinearity implies that a point x on the limit cycle in Fig.10.18 has the same phase-resetting as any other point y on the isochron of x near the cycle. Uniform density of isochrons implies that the phase-resetting scales linearly with the strength of the pulse, that is, a half-pulse at point z in Fig.10.18 produces a half-resetting of the phase.

Linear scaling of PRC with respect to the strength of the pulse motivates the substitution

$$\mathrm{PRC}\,(\vartheta, A) \approx Z(\vartheta)A\ ,$$

where $Z(\vartheta) = \partial\,\mathrm{PRC}(\vartheta, A)/\partial A$ at $A = 0$ is the *linear response* or *sensitivity* function (Winfree 1967) describing the slight alteration of rate, or of instantaneous frequency of oscillation, accompanying application of a small stimulus. Some call it the *infinitesimal PRC*.

Now suppose $\varepsilon \neq 0$ but is sufficiently small that the trajectory of the weakly perturbed oscillator (10.5) remains near the limit cycle attractor all the time. Let us replace the continuous input function $\varepsilon p(t)$ with the equivalent train of pulses of strength $A = \varepsilon p(t_n)h$, where h is a small interpulse interval (denoted as $T_{\rm s}$ in section 10.1), and $t_n = nh$ is the timing of the nth pulse, see Fig.10.19. We rewrite the corresponding Poincare phase map (10.3)

$$\vartheta(t_{n+1}) = \{\vartheta(t_n) + \overbrace{Z(\vartheta(t_n))\underbrace{\varepsilon p(t_n)h}_{A}}^{\mathrm{PRC}} + h\} \mod T$$

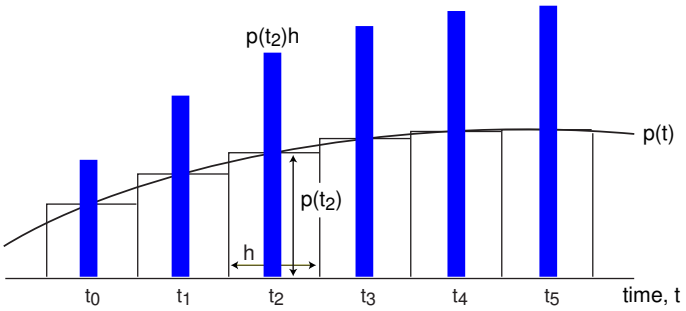

Figure 10.19: A continuous function $p(t)$ is replaced by an equivalent train of pulses of variable amplitudes.

Figure 10.20: Yoshiki Kuramoto in 1988, while he was visiting Jim Murray's institute at Oxford University. (Picture provided by Dr. Y. Kuramoto.)

in the form

$$\frac{\vartheta(t_n + h) - \vartheta(t_n)}{h} = Z(\vartheta(t_n))\varepsilon p(t_n) + 1 \ ,$$

which is a discrete version of

$$\dot{\vartheta} = 1 + \varepsilon Z(\vartheta) \cdot p(t), \tag{10.6}$$

in the limit $h \to 0$.

To be consistent with all the examples in section 10.1, we implicitly assume here that $p(t)$ perturbs only the first, voltage-like variable x_1 of the state vector $x = (x_1, \ldots, x_m) \in \mathbb{R}^m$ and that $Z(\vartheta)$ is the corresponding sensitivity function. However, the phase model (10.6) is also valid for an arbitrary input $p(t) = (p_1(t), \ldots, p_m(t))$. Indeed, let Z_i describe the linear response to perturbations of the ith state variable x_i, and $Z(\vartheta) = (Z_1(\vartheta), \ldots, Z_m(\vartheta))$ denote the corresponding linear response vector-function. Then the combined phase shift $Z_1 p_1 + \cdots + Z_m p_m$ is the dot product $Z \cdot p$ in (10.6).

10.2.2 Kuramoto's Approach

Consider the unperturbed ($\varepsilon = 0$) oscillator (10.5), and let the function $\vartheta(x)$ denote the phases of points near its limit cycle attractor. Obviously, isochrons are the level

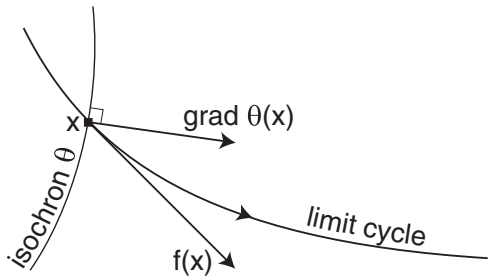

Figure 10.21: Geometrical interpretation of the vector grad ϑ.

contours of $\vartheta(x)$ since the function is constant on each isochron. Differentiating the function using the chain rule yields

$$\frac{d\vartheta(x)}{dt} = \operatorname{grad}\vartheta \cdot \frac{dx}{dt} = \operatorname{grad}\vartheta \cdot f(x) \ ,$$

where $\operatorname{grad}\vartheta = (\vartheta_{x_1}(x), \ldots, \vartheta_{x_m}(x))$ is the gradient of $\vartheta(x)$ with respect to the state vector $x = (x_1, \ldots, x_m) \in \mathbb{R}^m$. However,

$$\frac{d\vartheta(x)}{dt} = 1$$

near the limit cycle because isochrons are mapped to isochrons by the flow of the vector field $f(x)$. Therefore, we obtain a useful equality,

$$\operatorname{grad}\vartheta \cdot f(x) = 1 \ . \tag{10.7}$$

Figure 10.21 shows a geometrical interpretation of grad $\vartheta(x)$: it is the vector based at point x, normal to the isochron of x and with a length equal to the number density of isochrons at x. Its length can also be found from (10.7).

Kuramoto (1984) applied the chain rule to the perturbed system (10.5),

$$\frac{d\vartheta(x)}{dt} = \operatorname{grad}\vartheta \cdot \frac{dx}{dt} = \operatorname{grad}\vartheta \cdot \{f(x) + \varepsilon p(t)\} = \operatorname{grad}\vartheta \cdot f(x) + \varepsilon \operatorname{grad}\vartheta \cdot p(t) \ ,$$

and, using (10.7), obtained the phase model

$$\dot{\vartheta} = 1 + \varepsilon \operatorname{grad}\vartheta \cdot p(t) \ , \tag{10.8}$$

which has the same form as (10.6). Subtracting (10.8) from (10.6) yields $(Z(\vartheta) - \operatorname{grad}\vartheta) \cdot p(t) = 0$. Since this is valid for any $p(t)$, we conclude that $Z(\vartheta) = \operatorname{grad}\vartheta$ (see also exercise 6). Thus, Kuramoto's phase model (10.8) is indeed equivalent to Winfree's model (10.8).

10.2.3 Malkin's Approach

Yet another equivalent method of reduction of weakly perturbed oscillators to their phase models follows from Malkin's theorem (1949, 1956), which we state in the simplest form below. The most abstract form and its proof are provided by Hoppensteadt and Izhikevich (1997).

Figure 10.22: Ioel Gil'evich Malkin (Иоэль Гильевич Малкин, 1907–1958).

Malkin's theorem. Suppose the unperturbed ($\varepsilon = 0$) oscillator in (10.5) has an exponentially stable limit cycle of period T. Then its phase is described by the equation

$$\dot{\vartheta} = 1 + \varepsilon Q(\vartheta) \cdot p(t) \ , \tag{10.9}$$

where the T-periodic function Q is the solution to the linear "adjoint" equation

$$\dot{Q} = -\{Df(x(t))\}^\top Q \ , \qquad \text{with} \quad Q(0) \cdot f(x(0)) = 1 \ , \tag{10.10}$$

where $Df(x(t))^\top$ is the transposed Jacobian of f (matrix of partial derivatives) at the point $x(t)$ on the limit cycle, and the normalization condition can be replaced by $Q(t) \cdot f(x(t)) = 1$ for any, and hence all, t. Here $Q \cdot f$ is the dot product of two vectors, which is the same as $Q^\top f$.

Though this theorem looks less intuitive than the methods of Winfree and Kuramoto, it is actually more useful because (10.10) can be solved numerically quite easily. Applying the MATLAB procedure in exercise 12 to the four oscillators in Fig.10.3, we plot their functions Q in Fig.10.23. It is not a coincidence that each component of Q looks like PRC along the first or second state variable, shown in Fig.10.6. Subtracting (10.9) from (10.8) or from (10.6), we conclude that

$$Z(\vartheta) = \operatorname{grad} \vartheta(x) = Q(\vartheta) \ ,$$

(see also exercise 7), so that we can determine the linear response function of the phase model using any of the three alternative methods: via PRCs, via isochrons, or solving the adjoint equation (10.10). This justifies the reason why many refer to the function simply as PRC, implicitly assuming that it is measured to the infinitesimal stimuli and then normalized by the stimulus amplitude.

10.2.4 Measuring PRCs Experimentally

In Fig.10.24 we exploit the relationship (10.9) and measure the infinitesimal PRCs of a layer 5 pyramidal neuron of mouse visual cortex. First, we stimulate the neuron with 40 pA DC current to elicit periodic spiking. Initially, the firing period starts at 50 ms, and then relaxes to the averaged value of 110 ms (Fig.10.24a). The standard method of finding PRCs consists in stimulating the neuron with brief pulses of current at different

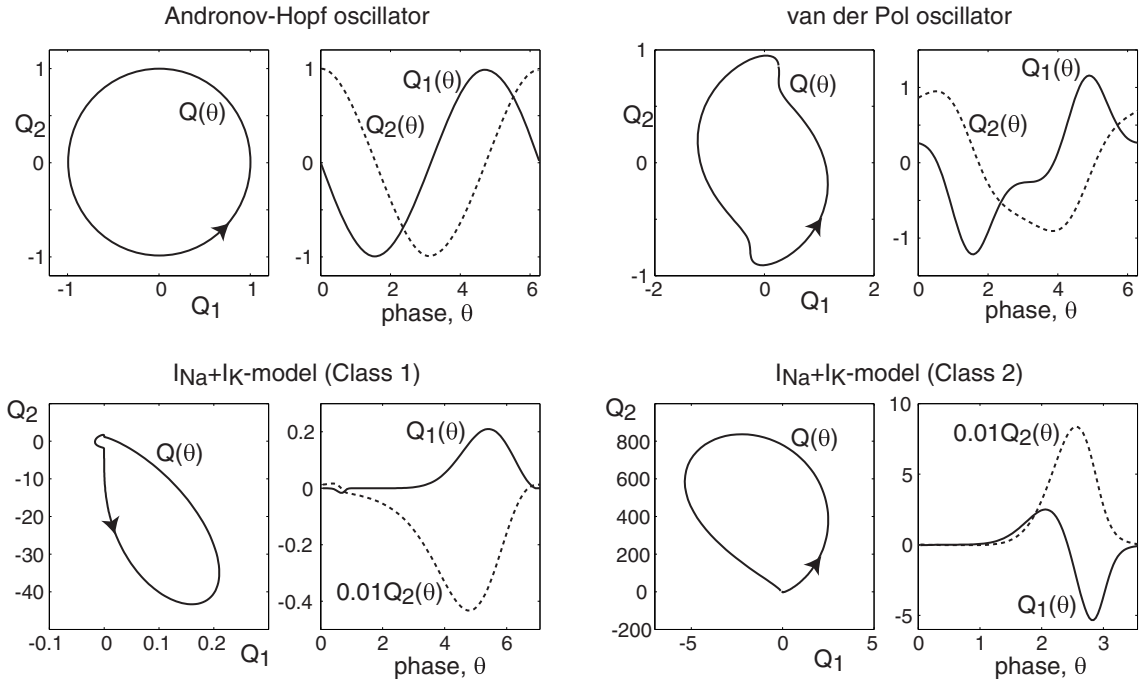

Figure 10.23: Solutions $Q = (Q_1, Q_2)$ to adjoint problem (10.10) for oscillators in Fig.10.3.

phases of the cycle and measuring the induced phase shift, which can be approximated by the difference between two successive periods of oscillation. The method works well in models (see exercise 5), but should be used with caution in real neurons because their firing is too noisy, as we demonstrate in Fig.10.24b. Thus, one needs to apply hundreds, if not thousands, of pulses and then average the resulting phase deviations (Reyes and Fetz 1993).

Starting with time 10 sec, we inject a relatively weak noisy current $\varepsilon p(t)$ that continuously perturbs the membrane potential (Fig.10.24c) and, hence, the phase of oscillation (the choice of $p(t)$ is important; its Fourier spectrum must span a range of frequencies that depends on the frequency of firing of the neuron). Knowing $\varepsilon p(t)$, the moments of firing of the neuron, which are zero crossings $\vartheta(t) = 0$, and the relationship

$$\dot{\vartheta} = 1 + \mathrm{PRC}\,(\vartheta)\varepsilon p(t)\ ,$$

we solve the inverse problem for the infinitesimal $\mathrm{PRC}\,(\vartheta)$ and plot the solution in Fig.10.24d. As one expects, the PRC is mostly positive, maximal just before the spike and almost zero during the spike. It would resemble the PRC in Fig.10.23 ($Q_1(\vartheta)$ in Class 1) if not for the dip in the middle, for which we have no explanation (probably it is due to overfitting). The advantage of this method is that it is more immune to noise, because intrinsic fluctuations are spread over the entire $p(t)$ and not concentrated at the moments of pulses – unless, of course $p(t)$, consists of random pulses, in which case this method is equivalent to the standard one. The drawback is that we need to solve

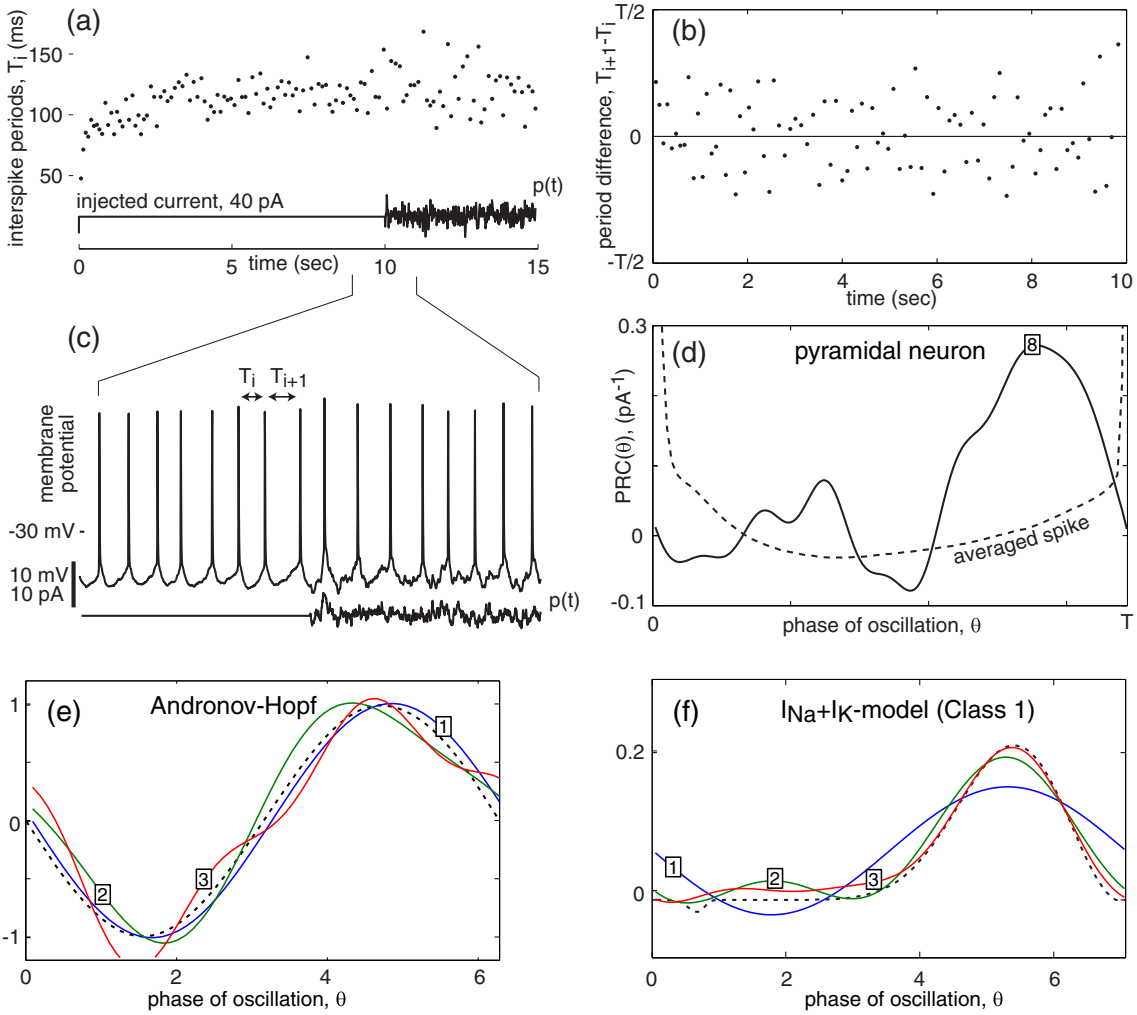

Figure 10.24: Measuring the infinitesimal PRC experimentally in a layer 5 pyramidal neuron of mouse visual cortex. (a) Interspike periods in response to the injection of DC current. (b) Differences between successive periods. (c) Spiking 1 second before and after the noisy current $p(t)$ is injected. (d) Infinitesimal PRC of the neuron (continuous curve) obtained from 40 cycles and the MATLAB program in exercise 13 (first eight Fourier terms). Averaged voltage trace during the spike (dotted curve) is plotted for reference. The same procedure is applied to (e) the Andronov-Hopf oscillator and (f) the $I_{\mathrm{Na,p}}$+I_{K}-model. Numbers in boxes represent the number of Fourier terms used to fit the curve; theoretical curves (functions $Q_1(\vartheta)$ from Fig.10.23) are dashed.

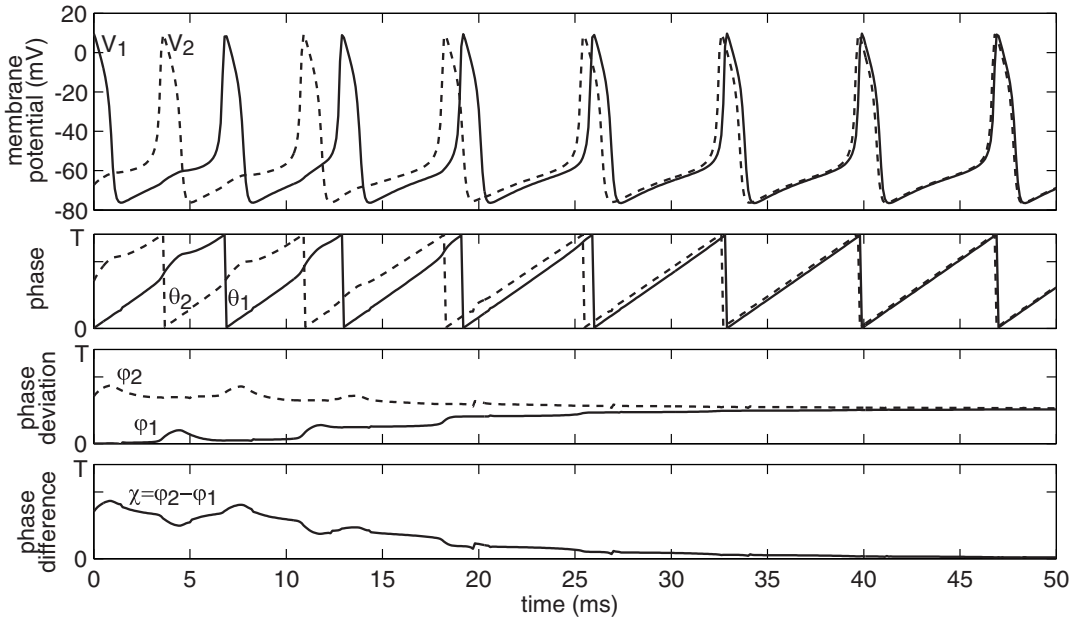

Figure 10.25: The relationship between membrane potential oscillation of two neurons, V_1 (solid) and V_2 (dashed), their phases, phase deviations, and phase difference. Shown are simulation of two $I_{\mathrm{Na}} + I_{\mathrm{K}}$-models with parameters as in Fig.10.3 and coupled symmetrically via gap junctions $0.1(V_j - V_i)$ (see section 2.3.4).

the equation above, which we do in exercise 13, using an optimization technique.

10.2.5 Phase Model for Coupled Oscillators

Now consider n weakly coupled oscillators of the form

$$\dot{x}_i = f_i(x_i) + \varepsilon \overbrace{\sum_{j=1}^{n} g_{ij}(x_i, x_j)}^{p_i(t)} , \quad x_i \in \mathbb{R}^m , \tag{10.11}$$

and assume that the oscillators, when uncoupled ($\varepsilon = 0$), have equal free-running periods $T_1 = \cdots = T_n = T$. Applying any of the three methods above to such a weakly perturbed system, we obtain the corresponding phase model

$$\dot{\vartheta}_i = 1 + \varepsilon\, Q_i(\vartheta_i) \cdot \overbrace{\sum_{j=1}^{n} g_{ij}(x_i(\vartheta_i), x_j(\vartheta_j))}^{p_i(t)} , \tag{10.12}$$

where each $x_i(\vartheta_i)$ is the point on the limit cycle having phase ϑ_i. Note that (10.11) is defined in $\mathbb{R}^{nm}$, whereas the phase model (10.12) is defined on the n-torus, denoted as $\mathbb{T}^n$.

To study collective properties of the network, such as synchronization, it is convenient to represent each $\vartheta_i(t)$ as

$$\vartheta_i(t) = t + \varphi_i \ , \tag{10.13}$$

with the first term capturing the *fast* free-running natural oscillation $\dot{\vartheta}_i = 1$, and the second term capturing the *slow* network-induced build-up of *phase deviation* from the natural oscillation. The relationship between $x_i(t)$, $\vartheta_i(t)$ and $\varphi_i(t)$ is illustrated in Fig.10.25.

Substituting (10.13) into (10.12) results in

$$\dot{\varphi}_i = \varepsilon\, Q_i(t+\varphi_i) \cdot \sum_{j=1}^{n} g_{ij}(x_i(t+\varphi_i), x_j(t+\varphi_j)) \ . \tag{10.14}$$

Note that the right-hand side is of order ε, reflecting the slow dynamics of phase deviations φ_i seen in Fig.10.25. Thus, it contains two time scales: fast oscillations (variable t) and slow phase modulation (variables φ). The classical method of averaging, reviewed by Hoppensteadt and Izhikevich (1997, Chap. 9), consists in a near-identity change of variables that transforms the system into the form

$$\dot{\varphi}_i = \varepsilon\omega_i + \varepsilon \sum_{j\neq i}^{n} H_{ij}(\varphi_j - \varphi_i) \ , \tag{10.15}$$

where

$$H_{ij}(\varphi_j - \varphi_i) = \frac{1}{T}\int_0^T Q_i(t) \cdot g_{ij}(x_i(t), x_j(t+\varphi_j-\varphi_i))\, dt \ , \tag{10.16}$$

and each $\omega_i = H_{ii}(\varphi_i - \varphi_i) = H_{ii}(0)$ describes a constant frequency deviation from the free-running oscillation. Figure 10.26 depicts the functions H_{ij} corresponding to

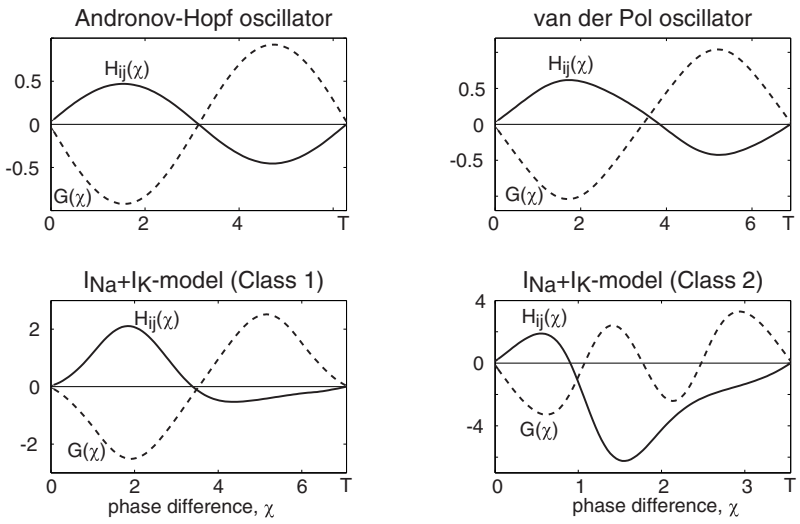

Figure 10.26: Solid curves. Functions $H_{ij}(\chi)$ defined by (10.16) with the input $g(x_i, x_j) = (x_{j1} - x_{i1}, 0)$ corresponding to electrical synapse via gap-junction. Dashed curves. Functions $G(\chi) = H_{ji}(-\chi) - H_{ij}(\chi)$. Parameters are as in Fig.10.3.

gap-junction (i.e., electrical; see section 2.3.4) coupling of oscillators in Fig.10.3. Prove that $H(\chi) = Q(\chi) \cdot A/T$ in the case of pulse-coupling (10.1), so that $H(\chi)$ is just re-scaled PRC.

A special case of (10.15) occurs when H is replaced by its first Fourier term, sin. The resulting system, written in the slow time $\tau = \varepsilon t$,

$$\varphi_i' = \omega_i + \sum_{j=1}^{n} c_{ij} \sin(\varphi_j - \varphi_i + \psi_{ij}),$$

is called the *Kuramoto phase model* (Kuramoto 1975). Here, the frequency deviations ω_i are interpreted as intrinsic frequencies of oscillators. The strengths of connections c_{ij} are often assumed to be equal to K/n for some constant K, so that the model can be studied in the limit $n \to \infty$. The phase deviations ψ_{ij} are often neglected for the sake of simplicity.

To summarize, we transformed the weakly coupled system (10.11) into the phase model (10.15) with H given by (10.16) and each Q being the solution to the adjoint problem (10.10). This constitutes the Malkin theorem for weakly coupled oscillators (Hoppensteadt and Izhikevich 1997, theorem 9.2).

10.3 Synchronization

Consider two coupled phase variables (10.12) in a general form

$$\begin{aligned} \dot{\vartheta}_1 &= h_1(\vartheta_1, \vartheta_2) \,, \\ \dot{\vartheta}_2 &= h_2(\vartheta_1, \vartheta_2) \,, \end{aligned}$$

with some positive functions h_1 and h_2. Since each phase variable is defined on the circle $\mathbb{S}^1$, the state space of this system is the 2-torus $\mathbb{T}^2 = \mathbb{S}^1 \times \mathbb{S}^1$ depicted in Fig.10.27, with ϑ_1 and ϑ_2 being the longitude and the latitude, respectively. The torus can be represented as a square with vertical and horizontal sides identified, so that a solution disappearing at the right side of the square appears at the left side.

The coupled oscillators above are said to be *frequency-locked* when there is a periodic trajectory on the 2-torus, which is called a *torus knot*. It is said to be of type (p, q) if ϑ_1 makes p rotations while ϑ_2 makes q rotations, and p and q are relatively prime integers, that is, they do not have a common divisor greater than 1. Torus knots of type (p, q) produce p:q frequency-locking, e.g., the 2:3 frequency-locking in Fig.10.27. A 1:1 frequency-locking is called *entrainment*. There can be many periodic orbits on the torus, with stable orbits between unstable ones. Since the orbits on the 2-torus cannot intersect, they are all knots of the same type, resulting in the same p:q frequency-locking.

Let us follow a trajectory on the torus and count the number of rotations of the phase variables. The limit of the ratio of rotations as $t \to \infty$ is independent of the trajectory we follow, and it is called the *rotation number* of the torus flow. It is rational

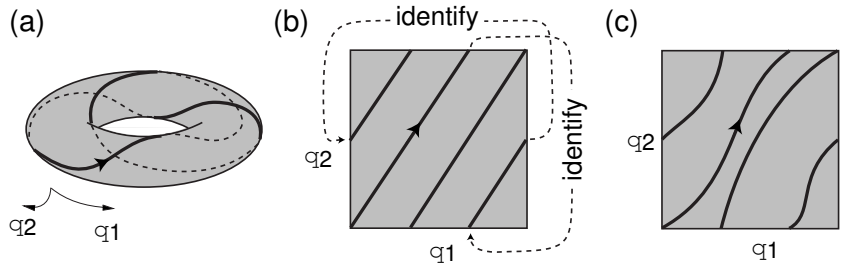

Figure 10.27: Torus knot of type (2, 3) (a) and its representation on the square (b). The knot produces frequency-locking and phase-locking. (c) Torus knot that does not produce phase-locking.

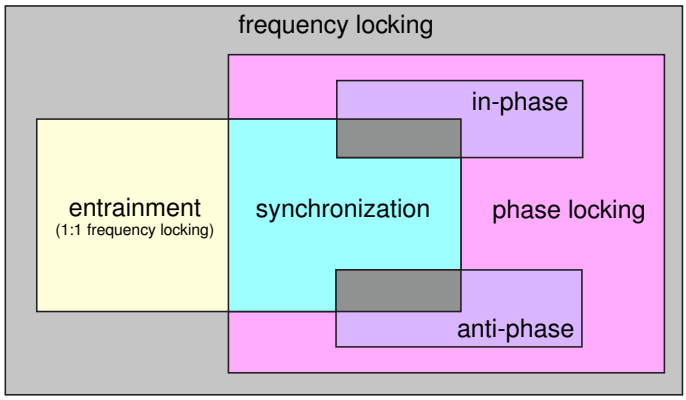

Figure 10.28: Various degrees of locking of oscillators.

if and only if there is a (p, q) periodic orbit, in which case the rotation number is p/q. An irrational rotation number implies there are no periodic orbits, and it corresponds to a *quasi-periodic* or *multifrequency* torus flow. Oscillators exhibit *phase drifting* in this case. Denjoy (1932) proved that such coupled oscillators are topologically equivalent to the uncoupled system $\dot{\vartheta}_1 = r,\ \dot{\vartheta}_2 = 1$ with irrational r.

Suppose the oscillators are frequency-locked; that is, there is a p:q limit cycle attractor on the torus. We say that the oscillators are p:q *phase-locked* if

$$q\vartheta_1(t) - p\vartheta_2(t) = \text{const}$$

on the cycle. The value of the constant determines whether the locking is in-phase (const= 0), anti-phase (const= $T/2$; half-period), or out-of-phase. Frequency-locking does not necessarily imply phase-locking: the $(2, 3)$ torus knot in Fig.10.27b corresponds to phase-locking, whereas that in Fig.10.27c does not. Frequency-locking without phase-locking is called *phase trapping*. Finally, *synchronization* is a 1:1 phase-locking. The phase difference $\vartheta_2 - \vartheta_1$ is also called *phase lag* or *phase lead*. The relationships between all these definitions are shown in Fig.10.28.

Frequency-locking, phase-locking, entrainment, and synchronization of a network of $n > 2$ oscillators are the same as pairwise locking, entrainment, and synchronization

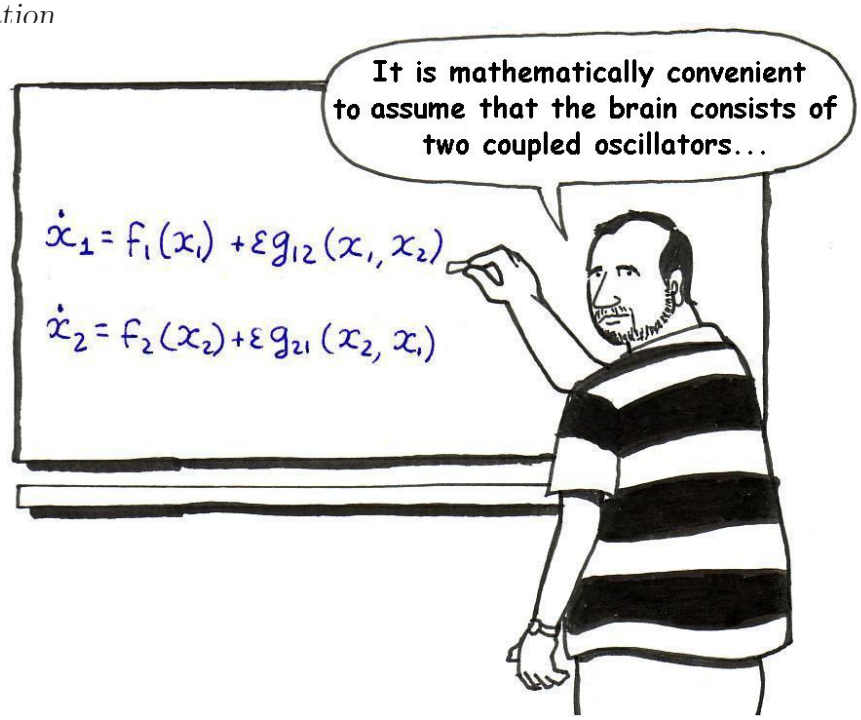

Figure 10.29: A major part of computational neuroscience concerns coupled oscillators.

of the oscillators comprising the network. In addition, a network can exhibit partial synchronization when only a subset of oscillators is synchronized.

Synchronization of oscillators with nearly identical frequencies is described by the phase model (10.15). Existence of one equilibrium of (10.15) implies the existence of the entire circular family of equilibria, since translation of all φ_i by a constant phase shift does not change the phase differences $\varphi_j - \varphi_i$, and hence the form of (10.15). This family corresponds to a limit cycle of (10.11), on which all oscillators, $x_i(t + \varphi_i)$, have equal frequencies and constant phase shifts (i.e., they are synchronized, possibly out-of-phase).

10.3.1 Two Oscillators

Consider (10.11) with $n = 2$, describing two coupled oscillators, as in Fig.10.29. Let us introduce the "slow" time $\tau = \varepsilon t$ and rewrite the corresponding phase model (10.15) in the form

$$\begin{aligned} \varphi_1' &= \omega_1 + H_1(\varphi_2 - \varphi_1) \,, \\ \varphi_2' &= \omega_2 + H_2(\varphi_1 - \varphi_2) \,, \end{aligned}$$

where $' = d/d\tau$ is the derivative with respect to slow time. Let $\chi = \varphi_2 - \varphi_1$ denote the phase difference between the oscillators. Then the two-dimensional system above becomes the one-dimensional

$$\chi' = \omega + G(\chi) \,, \tag{10.17}$$

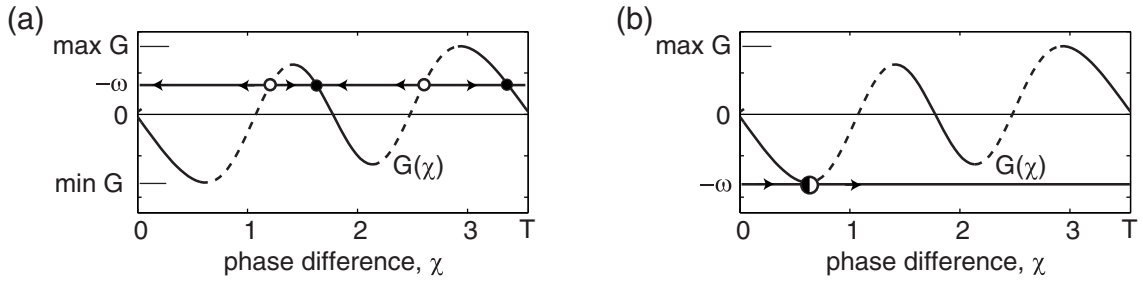

Figure 10.30: Geometrical interpretation of equilibria of the phase model (10.17) for gap-junction-coupled Class 2 $I_{\rm Na}+I_{\rm K}$-oscillators (see Fig.10.26).

where

$$\omega=\omega_2-\omega_1 \qquad \text{and} \qquad G(\chi)=H_2(-\chi)-H_1(\chi)$$

are the frequency mismatch and the anti-symmetric part of the coupling, respectively (illustrated in Fig.10.26, dashed curves). A stable equilibrium of (10.17) corresponds to a stable limit cycle of the phase model.

All equilibria of (10.17) are solutions to $G(\chi)=-\omega$, and they are intersections of the horizontal line $-\omega$ with the graph of G, as illustrated in Fig.10.30a. They are stable if the slope of the graph is negative at the intersection. If the oscillators are identical, then $G(\chi)=H(-\chi)-H(\chi)$ is an odd function (i.e., $G(-\chi)=-G(\chi)$), and $\chi=0$ and $\chi=T/2$ are always equilibria (possibly unstable) corresponding to the in-phase and anti-phase synchronized solutions. The stability condition of the in-phase synchronized state is

$$G'(0)=-2H'(0)<0 \qquad \text{(stability of in-phase synchronization)}$$

The in-phase synchronization of electrically (gap-junction) coupled oscillators in Fig.10.26 is stable because the slope of G (dashed curves) is negative at $\chi=0$. Simulation of two coupled $I_{\rm Na}+I_{\rm K}$-oscillators in Fig.10.25 confirms that. Coupled oscillators in the Class 2 regime also have a stable anti-phase solution, since $G'<0$ at $\chi=T/2$ in Fig.10.30a.

The max and min values of the function G determine the tolerance of the network for the frequency mismatch ω, since there are no equilibria outside this range. Geometrically, as ω increases (the second oscillator speeds up), the horizontal line $-\omega$ in Fig.10.30a slides downward, and the phase difference $\chi=\varphi_2-\varphi_1$ increases, compensating for the frequency mismatch ω. When $\omega>-\min G$, the second oscillator becomes too fast, and the synchronized state is lost via saddle-node on invariant circle bifurcation (see Fig.10.30b). This bifurcation corresponds to the annihilation of stable and unstable limit cycles of the weakly coupled network, and the resulting activity is called *drifting*, *cycle slipping*, or *phase walk-through*. The variable χ slowly passes the ghost of the saddle-node point, where $G(\chi)\approx 0$, then increases past T, appears at 0, and approaches the ghost again, thereby slipping a cycle and walking through all the phase values $[0,T]$. The frequency of such slipping scales as $\sqrt{\omega+\min G}$; see section 6.1.2.

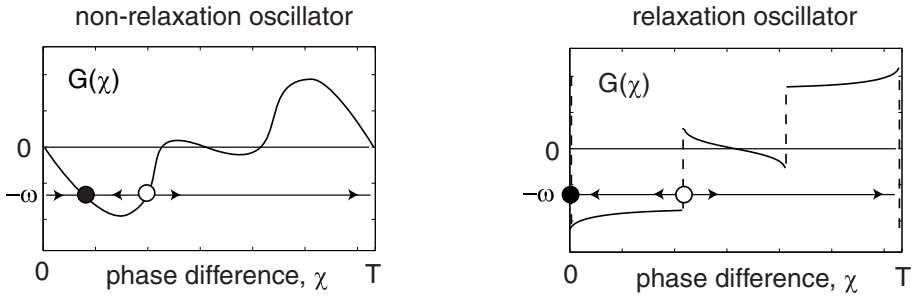

Figure 10.31: Functions $G(\chi)$ for weakly coupled oscillators of non-relaxation (smooth) and relaxation types. The frequency mismatch ω creates a phase difference in the smooth case, but not in the relaxation case.

In Fig.10.31 we contrast synchronization properties of weakly coupled oscillators of relaxation and non-relaxation type. The function $G(\chi)$ of the former has a negative discontinuity at $\chi = 0$ (section 10.4.4). An immediate consequence is that the in-phase synchronization is rapid and persistent in the presence of the frequency mismatch ω. Indeed, if G is smooth, then χ slows down while it approaches the equilibrium $\chi = 0$. As a result, complete synchronization is an asymptotic process that requires an infinite period of time to attain. In contrast, when G is discontinuous at 0, the variable χ does not slow down, and it takes a finite period of time to lock. Changing the frequency mismatch ω shifts the root of $-\omega = G(\chi)$ in the continuous case, but not in the discontinuous case. Hence, the in-phase synchronized state $\chi = 0$ of coupled relaxation oscillators exists and is stable in a wide range of ω.

10.3.2 Chains

Understanding the synchronization properties of two coupled oscillators helps one in studying the dynamics of chains of $n > 2$ oscillators

$$\varphi_i' = \omega_i + H^+(\varphi_{i+1} - \varphi_i) + H^-(\varphi_{i-1} - \varphi_i) \ , \tag{10.18}$$

where the functions H^+ and H^- describe the coupling in the ascending and descending directions of the chain, as in Fig.10.32. Any phase-locked solution of (10.18) has the form $\varphi_i(\tau) = \omega_0\tau + \phi_i$, where ω_0 is the common frequency of oscillation and ϕ_i are constants. These satisfy n conditions

$$\begin{aligned}
\omega_0 &= \omega_1 + H^+(\phi_2 - \phi_1) \ , \\
\omega_0 &= \omega_i + H^+(\phi_{i+1} - \phi_i) + H^-(\phi_{i-1} - \phi_i) \ , \qquad i = 2, \ldots, n-1 \ , \\
\omega_0 &= \omega_n + H^-(\phi_{n-1} - \phi_n) \ .
\end{aligned}$$

A solution with $\phi_1 < \phi_2 < \cdots < \phi_n$ or with $\phi_1 > \phi_2 > \cdots > \phi_n$ (as in Fig.10.32) is called a *traveling wave*. Indeed, the oscillators oscillate with a common frequency ω_0 but with different phases that increase or decrease monotonically along the chain.

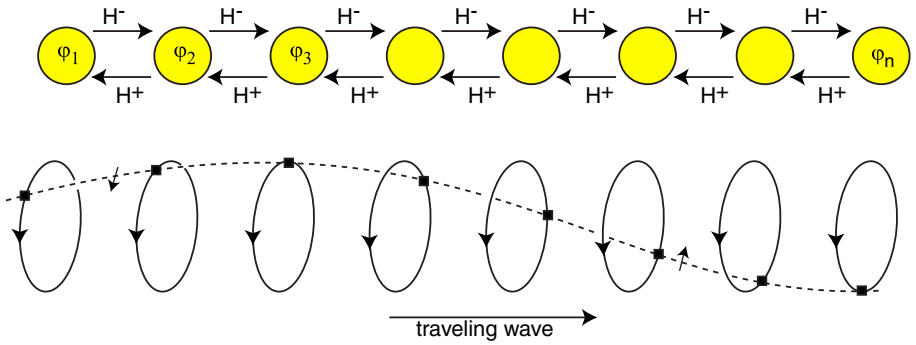

Figure 10.32: Traveling wave solutions in chains of oscillators (10.18) describe undulatory locomotion and central pattern generation.

Such a behavior is believed to correspond to central pattern generation (CPG) in crayfish, undulatory locomotion in lampreys and dogfish, and peristalsis in vascular and intestinal smooth muscles. Below we consider two fundamentally different mechanisms of generation of traveling waves.

Frequency Differences

Suppose the connections in (10.18) look qualitatively similar to those in Fig.10.26, in particular, $H^+(0) = H^-(0) = 0$. If the frequencies are all equal, then the in-phase synchronized solution $\varphi_1 = \cdots = \varphi_n$ exists and is stable. A traveling wave exists when the frequencies are not all equal.

Let us seek the conditions for the existence of a traveling wave with a constant phase shift, say $\chi = \phi_{i+1} - \phi_i$, along the chain. Subtracting each equation from the second one, we find that

$$0 = \omega_2 - \omega_1 + H^-(-\chi)\ , \qquad 0 = \omega_2 - \omega_i\ , \qquad 0 = \omega_2 - \omega_n + H^+(\chi)\ ,$$

and $\omega_0 = \omega_1 + \omega_n - 2\omega_2$. In particular, if $\omega_1 \le \omega_2 = \cdots = \omega_{n-1} \le \omega_n$, which corresponds to the first oscillator being tuned up and the last oscillator being tuned down, then $\chi < 0$ and the traveling wave moves upward, as in Fig.10.32, that is, from the fastest to the slowest oscillator. Interestingly, such an ascending wave exists even when $H^- = 0$, that is, even when the coupling is only in the opposite, descending direction.

When there is a linear gradient of frequencies ($\omega_1 > \omega_2 > \cdots > \omega_n$ or vice versa), as in the cases of the smooth muscle of intestines or leech CPG for swimming, one may still observe a traveling wave, but with a non-constant phase difference along the chain. When the gradient is large enough, the synchronized solution corresponding to a single traveling wave disappears, and frequency plateaus may appear (Ermentrout and Kopell 1984). That is, solutions occur in which the first $k < n$ oscillators are phase-locked and the last $n - k$ oscillators are phase-locked as well, but the two pools, forming two clusters, oscillate with different frequencies. There may be many frequency plateaus.

Coupling Functions

A traveling wave solution may exist even when all the frequencies are equal, if either $H^+(0) \neq 0$ or $H^-(0) \neq 0$. As an example, consider the case of descending coupling ($H^- = 0$)

$$\varphi_i' = \omega + H^+(\varphi_{i+1} - \varphi_i) \ , \qquad i = 1, \ldots, n-1 \ .$$

From $\varphi_n' = \omega$ we find that $\omega_0 = \omega$, that is, the common frequency is the frequency of the free oscillation of the last, uncoupled oscillator. The phase lag along the chain, $\chi = \varphi_{i+1} - \varphi_i$, satisfies $n-1$ identical conditions $0 = H^+(\chi)$. Thus, the traveling wave with a constant phase shift exists when H^+ has a zero crossing with positive slope, in contrast to Fig.10.26. The sign of χ, and not the direction of coupling, determines the direction of wave propagation.

10.3.3 Networks

Now let us consider weakly connected networks (10.11) with arbitrary, possibly all-to-all coupling. To study synchronized states of the network, we need to determine whether the corresponding phase model (10.15) has equilibria and to examine their stability properties. A vector $\phi = (\phi_1, \ldots, \phi_n)$ is an equilibrium of (10.15) when

$$0 = \omega_i + \sum_{j \neq 1}^{n} H_{ij}(\phi_j - \phi_i) \qquad \text{for all } i \ . \tag{10.19}$$

It is stable when all eigenvalues of the linearization matrix (Jacobian) at ϕ have negative real parts, except one zero eigenvalue corresponding to the eigenvector along the circular family of equilibria (ϕ plus a phase shift is a solution of (10.19), too, since the phase differences $\phi_j - \phi_i$ are not affected).

In general, determining the stability of equilibria is a difficult problem. Ermentrout (1992) found a simple sufficient condition. Namely, if

- $a_{ij} = H_{ij}'(\phi_j - \phi_i) \geq 0$, and
- the directed graph defined by the matrix $a = (a_{ij})$ is connected (i.e., each oscillator is influenced, possibly indirectly, by every other oscillator),

then the equilibrium ϕ is neutrally stable, and the corresponding limit cycle $x(t + \phi)$ of (10.11) is asymptotically stable.

Another sufficient condition was found by Hoppensteadt and Izhikevich (1997). It states that if system (10.15) satisfies

- $\omega_1 = \cdots = \omega_n = \omega$ (identical frequencies) and
- $H_{ij}(-\chi) = -H_{ji}(\chi)$ (pairwise odd coupling)

for all i and j, then the network dynamics converge to a limit cycle. On the cycle, all oscillators have equal frequencies $1 + \varepsilon\omega$ and constant phase deviations.

The proof follows from the observation that (10.15) is a gradient system in the rotating coordinates $\varphi = \omega\tau + \phi$, with the energy function

$$E(\phi) = \frac{1}{2}\sum_{i=1}^{n}\sum_{j=1}^{n} R_{ij}(\phi_j - \phi_i) \ , \qquad \text{where} \qquad R_{ij}(\chi) = \int_0^{\chi} H_{ij}(s)\, ds \ .$$

One can check that $dE(\phi)/d\tau = -\sum(\phi_i')^2 \le 0$ along the trajectories of (10.15), with equality only at equilibria.

10.3.4 Mean-Field Approximations

Synchronization of the phase model (10.15) with randomly distributed frequency deviations ω_i can be analyzed in the limit $n \to \infty$, often called the thermodynamic limit by physicists. We illustrate the theory using the special case $H(\chi) = \sin\chi$ (Kuramoto 1975)

$$\varphi_i' = \omega_i + \frac{K}{n}\sum_{j=1}^{n} \sin(\varphi_j - \varphi_i) \ , \qquad \varphi_i \in [0, 2\pi] \ , \tag{10.20}$$

where $K > 0$ is the coupling strength and the factor $1/n$ ensures that the model behaves well as $n \to \infty$. The complex-valued sum of all phases,

$$re^{\mathrm{i}\psi} = \frac{1}{n}\sum_{j=1}^{n} e^{\mathrm{i}\varphi_j} \qquad \text{(Kuramoto synchronization index)}, \tag{10.21}$$

describes the degree of synchronization in the network. The parameter r is often called the *order parameter* by physicists. Apparently, the in-phase synchronized state $\varphi_1 = \cdots = \varphi_n$ corresponds to $r = 1$, with ψ being the population phase. In contrast, the *incoherent* state, with all φ_i having different values randomly distributed on the unit circle, corresponds to $r \approx 0$. (The case $r \approx 0$ can also correspond to two or more clusters of synchronized neurons, oscillating anti-phase or out-of-phase and canceling each other.) Intermediate values of r correspond to a *partially synchronized* or *coherent* state, depicted in Fig.10.33. Some phases are synchronized in a cluster, while others roam around the circle.

Multiplying both sides of (10.21) by $e^{-\mathrm{i}\varphi_i}$ and considering only the imaginary parts, we can rewrite (10.20) in the equivalent form

$$\varphi_i' = \omega_i + Kr\sin(\psi - \varphi_i) \ ,$$

which emphasizes the mean-filed character of interactions between the oscillators: they are all pulled into the synchronized cluster ($\varphi_i \to \psi$) with the effective strength proportional to the cluster size r. This pull is offset by the random frequency deviations ω_i, which pull away from the cluster.

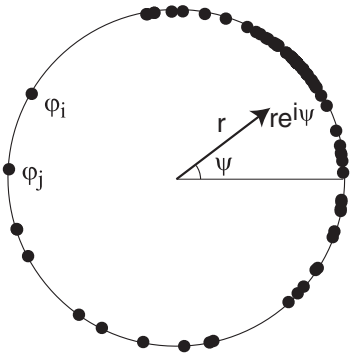

Figure 10.33: The Kuramoto synchronization index (10.21) describes the degree of coherence in the network (10.20).

Let us assume that the frequencies ω_i are distributed randomly around 0 with a symmetric probability density function $g(\omega)$ (e.g., Gaussian). Kuramoto (1975) has shown that in the limit $n \to \infty$, the cluster size r obeys the self-consistency equation

$$r = rK \int_{-\pi/2}^{+\pi/2} g(rK \sin\varphi)\, \cos^2\varphi \, d\varphi \tag{10.22}$$

derived in exercise 21. Note that $r = 0$, corresponding to the incoherent state, is always a solution of this equation. When the coupling strength K is greater than a certain critical value,

$$K_\mathrm{c} = \frac{2}{\pi g(0)} \ ,$$

an additional, nontrivial solution $r > 0$ appears, which corresponds to a partially synchronized state. It scales as $r = \sqrt{16(K - K_\mathrm{c})/(-g''(0)\pi K_\mathrm{c}^4)}$, as the reader can prove by expanding g in a Taylor series. Thus, the stronger the coupling K relative to the random distribution of frequencies, the more oscillators synchronize into a coherent cluster. The issue of stability of incoherent and partially synchronized states is discussed by Strogatz (2000).

10.4 Examples

Below we consider simple examples of oscillators to illustrate the theory developed in this chapter. Our goal is to understand which details of oscillators are important in shaping the PRC, the form of the function H in the phase deviation model, and, hence, the existence and stability of synchronized states.

10.4.1 Phase Oscillators

Let us consider the simplest possible kind of a nonlinear oscillator, known as the *phase oscillator*:

$$\dot{x} = f(x) + \varepsilon p(t) \ , \qquad x \in \mathbb{S}^1 \ , \tag{10.23}$$

where $f(x) > 0$ is a periodic function, for example, $f(x) = a + \sin x$ with $a > 1$. Note that this kind of oscillator is quite different from the two- or high-dimensional

conductance-based models with limit cycle attractors that we considered in the earlier chapters. Here, the state variable x is one-dimensional, defined on a circle $\mathbb{S}^1$. It may be interpreted as a measure of distance along a limit cycle attractor of a multi-dimensional system.

Consider the unperturbed ($\varepsilon = 0$) phase oscillator $\dot{x} = f(x)$, and let $x(t)$ be its solution with some period $T > 0$. Following Kuramoto's idea, we substitute $x(\vartheta)$ into (10.23) and use the chain rule,

$$f(x(\vartheta)) + \varepsilon p(t) = \{x(\vartheta)\}' = x'(\vartheta)\,\vartheta' = f(x(\vartheta))\vartheta' \,,$$

to get the new phase equation

$$\dot{\vartheta} = 1 + \varepsilon p(t)/f(x(\vartheta)) \,, \tag{10.24}$$

which is equivalent to (10.23) for any, not necessarily small, ε.

We can also obtain (10.24) by using any of the three methods of reduction of oscillators to phase models:

- *Malkin's* method is the easiest one. We do not even have to solve the one-dimensional adjoint equation (10.10) having the form $\dot{Q} = -f'(x(t))\,Q$, because we can obtain the solution $Q(t) = 1/f(x(t))$ directly from the normalization condition $Q(t)f(x(t)) = 1$.

- *Kuramoto's* method relies on the function $\vartheta(x)$, which we can find implicitly. Since the phase at a point $x(t)$ on the limit cycle is t, $x(\vartheta)$ is the inverse of $\vartheta(x)$. Using the rule for differentiating of inverse functions, $\vartheta'(x) = 1/x'(\vartheta)$, we find $\operatorname{grad}\vartheta = 1/f(x(\vartheta))$.

- *Winfree's* method relies on $\mathrm{PRC}\,(\vartheta)$, which we find using the following procedure: A pulsed perturbation at phase ϑ moves the solution from $x(\vartheta)$ to $x(\vartheta) + A$, which is $x(\vartheta + \mathrm{PRC}\,(\vartheta, A)) \approx x(\vartheta) + x'(\vartheta)\mathrm{PRC}\,(\vartheta, A)$ when A is small. Hence, $\mathrm{PRC}\,(\vartheta, A) \approx A/x'(\vartheta) = A/f(x(\vartheta))$, and the linear response is $Z(\vartheta) = 1/f(x(\vartheta))$ when $A \to 0$.

Two coupled identical oscillators

$$\begin{aligned} \dot{x}_1 &= f(x_1) + \varepsilon g(x_2) \\ \dot{x}_2 &= f(x_2) + \varepsilon g(x_1) \end{aligned}$$

can be reduced to the phase model (10.17) with $G(\chi) = H(-\chi) - H(\chi)$, where

$$H(\chi) = \frac{1}{T}\int_0^T Q(t)\,g(x(t+\chi))\,dt = \frac{1}{T}\int_0^T \frac{g(x(t+\chi))}{f(x(t))}\,dt \,.$$

The condition for exponential stability of the in-phase synchronized state, $\chi = 0$, can be expressed in the following three equivalent forms

$$\int_0^T g'(x(t))\,dt > 0 \qquad \text{or} \qquad \int_{\mathbb{S}^1} \frac{g'(x)}{f(x)}\,dx > 0 \qquad \text{or} \qquad \int_{\mathbb{S}^1} \frac{f'(x)}{f^2(x)}\,g(x)\,dx > 0 \,, \tag{10.25}$$

as we prove in exercise 24.

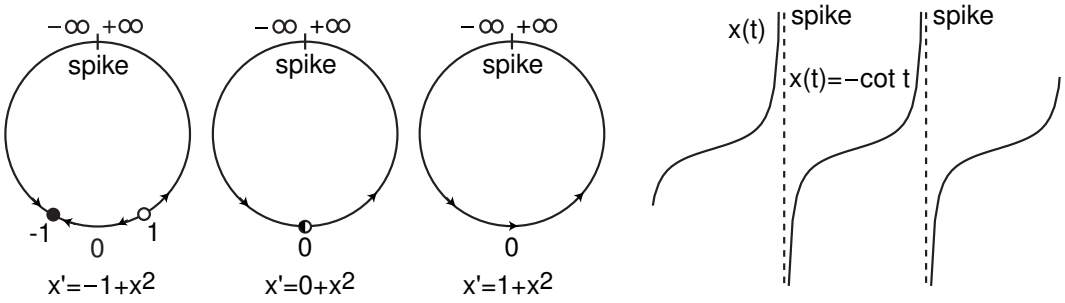

Figure 10.34: Phase portraits and typical oscillations of the quadratic integrate-and-fire neuron $\dot{x} = I + x^2$ with $x \in \mathbb{R} \cup \{\pm\infty\}$. Parameter: $I = -1, 0, +1$.

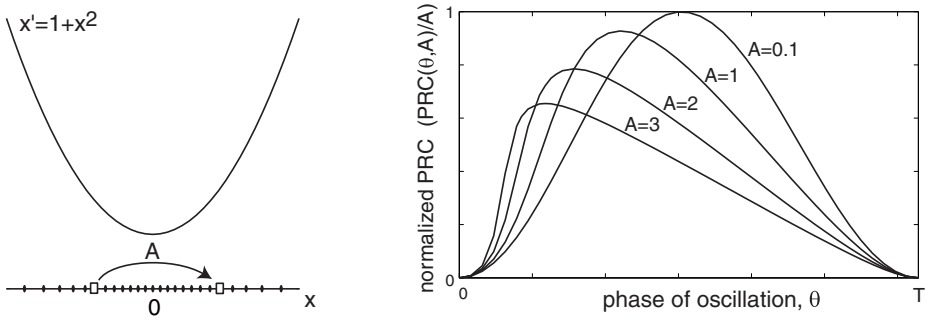

Figure 10.35: The dependence of the PRC of the quadratic integrate-and-fire model on the strength of the pulse A.

10.4.2 SNIC Oscillators

Let us go through all the steps of derivation of the phase equation using a neuron model exhibiting low-frequency periodic spiking. Such a model is near the saddle-node on invariant circle (SNIC) bifurcation studied in section 6.1.2. Appropriate rescaling of the membrane potential and time converts the model into the normal form

$$x' = 1 + x^2 \,, \qquad x \in \mathbb{R} \,.$$

Because of the quadratic term, x escapes to infinity in a finite time, producing a spike depicted in Fig.10.34. If we identify $-\infty$ and $+\infty$, then x exhibits periodic spiking of infinite amplitude. Such a spiking model is called a quadratic integrate-and-fire (QIF) neuron (see also section 8.1.3 for some generalizations of the model).

Strong Pulse

The solution of this system, starting at the spike, that is, at $x(0) = \pm\infty$, is

$$x(t) = -\cot t \,,$$

as the reader can check by differentiating. It is a periodic function with $T = \pi$; hence, we can introduce the phase of oscillation via the relation $x = -\cot\vartheta$. The

corresponding PRC can be found explicitly (see exercise 9) and it has the form

$$\mathrm{PRC}\,(\vartheta, A) = \pi/2 + \,\mathrm{atan}\,(A - \cot\vartheta) - \vartheta\ ,$$

depicted in Fig.10.35, where A is the magnitude of the pulse. Note that the PRC tilts to the left as A increases. Indeed, the density of isochrons, denoted by black points on the x-axis in the figure, is maximal at the ghost of the saddle-node point $x = 0$, where the parabola $1 + x^2$ has the knee. This corresponds to the inflection point of the graph of $x(t)$ in Fig.10.34, where the dynamics of $x(t)$ is the slowest. The effect of a pulse is maximal just before the ghost because x can jump over the ghost and skip the slow region. The stronger the pulse, the earlier it should arrive; hence the tilt.

Weak Coupling

The PRC behaves as $A\sin^2\vartheta$, with $\vartheta \in [0, \pi]$, when A is small, as the reader can see in Fig.10.35 or prove by differentiating the function $\mathrm{PRC}\,(\vartheta, A)$ with respect to A. Therefore, $Z(\vartheta) = \sin^2\vartheta$, and we can use Winfree's approach to transform the weakly perturbed quadratic integrate-and-fire (QIF) oscillator

$$x' = 1 + x^2 + \varepsilon p(t)$$

into its phase model

$$x' = 1 + \varepsilon(\sin^2\vartheta)p(t)\ , \qquad \vartheta \in [0, \pi]\ .$$

The results of the previous section, $Q(\vartheta) = 1/f(x(\vartheta)) = 1/(1+\cot^2\vartheta) = \sin^2\vartheta$, confirm the phase model. In fact, any neuronal model $C\dot{V} = I - I_\infty(V)$ near saddle-node on invariant circle bifurcation point $(I_{\mathrm{sn}}, V_{\mathrm{sn}})$ has infinitesimal PRC:

$$\mathrm{PRC}\,(\vartheta) = \frac{C}{I - I_{\mathrm{sn}}}\sin^2\vartheta\ , \qquad \vartheta \in [0, \pi]\ ,$$

as the reader can prove as an exercise. The function $\sin^2\vartheta$ has the same form as $(1 - \cos\theta)$ if we change variables $\theta = 2\vartheta$ (notice the font difference). The change of variables scales the period from π to 2π.

In Fig.10.36a we compare the function with numerically obtained PRCs for the $I_{\mathrm{Na}} + I_{\mathrm{K}}$-model in the Class 1 regime. Since the ghost of the saddle-node point, revealing itself as an inflection of the voltage trace in Fig.10.36b, moves to the right as I increases away from the bifurcation value $I = 4.51$, so does the peak of the PRC.

Figure 10.36a emphasizes the common features of all systems undergoing saddle-node on invariant circle bifurcation: they are insensitive to the inputs arriving during the spike, since $\mathrm{PRC} \approx 0$ when $\vartheta \approx 0, T$. The oscillators are most sensitive to the input when they are just entering the ghost of the resting state, where PRC is maximal. The location of the maximum tilts to the left as the strength of the input increases, and may tilt to the right as the distance to the bifurcation increases. Finally, PRCs are non-negative, so positive (negative) inputs can only advance (delay) the phase of oscillation.

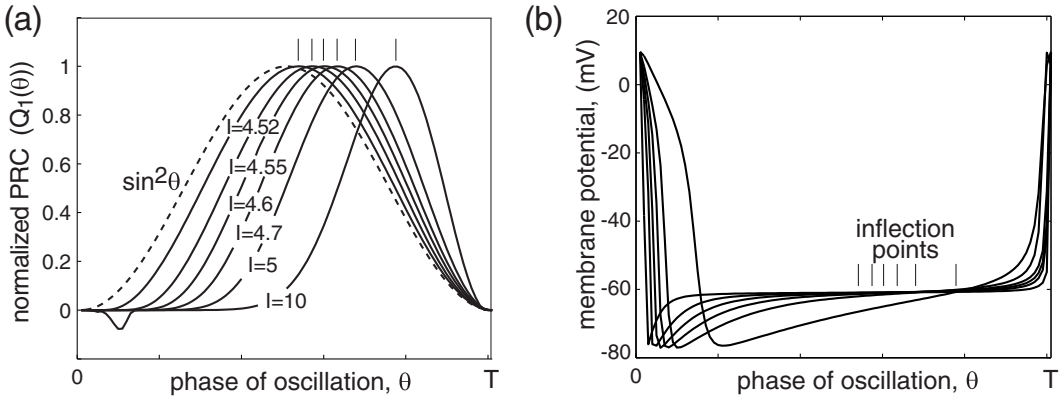

Figure 10.36: (a) Numerically found PRCs of the $I_{\rm Na} + I_{\rm K}$-oscillator in Class 1 regime (parameters as in Fig.4.1a) and various I using the MATLAB program in exercise 12. (b) Corresponding voltage traces show that the inflection point (slowest increase) of V moves right as I increases.

Gap Junctions

Now consider two oscillators coupled via gap junctions (discussed in section 2.3.4):

$$\begin{aligned} x_1' &= 1 + x_1^2 + \varepsilon(x_2 - x_1) \ , \\ x_2' &= 1 + x_2^2 + \varepsilon(x_1 - x_2) \ . \end{aligned}$$

Let us determine the stability of the in-phase synchronized state $x_1 = x_2$. The corresponding phase model (10.12) has the form

$$\begin{aligned} \vartheta_1' &= 1 + \varepsilon(\sin^2\vartheta_1)(\cot\vartheta_1 - \cot\vartheta_2) \ , \\ \vartheta_2' &= 1 + \varepsilon(\sin^2\vartheta_2)(\cot\vartheta_2 - \cot\vartheta_1) \ . \end{aligned}$$

The function (10.16) can be found analytically:

$$H(\chi) = \frac{1}{\pi}\int_0^\pi \sin^2 t\,(\cot t - \cot(t+\chi))\ dt = \frac{1}{2}\sin 2\chi \ ,$$

so that the model in the phase deviation coordinates, $\vartheta(t) = t + \varphi$, has the form

$$\begin{aligned} \varphi_1' &= (\varepsilon/2)\sin\{2(\varphi_2 - \varphi_1)\} \ , \\ \varphi_2' &= (\varepsilon/2)\sin\{2(\varphi_1 - \varphi_2)\} \ . \end{aligned}$$

The phase difference, $\chi = \varphi_2 - \varphi_1$, satisfies the equation (compare with Fig.10.26)

$$\chi' = -\varepsilon\sin 2\chi \ ,$$

and, apparently, the in-phase synchronized state, $\chi = 0$, is always stable while the anti-phase state $\chi = \pi/2$ is not.

Weak Pulses

Now consider two weakly pulse-coupled oscillators

$$\begin{aligned} x_1' &= 1 + x_1^2 + \varepsilon_1 \delta(t - t_2) \, , \\ x_2' &= 1 + x_2^2 + \varepsilon_2 \delta(t - t_1) \, , \end{aligned}$$

where t_1 and t_2 are the moments of firing ($x(t) = \infty$) of the first and the second oscillator, respectively, and ε_1 and ε_2 are the strengths of synaptic connections. The corresponding phase model (10.12) has the form

$$\begin{aligned} \vartheta_1' &= 1 + \varepsilon_1 (\sin^2 \vartheta_1) \delta(t - t_2) \\ \vartheta_2' &= 1 + \varepsilon_2 (\sin^2 \vartheta_2) \delta(t - t_1) \, . \end{aligned}$$

Since

$$H(\chi) = \frac{1}{\pi} \int_0^\pi \sin^2 t \, \delta(t + \chi) \, dt = \frac{1}{\pi} \sin^2 \chi \, ,$$

the corresponding phase deviation model (10.15) is

$$\begin{aligned} \varphi_1' &= \frac{\varepsilon_1}{\pi} \sin^2(\varphi_2 - \varphi_1) \, , \\ \varphi_2' &= \frac{\varepsilon_2}{\pi} \sin^2(\varphi_1 - \varphi_2) \, . \end{aligned}$$

The phase difference $\chi = \varphi_2 - \varphi_1$ satisfies the equation

$$\chi' = \frac{\varepsilon_2 - \varepsilon_1}{\pi} \sin^2 \chi,$$

which becomes $\chi' = 0$ when the coupling is symmetric. In this case, the oscillators preserve (on average) the initial phase difference. When $\varepsilon_1 \neq \varepsilon_2$, the in-phase synchronized state $\chi = 0$ is only neutrally stable. Interestingly, it becomes exponentially unstable in a network of three or more pulse-coupled Class 1 oscillators (see exercise 23).

Weak Pulses with Delays

The synchronization properties of weakly pulse-coupled oscillators can change significantly when explicit axonal conduction delays are introduced. As an example, consider the system

$$\begin{aligned} x_1' &= 1 + x_1^2 + \varepsilon \delta(t - t_2 - d) \, , \\ x_2' &= 1 + x_2^2 + \varepsilon \delta(t - t_1 - d) \, , \end{aligned}$$

where $d \geq 0$ is the delay. exercise 18 shows that delays introduce simple phase shifts, so that the phase model has the form

$$\begin{aligned} \varphi_1' &= \frac{\varepsilon}{\pi} \sin^2(\varphi_2 - \varphi_1 - d) \, , \\ \varphi_2' &= \frac{\varepsilon}{\pi} \sin^2(\varphi_1 - \varphi_2 - d) \, , \end{aligned}$$

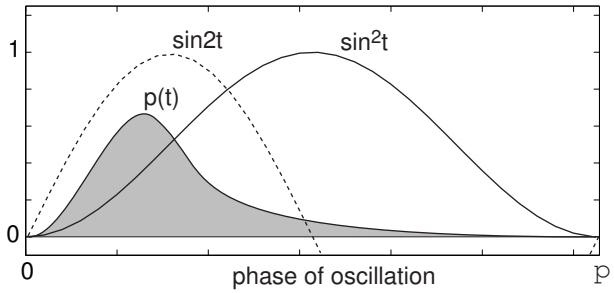

Figure 10.37: Synaptic transmission function $p(t)$ typically has an asymmetric shape with fast rise and slow decay.

The phase difference $\chi = \varphi_2 - \varphi_1$ satisfies

$$\chi' = \frac{\varepsilon}{\pi}\left(\sin^2(\chi + d) - \sin^2(\chi - d)\right) = \frac{\varepsilon \sin 2d}{\pi} \sin 2\chi \ .$$

The stability of synchronized states is determined by the sign of the function $\sin 2d$. The in-phase state $\chi = 0$ is unstable when $\sin 2d > 0$, that is, when the delay is shorter than the half-period $\pi/2$, stable when the delay is longer than the half-period but shorter than one period π, unstable for even longer delays, and so on. The stability of the anti-phase state $\chi = \pi/2$ is reversed, that is, it is stable for short delays, unstable for longer delays, then stable again for even longer delays, and so on. Finally, when the pulses are inhibitory ($\varepsilon < 0$), the (in)stability character is flipped so that the in-phase state becomes stable for short delays.

Weak Synapses

Now suppose that each pulse is not a delta function, but is smeared in time (i.e., it has a time course $p(t - t_i)$ with $p(0) = p(\pi) = 0$). That is, the synaptic transmission starts right after the spike of the presynaptic neuron and ends before the onset of the next spike. The function p has a typical unimodal shape with fast rise and slow decay, depicted in Fig.10.37. The discussion below is equally applicable to the case of $p(t, x) = g(t)(E - x)$ with $g > 0$ being the synaptic conductance with the shape in the figure and E being the synaptic reverse potential, positive (negative) for excitatory (inhibitory) synapses.

Two weakly synaptically coupled SNIC (Class 1) oscillators

$$\begin{aligned} x_1' &= 1 + x_1^2 + \varepsilon p(t - t_2) \ , \\ x_2' &= 1 + x_2^2 + \varepsilon p(t - t_1) \end{aligned}$$

can be converted into a general phase model with the connection function (10.16) in the form

$$H(\chi) = \frac{1}{\pi} \int_0^\pi \sin^2 t \, p(t + \chi) \, dt \ ,$$

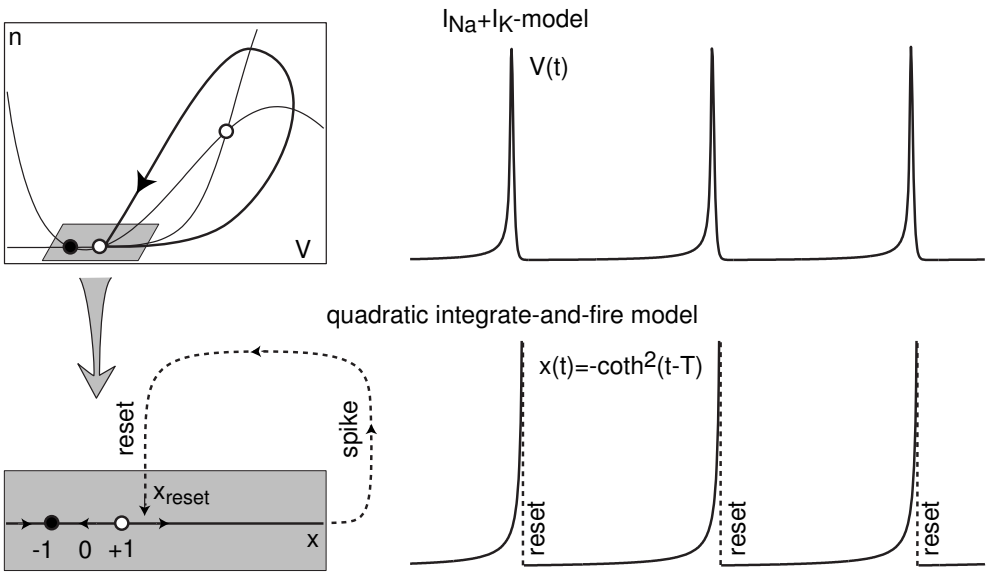

Figure 10.38: Top. Periodic spiking of the $I_{\rm Na}+I_{\rm K}$-neuron near saddle-node homoclinic orbit bifurcation (parameters as in Fig.4.1a with $\tau(V)=0.167$ and $I=4.49$). Bottom. Spiking in the corresponding quadratic integrate-and-fire model.

and it can be computed explicitly for some simple $p(t)$.

The in-phase synchronized solution, $\chi=0$, is stable when

$$H'(0)=\frac{1}{\pi}\int_0^\pi \sin^2 t\, p'(t)\, dt > 0\ .$$

Since the function $\sin^2 t$ depicted in Fig.10.37 is small at the ends of the interval and large in the middle, the integral is dominated by the sign of p' in the middle. Fast-rising and slowly decaying excitatory ($p>0$) synaptic transmission has $p'<0$ in the middle (as in the figure), so the integral is negative and the in-phase solution is unstable. In contrast, fast-rising slowly decaying inhibitory ($p<0$) synaptic transmission has $p'>0$ in the middle, so the integral is positive and the in-phase solution is stable. Another way to see this is to integrate the equation by parts, reduce it to $-\int p(t)\sin 2t\, dt$, and note that $p(t)$ is concentrated in the first (left) half of the period, where $\sin 2t$ is positive. Hence, positive (excitatory) p results in $H'(0)<0$, and vice versa. Both approaches confirm the theoretical results independently obtained by van Vreeswijk et al. (1994) and Hansel et al. (1995) that *inhibition, not excitation, synchronizes Class 1 (SNIC) oscillators*. The relationship is inverted for the anti-phase solution $\chi=\pi/2$ (the reader should prove this), and no relationships are known for other types of oscillators.

10.4.3 Homoclinic Oscillators

Besides the SNIC bifurcation considered above, low-frequency oscillations may also indicate the proximity of the system to a saddle homoclinic orbit bifurcation, as in

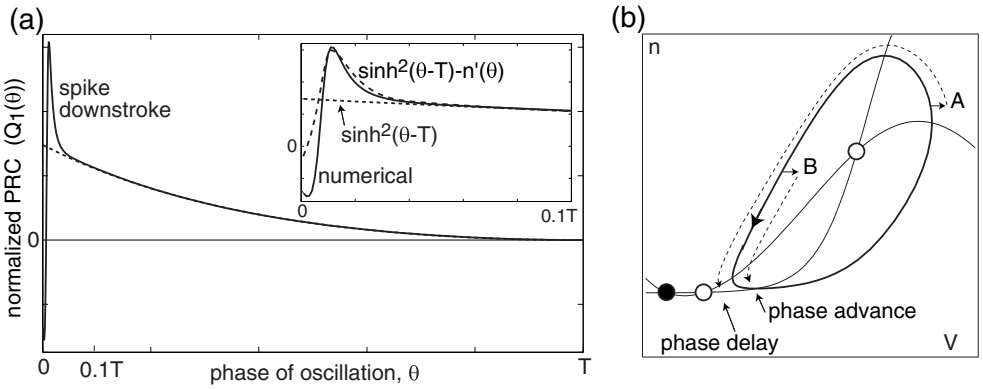

Figure 10.39: (a) Numerically found PRCs of the $I_{\rm Na}+I_{\rm K}$-oscillator near saddle-node homoclinic orbit bifurcation (as in Fig.10.38), using the MATLAB program in exercise 12. Magnification shows the divergence from the theoretical curve $\sinh^2(\vartheta - T)$ during the spike. (b) A pulsed input during the downstroke of the spike can produce a significant phase delay (pulse A) or advance (pulse B) not captured by the quadratic integrate-and-fire model.

Fig.10.38 (top). The spiking trajectory in the figure quickly approaches a small shaded neighborhood of the saddle along the stable direction, and then slowly diverges from the saddle along the unstable direction, thereby resulting in a large-period oscillation. As often the case in neuronal models, the saddle equilibrium is near a stable node equilibrium corresponding to the resting state, and the system is near the codimension-2 saddle-node homoclinic orbit bifurcation studied in section 6.3.6. As a result, there is a drastic difference between the attraction and divergence rates to the saddle, so that the dynamics in the shaded neighborhood of the saddle-node in the figure can be reduced to the one-dimensional V-equation, which in turn can be transformed into the "quadratic integrate-and-fire" form

$$x' = -1 + x^2 \ , \qquad \text{if } x = +\infty, \text{ then } x \leftarrow x_{\rm reset} \ ,$$

with solutions depicted in Fig.10.38 (bottom). The saddle and the node correspond to $x = +1$ and $x = -1$, respectively. One can check by differentiating that the solution of the model with $x(0) = x_{\rm reset} > 1$ is $x(t) = -\coth(t - T)$, where $\coth(s) = (e^s + e^{-s})/(e^s - e^{-s})$ is the hyperbolic cotangent and $T = \operatorname{acoth}(x_{\rm reset})$ is the period of oscillation, which becomes infinite as $x_{\rm reset} \to 1$.

Using the results of section 10.4.1, we find the function

$$Q(\vartheta) = 1/(-1 + \coth^2(\vartheta - T)) = \sinh^2(\vartheta - T)$$

whose graph is shown in Fig.10.39a. For comparison, we plotted the numerically found PRC for the $I_{\rm Na}+I_{\rm K}$-oscillator to illustrate the disagreement between the theoretical and numerical curves in the region $\vartheta < 0.1T$ corresponding to the downstroke of the spike. Such a disagreement is somewhat expected, since the quadratic integrate-and-fire model ignores spike downstroke. If a pulse arriving during the downstroke

displaces the trajectory to the exterior of the limit cycle (as in Fig.10.39b, pulse A), then the trajectory becomes closer to the saddle equilibrium when it reenters a small neighborhood of the saddle, thereby leading to a significant phase delay. Displacements to the interior of the cycle (as in Fig.10.39b, pulse B) push away from the saddle and lead to phase advances. The direction and the magnitude of displacements are determined by the derivative of the slow variable n' along the limit cycle.

The region of disagreement between theoretical and numerical PRCs becomes infinitesimal relative to $T \to \infty$ near the bifurcation. Theoretical PRC can be used to study anti-phase and out-of-phase synchronization of pulse-coupled oscillators, but not of in-phase synchronization, because the region of breakdown is the only important region in this case. Finally, note that as $T \to \infty$, the spiking limit cycle fails to be exponentially stable, and the theory of weakly coupled oscillators is no longer applicable to it.

Though the PRC in Fig.10.39 is quite different from the one corresponding to SNIC oscillators in Fig.10.36, there is an interesting similarity between these two cases: both can be reduced to quadratic integrate-and-fire neurons, and both have cotangent-shaped periodic spiking solutions and sine-squared-shape PRCs, except that they are "regular" in the SNIC case and hyperbolic in the homoclinic case (see also exercise 26).

10.4.4 Relaxation Oscillators and FTM

Consider two relaxation oscillators having weak fast → fast connections

$$\begin{aligned} \mu \dot{x}_i &= f(x_i, y_i) + \varepsilon p_i(x_i, x_k) \ , \\ \dot{y}_i &= g(x_i, y_i) \ , \end{aligned} \tag{10.26}$$

where $i = 1, 2$ and $k = 2, 1$. This system can be converted to a phase model in the relaxation limit $\varepsilon \ll \mu \to 0$ (Izhikevich 2000b). The connection functions $H_i(\chi)$ have a positive discontinuity at $\chi = 0$, which occurs because the x-coordinate of the relaxation limit cycle is discontinuous at the jump points. Hence, the phase difference function $G(\chi) = H_2(-\chi) - H_1(\chi)$ has a negative discontinuity at $\chi = 0$ (depicted in Fig.10.31). This reflects the profound difference between behaviors of weakly coupled oscillators of the relaxation and non-relaxation types, discussed in section 10.3.1: The in-phase synchronized solution, $\chi = 0$, in the relaxation limit $\mu \to 0$ is stable and persistent in the presence of the frequency mismatch ω, and it has a rapid rate of convergence. The reduction to a phase model breaks down when $\varepsilon \gg \mu \to 0$, that is, when the connections are relatively strong. One can still analyze such oscillators in the special case considered below.

Fast Threshold Modulation

Consider (10.26) and suppose that $p_1 = p_2 = p$ is a piecewise constant function: $p = 1$ when the presynaptic oscillator, x_k, is on the right branch of the cubic x-nullcline corresponding to an active state, and $p = 0$ otherwise (see Fig.10.40a). Somers and

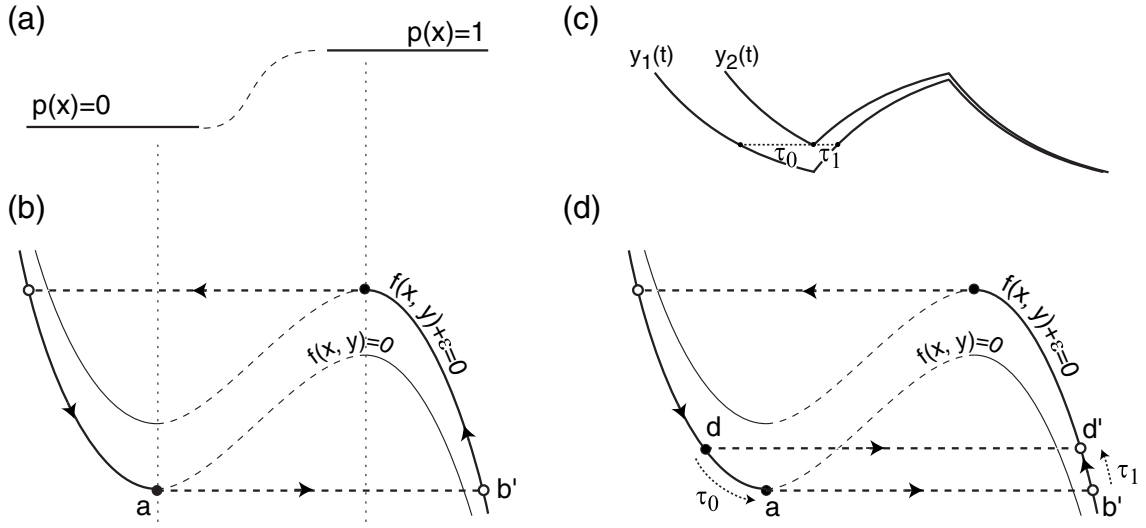

Figure 10.40: Fast threshold modulation of relaxation oscillation. (a) The Heaviside or sigmoidal coupling function $p(x)$ is constant while x is on the left or right branch of the x-nullcline. (b) In the relaxation limit $\mu = 0$, the synchronized limit cycle consists of the left branch of the nullcline $f(x, y) = 0$ and the right branch of the nullcline $f(x, y) + \varepsilon = 0$. When oscillator 1 is ahead of oscillator 2 (c), the phase difference between them decreases after the jump (d).

Kopell (1993, 1995) referred to such a coupling in the relaxation limit $\mu \to 0$ as fast threshold modulation (FTM), and found a simple criterion of stability of synchronized state that works even for strong coupling.

Since the oscillators are identical, the in-phase synchronized state exists, during which the variables x_1 and x_2 follow the left branch of the x-nullcline defined by $f(x, y) = 0$ (see Fig.10.40b) until they reach the jumping point a. During the instantaneous jump, they turn on the mutual coupling ε, and land at some point b' on the perturbed x-nullcline defined by $f(x, y) + \varepsilon = 0$. They follow the new nullcline to the right (upper) knee, and then jump back to the left branch.

To determine the stability of the in-phase synchronization, we consider the case when oscillator 1 is slightly ahead of oscillator 2, as in Fig.10.40c. We assume that the phase difference between the oscillators is so small – or alternatively, the strength of coupling is so large – that when oscillator 1 jumps and turns on its input to oscillator 2, the latter, being at point d in Fig.10.40d, is below the left knee of the perturbed x-nullcline $f(x, y) + \varepsilon = 0$ and therefore jumps, too. As a result, both oscillators jump to the perturbed x-nullcline and reverse their order. Although the apparent distance between the oscillators, measured by the difference of their y-coordinates, is preserved during such a jump, the phase difference between them usually is not.

The phase difference between two points on a limit cycle is the time needed to travel from one point to the other. Let $\tau_0(d)$ be the time needed to slide from point d to point a along the x-nullcline in Fig.10.40d (i.e., the phase difference just before

the jump). Let $\tau_1(d)$ be the time needed to slide from point b' to point d' (i.e., the phase difference after the jump). The phase difference between the oscillators during the jump changes by the factor $C(d) = \tau_1(d)/\tau_0(d)$, called the *compression function*. The difference decreases when the compression function $C(d) < 1$ uniformly for all d near the left knee a. This condition has a simple geometrical meaning: the rate of change of $y(t)$ is slower before the jump than after it, so that $y(t)$ has a "scalloped" shape, as in Fig.10.40c. As an exercise, prove that $C(d) \to |g(a)|/|g(b')|$ as $d \to a$.

If the compression function at the right (upper) knee is also less than 1, then the in-phase synchronization is stable. Indeed, the phase difference does not change while the oscillators slide along the nullclines, and it decreases geometrically with each jump. In fact, it suffices to require that the product of compression factors at the two knees be less than 1, so that any expansion at one knee is compensated for by even stronger compression at the other knee.

10.4.5 Bursting Oscillators

Let us consider bursting neurons coupled weakly through their fast variables:

$$\dot{x}_i = f(x_i, y_i) + \varepsilon p(x_i, x_j) \,, \tag{10.27}$$

$$\dot{y}_i = \mu g(x_i, y_i) \,, \tag{10.28}$$

$i = 1, 2$ and $j = 2, 1$. Since bursting involves two time scales, fast spiking and slow transition between spiking and resting, there are two synchronization regimes: spike synchronization and burst synchronization, illustrated in Fig.9.51 and discussed in section 9.4. Below, we outline some useful ideas and methods of studying both regimes. Our exposition is not complete, but it lays the foundation for a more detailed research program.

Spike Synchronization

To study synchronization of individual spikes within the burst, we let $\mu = 0$ in order to freeze the slow subsystem (10.28), and consider the fast subsystem (10.27) describing weakly coupled oscillators. When $y_i \approx y_j$, the fast variables oscillate with approximately equal periods, so (10.27) can be reduced to the phase model

$$\dot{\varphi}_i = \varepsilon H(\varphi_j - \varphi_i,\ y_i) \,,$$

where $y_i = \text{const}$ parameterize the form of the connection function. For example, during the "circle/Hopf" burst, the function is transformed from $H(\chi) = \sin^2 \chi$ or $1 - \cos \chi$ at the beginning of the burst (saddle-node on invariant circle bifurcation) to $H(\chi) = \sin \chi$ at the end of the burst (supercritical Andronov-Hopf bifurcation). Changing y_i slowly, one can study when spike synchronization appears and when it disappears during the burst. When the slow variables y_i have different values, fast variables typically oscillate with different frequencies, so one needs to look at low-order resonances to study the possibility of spike synchronization.

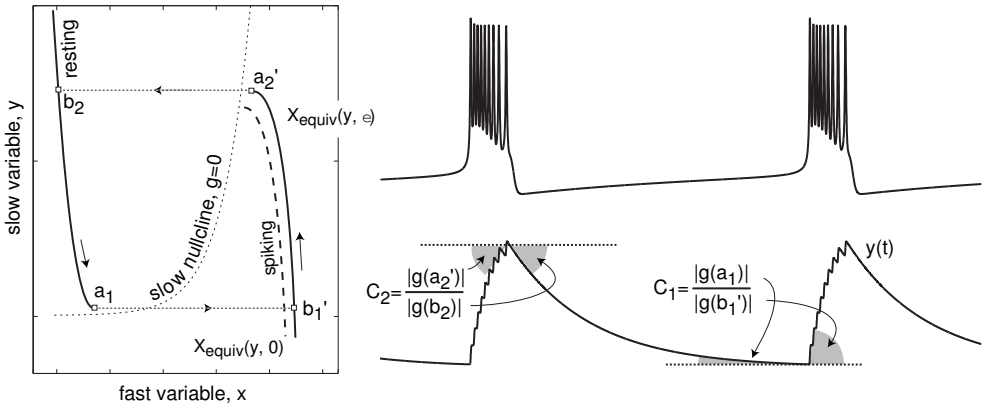

Figure 10.41: Reduction of the $I_{\mathrm{Na,p}}$+I_{K}+$I_{\mathrm{K(M)}}$-burster to a relaxation oscillator. The slow variable exhibits "scalloped" oscillations needed for stability of in-phase burst synchronization. C_1 and C_2 are compression functions at the two jumps.

Burst synchronization

In chapter 9 we presented two methods, averaging and equivalent voltage, that remove fast oscillations and reduce bursters to slow relaxation oscillators. Burst synchronization is then reduced to synchronization of such oscillators, and it can be studied using phase reduction or fast threshold modulation (FTM) approaches.

To apply FTM, we assume that the coupling in (10.27) is piecewise constant, that is, $p(x_i, x_j) = 0$ when the presynaptic burster x_j is resting, and $p(x_i, x_j) = 1$ (or any function of x_i) when the presynaptic burster is spiking. We also assume that the slow subsystem (10.28) is one-dimensional, so that we can use the equivalent voltage method (section 9.2.4) and reduce the coupled system to

$$\begin{aligned} 0 &= X_{\mathrm{equiv}}(y_i, \varepsilon p) - x_i \ , \\ y_i' &= g(x_i, y_i) \ . \end{aligned}$$

When the burster is of the hysteresis loop type (i.e., the resting and spiking states coexist), the function $x = X_{\mathrm{equiv}}(y, \varepsilon p)$ often, but not always, has a Z-shape on the slow/fast plane, as in Fig.9.16, so that the system corresponds to a relaxation oscillator with nullclines as in Fig.10.41. Fast threshold modulation occurs via the constant εp, which shifts the fast nullcline up or down. The compression criterion for stability of the in-phase burst synchronization, presented in the previous section, has a simple geometrical illustration in the figure. The slow nullcline has to be sufficiently close to the jumping points that $y(t)$ slows before each jump and produces the "scalloped" curve. Many hysteresis loop fast/slow bursters do generate such a shape. In particular, "fold/*" bursters exhibit robust in-phase burst synchronization when they are near the bifurcation from quiescence to bursting, since the slow nullcline is so close to the left knee that the compression during the resting $\rightarrow$ spiking jump (C_1 in Fig.10.41) dominates the expansion, if any, during the spiking $\rightarrow$ resting jump.

Review of Important Concepts

- Oscillations are described by their phase variables ϑ rotating on a circle $\mathbb{S}^1$. We define ϑ as the time since the last spike.
- The phase response curve, PRC (ϑ), describes the magnitude of the phase shift of an oscillator caused by a strong pulsed input arriving at phase ϑ.
- PRC depends on the bifurcations of the spiking limit cycle, and it defines synchronization properties of an oscillator.
- Two oscillators are synchronized in-phase, anti-phase, or out-of-phase when their phase difference, $\vartheta_2 - \vartheta_1$, equals 0, half-period, or some other value, respectively; see Fig.10.42.
- Synchronized states of pulse-coupled oscillators are fixed points of the corresponding Poincare phase map.
- Weakly coupled oscillators

  $$\dot{x}_i = f(x_i) + \varepsilon \sum g_{ij}(x_j)$$

  can be reduced to phase models

  $$\dot{\vartheta}_i = 1 + \varepsilon\, Q(\vartheta_i) \sum g_{ij}(x_j(\vartheta_j)) \ ,$$

  where $Q(\vartheta)$ is the infinitesimal PRC defined by (10.10).
- Weak coupling induces a slow phase deviation of the natural oscillation, $\vartheta_i(t) = t + \varphi_i$, described by the averaged model

  $$\dot{\varphi}_i = \varepsilon \left(\omega_i + \sum H_{ij}(\varphi_j - \varphi_i) \right) \ ,$$

  where ω_i denote the frequency deviations, and

  $$H_{ij}(\varphi_j - \varphi_i) = \frac{1}{T} \int_0^T Q(t)\ g_{ij}(x_j(t + \varphi_j - \varphi_i))\, dt$$

  describes the interactions between the phases.
- Synchronization of two coupled oscillators corresponds to equilibria of the one-dimensional system

  $$\dot{\chi} = \varepsilon(\omega + G(\chi)) \ , \qquad \chi = \varphi_2 - \varphi_1 \ ,$$

  where $G(\chi) = H_{21}(-\chi) - H_{12}(\chi)$ describes how the phase difference χ compensates for the frequency mismatch $\omega = \omega_2 - \omega_1$.

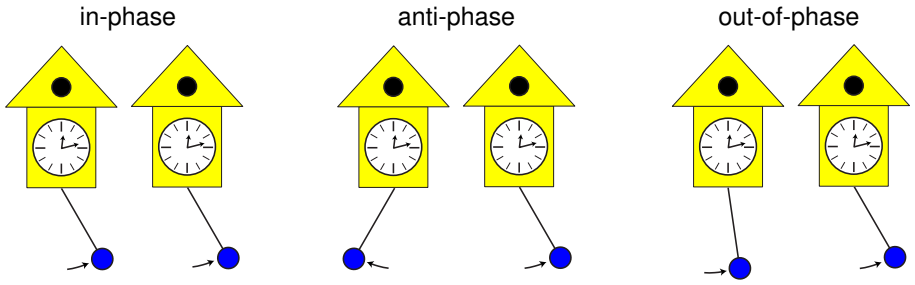

Figure 10.42: Different types of synchronization.

Bibliographical Notes

Surprisingly, this chapter turned out to be quite different from chapter 9 ("Weakly Connected Oscillators") of the book *Weakly Connected Neural Networks* by Hoppensteadt and Izhikevich (1997) and from the book *Synchronization: A Universal Concept in Nonlinear Sciences* by Pikovsky, Rosenblum, and Kurths (2001). All three texts, though devoted to the same subject, do not repeat, but rather complement, each other. The last provides an excellent historical overview of synchronization, starting with the work of the famous Dutch mathematician, astronomer, and physicist Christiaan Huygens (1629–1695), who was the first to describe synchronization of two pendulum clocks hanging from a common support (which was, incidentally, anti-phase). While providing many examples of synchronization of biological, chemical, and physical systems, the book by Pikovsky et al. also discusses the definition of a phase and synchronization of nonperiodic, e.g., chaotic, oscillators, a topic not covered here. A major part of *Spiking Neuron Models* by Gerstner and Kistler (2002) is devoted to synchronization of spiking neurons, with the emphasis on the integrate-and-fire model and the spike-response method.

The formalism of the phase response curve (PRC) was introduced by Hastings and Sweeney (1958), and it has been used extensively in the context of resetting the circadian rhythms. "Forty Years of PRC – What Have We Learned?" by Johnson (1999) gives a historical overview of this idea and some recent developments. John Guckenheimer (1975) used the theory of normally hyperbolic invariant manifolds to provide a mathematical foundation for the existence of isochrons, and their geometrical properties. An encyclopedic exposition on isochrons and phase-resettings in nature, as well as numerous anecdotes, can be found in Arthur Winfree's remarkable book *The Geometry of Biological Time* (1980, 2nd ed., 2001). In particular, Winfree describes the work of George R. Mines (1914), who was doing phase-resetting experiments by shocking rabbits at various phases of their heartbeat. He found the phase and shock that could stop a rabbit's heart (black hole in Fig.10.8), and then applied it to himself. He died.

Glass and Mackey (1988) provide a detailed exposition of circle phase maps. Although the structure of phase-locking regions in Fig.10.15 was discovered by Cartwright and Littlewood (1945), it is better known today as Arnold tongues (Arnold 1965). Gue-

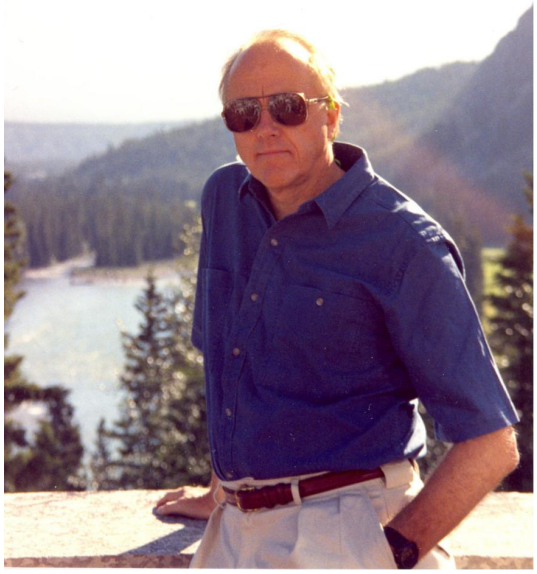

Figure 10.43: Frank Hoppensteadt, the author's adviser and mentor, circa 1989.

vara and Glass (1982) found this structure analytically for the Andronov-Hopf oscillator in Fig.10.3 (radial isochron clock). Hoppensteadt (1997, 2000) provides many examples of oscillatory systems arising in biology and neuroscience (see also Hoppensteadt and Peskin 2002).

Malkin's method of reduction of coupled oscillators to phase equations has been known, at least to Russian scientists, since the early 1950s (Malkin 1949, 1956; Blechman 1971). For example, Melnikov (1963) applied Malkin's theorem to a homoclinic orbit of infinite period to obtain the transversality condition for the saddle homoclinic orbit bifurcation (Kuznetsov 1995).

Malkin's method was rediscovered in the West by Neu (1979), and hoorayed by Winfree (1980), who finally saw a mathematical justification for his usage of phase variables. Since then, the field of phase equations has been largely dominated by Bard Ermentrout and Nancy Kopell (Ermentrout 1981, 1986, 1992; Ermentrout and Kopell 1986a,b, 1990, 1991, 1994; Kopell and Ermentrout 1990; Kopell 1986; Kopell et al. 1991). In particular, they developed the theory of traveling wave solutions in chains of oscillators, building on the seminal paper by Cohen et al. (1982). Incidentally, the one-page proof of Malkin's theorem provided by Hoppensteadt and Izhikevich (1997, Sect. 9.6) is based on Ermentrout and Kopell's idea of using the Fredholm alternative; Malkin's and Neu's proofs are quite long, mostly because they reprove the alternative.

There are only a handful of examples in which the Malkin adjoint problem can be solved analytically (i.e., without resort to simulations). The SNIC, homoclinic and Andronov-Hopf cases are the most important, and have been considered in detail in this chapter. Brown et al. (2004) also derive PRCs for oscillators with homoclinic orbits to pure saddles (see exercise 25) and for Bautin oscillators.

Throughout this chapter we define the phase ϑ or φ on the interval $[0, T]$, where T is the period of free oscillation, and do not normalize it to be on the interval $[0, 2\pi]$.

Figure 10.44: Nancy Kopell in her Boston University office in 1990 (photograph provided by Dr. Kopell).

As a result, we have avoided the annoying terms $2\pi/T$ and $2\pi/\Omega$ in the formulas. The only drawback is that some of the results may have an "unfamiliar look", such as $\sin^2\vartheta$ with $\vartheta \in [0,\pi]$ for the PRC of Class 1 neurons, as opposed to $1-\cos\vartheta$ with $\vartheta \in [0,2\pi]$ used previously by many authors before.

Hansel, Mato, and Meunier (1995) were the first to note that the shape of the PRC determines the synchronization properties of synaptically coupled oscillators. Ermentrout (1996) related this result to the classification of oscillators and proved that PRCs of all Class 1 oscillators have the form of $1-\cos\vartheta$, though the proof can be found in his earlier papers with Kopell (Ermentrout and Kopell 1986a, 1986b). Reyes and Fetz (1993) measured the PRC of a cat neocortical neuron and largely confirmed the theoretical predictions. The experimental method in section 10.2.4 is related to that of Rosenblum and Pikovsky (2001). It needs to be developed further, for instance, by incorporating the measurement uncertainty (error bars). In fact, most experimentally obtained PRCs, including the one in Fig.10.24, are so noisy that nothing useful can be derived from them. This issue is the subject of active research.

Our treatment of the FTM theory in this volume closely follows that of Somers and Kopell (1993, 1995). Anti-phase synchronization of relaxation oscillators is analyzed using phase models by Izhikevich (2000b), and FTM theory, by Kopell and Somers (1995). Ermentrout (1994) and Izhikevich (1998) considered weakly coupled oscillators with axonal conduction delays and showed that delays result in mere phase shifts (see exercise 18). Frankel and Kiemel (1993) observed that slow coupling can be reduced to weak coupling. Izhikevich and Hoppensteadt (2003) used Malkin's theorem to extend the results to slowly coupled networks, and to derive useful formulas for the coupling functions and coefficients. Ermentrout (2003) showed that the result could be generalized to synapses having fast-rising and slow-decaying conductances. Goel

and Ermentrout (2002) and Katriel (2005) obtained interesting results on in-phase synchronization of identical phase oscillators.

Interactions between resonant oscillators were considered by Ermentrout (1981), Hoppensteadt and Izhikevich (1997), and Izhikevich (1999) in the context of quasi-periodic (multi-frequency) oscillations. Baesens et al. (1991) undertook the heroic task of studying resonances and toroidal chaos in a system of three coupled phase oscillators. Mean-field approaches to the Kuramoto model are reviewed by Strogatz (2000) and Acebron et al. (2005). Daido (1996) extended the theory to the general coupling function $H(\chi)$. van Hemmen and Wreszinski (1993) were the first to find the Lyapunov function for the Kuramoto model, which was generalized (independently) by Hoppensteadt and Izhikevich (1997) to the arbitrary coupling function $H(\chi)$.

Ermentrout (1986), Aronson et al. (1990), and Hoppensteadt and Izhikevich (1996, 1997) studied weakly coupled Andronov-Hopf oscillators, and discussed the phenomena of self-ignition (coupling-induced oscillations) and oscillator death (coupling-induced cessation of oscillation). Collins and Stewart (1993, 1994) and Golubitsky and Stewart (2002) applied group theory to the study of synchronization of coupled oscillators in networks with symmetries.

In this chapter we have considered either strong *pulsed* coupling or *weak* continuous coupling. These limitations are severe, but they allow us to derive model-independent results. Studying synchronization in networks of strongly coupled neurons is an active area of research, though, most such studies fall into two categories: (1) simulations and (2) integrate-and-fire networks. In both cases, the results are model-dependent. If the reader wants to pursue this line of research, he or she will definitely need to read Mirollo and Strogatz (1990), van Vreeswijk et al. (1994), Chow and Kopell (2000), Rubin and Terman (2000, 2002), Bressloff and Coombes (2000), van Vreeswijk (2000), van Vreeswijk and Hansel (2001), Pfeuty et al. (2003), and Hansel and Mato (2003).

Exercises

1. Find the isochrons of the Andronov-Hopf oscillator

$$\dot{z} = (1 + \mathrm{i})z - z|z|^2, \qquad z \in \mathbb{C},$$

   in Fig.10.3.

2. Prove that the isochrons of the Andronov-Hopf oscillator in the form

$$\dot{z} = (1 + \mathrm{i})z + (-1 + d\mathrm{i})z|z|^2, \qquad z \in \mathbb{C},$$

   are the curves

$$z(s) = s^{(-1+d\mathrm{i})}\, e^{\chi \mathrm{i}}\,, \qquad s > 0\,,$$

   where χ is the phase of the isochron (see Fig.10.45).

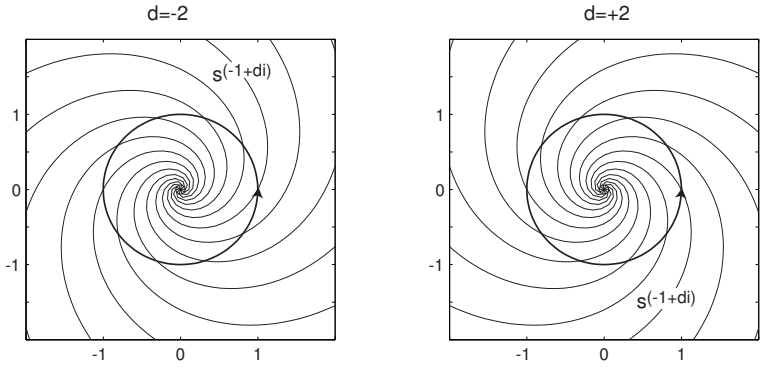

Figure 10.45: Isochrons of the Andronov-Hopf oscillator; see exercise 2.

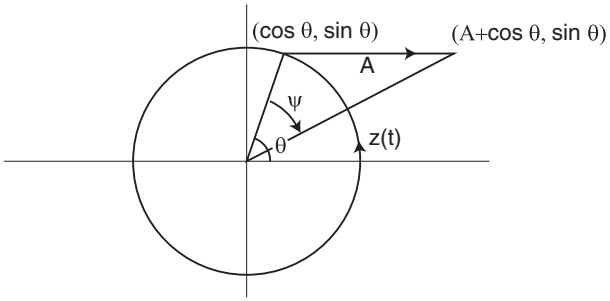

Figure 10.46: Pulsed stimulation of the Andronov-Hopf oscillator in Fig.10.3; see exercise 4.

3. [MATLAB] To determine isochrons of an oscillator $\dot{x} = F(x)$, one can start with many initial points near the limit cycle and integrate the system backwards, that is, $\dot{x} = -F(x)$. The images of the points at any time t lie on the same isochron. Write a MATLAB program that implements this algorithm.

4. Prove that the phase response curve of the Andronov-Hopf oscillator in Fig.10.3 is

$$\mathrm{PRC}\,(\vartheta, A) = \begin{cases} -\psi & \text{when } 0 \le \vartheta \le \pi, \\ +\psi & \text{when } \pi \le \vartheta \le 2\pi, \end{cases} \tag{10.29}$$

where

$$\psi = \arccos \frac{1 + A\cos\vartheta}{\sqrt{1 + 2A\cos\vartheta + A^2}}$$

and A is the magnitude of the horizontal displacement of $z(t)$; see Fig.10.46.

5. [MATLAB] Write a program that stimulates an oscillator at different phases and determines its phase response curve (PRC).

6. Show that $Z(\vartheta) = \operatorname{grad}\vartheta$, so that Winfree's phase model (10.6) is equivalent to Kuramoto's phase model (10.8).

7. Show that $Z(\vartheta) = Q(\vartheta)$, so that Winfree's phase model (10.6) is equivalent to Malkin's phase model (10.9).

8. Show that the PRC of the leaky integrate-and-fire neuron (section 8.1.1)

$$\dot{v} = b - v \ , \qquad \text{if } v \geq 1 \text{ (threshold), then } v \leftarrow 0 \text{ (reset)}$$

with $b > 1$ has the form

$$\mathrm{PRC}\,(\vartheta) = \min\left\{\ln(b/(b\exp(-\vartheta) - A)), T\right\} - \vartheta \ ,$$

where $T = \ln(b/(b-1))$ is the period of free oscillations and A is the amplitude of the pulse.

9. Prove that the quadratic integrate-and-fire neuron

$$\dot{v} = 1 + v^2 \ , \qquad \text{if } v = +\infty \text{ (peak of spike), then } v \leftarrow -\infty \text{ (reset)}$$

has $\mathrm{PTC}\,(\vartheta) = \pi/2 + \ \mathrm{atan}\,(A - \cot\vartheta)$.

10. Find the PRC of the quadratic integrate-and-fire neuron (section 8.1.3)

$$\dot{v} = b + v^2 \ , \qquad \text{if } v \geq 1 \text{ (peak of spike), then } v \leftarrow v_{\mathrm{reset}} \text{ (reset)}$$

with $b > 0$.

11. Consider two mutually pulsed coupled oscillators with periods $T_1 \approx T_2$ and type 1 phase transition curves PTC_1 and PTC_2, respectively. Show that the locking behavior of the system can be described by the Poincare phase map

$$\chi_{n+1} = T_1 - \ \mathrm{PTC}_1(T_2 - \ \mathrm{PTC}_2(\chi_n)) \ ,$$

where χ_n is the phase difference between the oscillators, that is, the phase of oscillator 2 when oscillator 1 fires a spike.

12. [MATLAB] Write a program that solves the adjoint equation (10.10) numerically. (Hint: Integrate the equation backward to achieve stability.)

13. [MATLAB] Write a program that finds the infinitesimal PRC using the relationship

$$\dot{\vartheta} = 1 + \mathrm{PRC}\,(\vartheta)\ \varepsilon p(t) \ ,$$

the moments of firings of a neuron (zero crossings of $\vartheta(t)$), and the injected current $\varepsilon p(t)$; see section 10.2.4 and Fig.10.24.

14. Use the approaches of Winfree, Kuramoto, and Malkin to transform the integrate-and-fire neuron $\dot{v} = b - v + \varepsilon p(t)$ in exercise 8 into its phase model

$$\dot{\vartheta} = 1 + \varepsilon \left(e^{\vartheta}/b\right) p(t) \ ,$$

with $T = \ln(b/(b-1))$.

15. Use the approaches of Winfree, Kuramoto, and Malkin to transform the quadratic integrate-and-fire neuron $\dot{v} = 1 + v^2 + \varepsilon p(t)$ in exercise 9 into its phase model

$$\dot{\vartheta} = 1 + \varepsilon \left(\sin^2 \vartheta\right) p(t) \ ,$$

with $T = \pi$.

16. Use the approaches of Winfree, Kuramoto, and Malkin to transform the Andronov-Hopf oscillator $\dot{z} = (1 + \mathrm{i})z - z|z|^2 + \varepsilon p(t)$ with real $p(t)$ into its phase model

$$\dot{\vartheta} = 1 + \varepsilon \left(-\sin \vartheta\right) p(t) \ ,$$

with $T = 2\pi$.

17. (PRC for Andronov-Hopf) Consider a weakly perturbed system near supercritical Andronov-Hopf bifurcation (see section 6.1.3)

$$\dot{z} = (b + \mathrm{i})z + (-1 + d\mathrm{i})z|z|^2 \ + \epsilon p(t) \ , \qquad z \in \mathbb{C} \ .$$

with $b > 0$. Let $\varepsilon = b\sqrt{b}/\epsilon$ be small. Prove that the corresponding phase model is

$$\dot{\theta} = 1 + d + \varepsilon \, \mathrm{Im} \left\{(1 + d\mathrm{i}) p(t) e^{-\mathrm{i}\theta}\right\} \ .$$

When the forcing $p(t)$ is one-dimensional (i.e., $p(t) = cq(t)$ with $c \in \mathbb{C}$ and scalar function $q(t)$), the phase model has the sinusoidal form

$$\dot{\theta} = 1 + d + \varepsilon s \sin(\theta - \psi) q(t) \ ,$$

with the strength s and the phase shift ψ depending only on d and c.

18. (Delayed coupling) Show that weakly coupled oscillators

$$\dot{x}_i = f(x_i) + \varepsilon \sum_{j=1}^{n} g_{ij}(x_i(t), x_j(t - d_{ij}))$$

with explicit axonal conduction delays $d_{ij} \geq 0$ have the phase model

$$\varphi_i' = \omega_i + \sum_{j \neq i}^{n} H_{ij}(\varphi_j - d_{ij} - \varphi_i)$$

where $' = d/d\tau$, $\tau = \varepsilon t$ is the slow time, and $H(\chi)$ is defined by (10.16). Thus, explicit delays result in explicit phase shifts.

19. Determine the existence and stability of synchronized states in the system

$$\begin{aligned} \dot{\varphi}_1 &= \omega_1 + c_1 \sin(\varphi_2 - \varphi_1) \\ \dot{\varphi}_2 &= \omega_2 + c_2 \sin(\varphi_1 - \varphi_2) \end{aligned}$$

as a function of the parameters $\omega = \omega_2 - \omega_1$ and $c = c_2 - c_1$.

20. Consider the Kuramoto model

$$\varphi_i = \omega + \sum_{j=1}^{n} c_{ij} \sin(\varphi_j + \psi_{ij} - \varphi_i) \ ,$$

where c_{ij} and ψ_{ij} are parameters. What can you say about its synchronization properties?

21. Derive the self-consistency equation (10.22) for the Kuramoto model (10.20).

22. Consider the phase deviation model

$$\begin{aligned} \varphi_1' &= \omega + c_1 H(\varphi_2 - \varphi_1) \\ \varphi_2' &= \omega + c_2 H(\varphi_1 - \varphi_2) \end{aligned}$$

with an even function $H(-\chi) = H(\chi)$. Prove that the in-phase synchronized state, $\varphi_1 = \varphi_2$, if it exists, cannot be exponentially stable. What can you say about the anti-phase state $\varphi_1 = \varphi_2 + T/2$?

23. Prove that the in-phase synchronized state in a network of three or more pulse coupled quadratic integrate-and-fire neurons is unstable.

24. Prove (10.25).

25. (Brown et al. 2004) Show that the PRC for an oscillator near saddle homoclinic orbit bifurcation scales as $\mathrm{PRC}\,(\vartheta) \sim e^{\lambda(T-\vartheta)}$, where λ is the positive eigenvalue of the saddle and T is the period of oscillation.

26. Consider the quadratic integrate-and-fire neuron $\dot{x} = \pm 1 + x^2$ with the resetting " if $x = +\infty$, then $x \leftarrow x_{\mathrm{reset}}$". Prove that

regime	SNIC	homoclinic
model	$x' = +1 + x^2$	$x' = -1 + x^2, (x_{\mathrm{reset}} > 1)$
	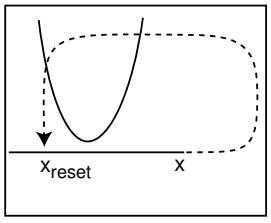	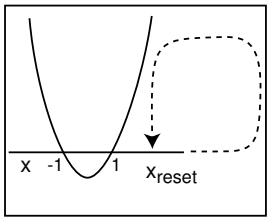
period T	$\pi/2 - \operatorname{atan} x_{\mathrm{reset}}$	$\operatorname{acoth} x_{\mathrm{reset}}$
solution $x(t)$	$-\cot(t-T)$	$-\coth(t-T)$
PRC $Q(\vartheta)$	$\sin^2(\vartheta - T)$	$\sinh^2(\vartheta - T)$
	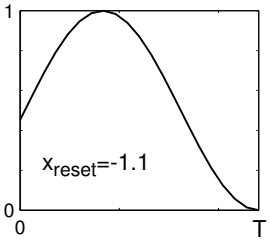	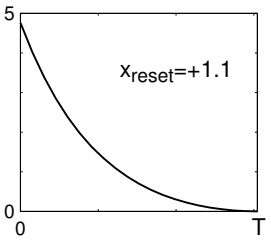

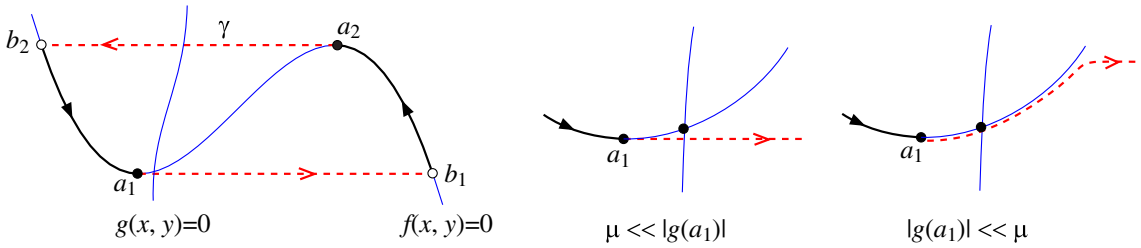

Figure 10.47: *Left:* Relaxation oscillator in the limit $\mu = 0$ near the onset of oscillation. *Middle and right*: A magnification of a neighborhood of the jump point a_1 for various $g(a_1)$ and μ. Canard solutions can appear when $g(a_1) \ll \mu$.

where coth, acoth, and sinh are hyperbolic cotangent, hyperbolic inverse cotangent and hyperbolic sine, respectively.

27. [**M.S.**] Derive the PRC for an oscillator near saddle homoclinic orbit bifurcation that is valid during the spike downstroke. Take advantage of the observation in Fig.10.39 that the homoclinic orbit consists of two qualitatively different parts.

28. [**M.S.**] Derive the PRC for a generic oscillator near fold limit cycle bifurcation (beware of the problems of defining the phase near such a bifurcation).

29. [**M.S.**] Simplify the connection function H for coupled relaxation oscillators (Izhikevich 2000b) when the slow nullcline approaches the left knee, as in Fig.10.47. Explore the range of parameters ε, μ, and $|g(a_1)|$ where the analysis is valid.

30. [**Ph.D.**] Use ideas outlined in section 10.4.5 to develop the theory of reduction of weakly coupled bursters to phase models. Do not assume that bursting trajectory is periodic.

Solutions to Chapter 10

1. In polar coordinates, $z = re^{\mathrm{i}\vartheta}$, the system has the form

$$\dot{\vartheta} = 1 \,, \quad \dot{r} = r - r^3.$$

Since the phase of oscillation does not depend on the amplitude, the isochrons have the radial structure depicted in Fig.10.3.

2. In polar coordinates, the oscillator has the form

$$\dot{\vartheta} = 1 + dr^2 \,, \quad \dot{r} = r - r^3.$$

The second equation has an explicit solution $r(t)$, such that

$$r(t)^2 = \frac{1}{1 - (1 - 1/r(0)^2)e^{-2t}} \,.$$

The phase difference between $\dot{\vartheta_{\rm lc}} = 1 + d(1)^2$ and $\dot{\vartheta} = 1 + dr(t)^2$ grows as $\dot{\chi} = d(r(t)^2 - 1)$, and its asymptotic value is

$$\chi(\infty) = \int_0^\infty d(r(t)^2 - 1) = d \log r(0) \ .$$

Thus, on the χ-isochron, we have $\vartheta + d \log r = \chi$.

3. An example is the file `isochrons.m`

```
function isochrons(F,phases,x0)
% plot isochrons of a planar dynamical system x'=F(t,x)
% at points given by the vector 'phases'.
% 'x0' is a point on the limit cycle (2x1-vector)
T= phases(end); % is the period of the cycle
tau = T/600;    % time step of integration
m=200;          % spatial grid
k=5;            % the number of skipped cycles

[t,lc] = ode23s(F,0:tau:T,x0);      % forward integration
dx=(max(lc)-min(lc))'/m;            % spatial resolution
center = (max(lc)+min(lc))'/2;      % center of the limit cycle
iso=[x0-m^0.5*dx, x0+m^0.5*dx];     % isochron's initial segment

for t=0:-tau:-(k+1)*T               % backward integration
    for i=1:size(iso,2)
        iso(:,i)=iso(:,i)-tau*feval(F,t,iso(:,i)); % move one step
    end;
    i=1;
    while i<=size(iso,2)            % remove infinite solutions
        if any(abs(iso(:,i)-center)>1.5*m*dx)    % check boundaries
            iso = [iso(:,1:i-1), iso(:,i+1:end)]; % remove
        else
            i=i+1;
        end;
    end;
    i=1;
    while i<=size(iso,2)-1
        d=sqrt(sum(((iso(:,i)-iso(:,i+1))./dx).^2)); % normalized distance
        if d > 2                    % add a point in the middle
            iso = [iso(:,1:i), (iso(:,i)+iso(:,i+1))/2 ,iso(:,i+1:end)];
        end;
        if d < 0.5                  % remove the point
            iso = [iso(:,1:i), iso(:,i+2:end)];
        else
            i=i+1;
        end;
    end;
    if (mod(-t,T)<=tau/2) & (-t<k*T+tau)        % refresh the screen
        cla;plot(lc(:,1),lc(:,2),'r'); hold on; % plot the limit cycle
    end;
    if min(abs(mod(-t,T)-phases))<tau/2   % plot the isochrons
        plot(iso(1,:),iso(2,:),'k-'); drawnow;
    end;
end;
```

```
hold off;
```

The call of the function is `isochrons('F',0:0.1:2*pi,[1;0]);` with

```
function dx = F(t,x);
z=x(1)+1i*x(2);
dz=(1+1i)*z-z*z*conj(z);
dx=[real(dz); imag(dz)];
```

4. (Hoppensteadt and Keener 1982) From calculus, $B \cdot C = |B|\,|C| \cos(\psi)$. Since $|B| = 1$ and $C = (A + \cos\vartheta, \sin\vartheta)$ – see Fig.10.46 – we have $B \cdot C = A\cos\vartheta + \cos^2\vartheta + \sin^2\vartheta$. Hence, $\cos\psi = (1 + A\cos\vartheta)/\sqrt{1 + 2A\cos\vartheta + A^2}$. When ϑ is in the upper (lower) half-plane, the phase is delayed (advanced).

5. An example is the file `prc.m`

```
function PRC=prc(F,phases,x0,A)
% plot phase-resetting curve (PRC) of system x'=F(t,x) + A delta(t)
% at points given by the vector 'phases'.
% 'x0' is a point on the limit cycle with zero phase
% A is the strength of stimulation (row-vector)
% use peaks of spikes to find the phase differences
T= phases(end); % is the period of the cycle
tau = T/6000;    % time step of integration
k=3;            % the number of cycles needed to determine the new phase
PRC=[];
[tc,lc] = ode23s(F,0:tau:k*T,x0); % find limit cycle
peak=1+find(lc(2:end-1,1)>lc(1:end-2,1)&lc(2:end-1,1)>=lc(3:end,1));
peak0 = tc(peak(end)); % the last peak is used for reference
for i=1:length(phases)
    [m,j]=min(abs(phases(i)-tc));
    [t,x] = ode23s(F,phases(i):tau:k*T,lc(j,:)+A); % stimulate
    peaks=1+find(x(2:end-1,1)>x(1:end-2,1)&x(2:end-1,1)>=x(3:end,1));
    PRC=[PRC, mod(T/2+peak0-t(peaks(end)),T)-T/2];
    subplot(2,1,2);drawnow;
    plot(phases(1:length(PRC)),PRC);
    xlabel('phase of stimulation');ylabel('induced phase difference');
    subplot(2,1,1);
    plot(tc,lc(:,1),'r',t,x(:,1),t(peaks(end)),x(peaks(end),1),'ro');
    xlabel('time');ylabel('membrane potential');
end;
```

An example of a call of the function is `PRC=prc('F',0:0.1:2*pi,[-1 0],[0.1 0]);` with

```
function dx = F(t,x);
z=x(1)+1i*x(2);
dz=(1+1i)*z-z*z*conj(z);
dx=[real(dz); imag(dz)];
```

6.

$$\begin{aligned}\operatorname{grad}\vartheta(x) &= \left(\frac{\vartheta(x+h_1)-\vartheta(x)}{h_1}, \ldots, \frac{\vartheta(x+h_m)-\vartheta(x)}{h_m}\right) \\ &= \left(\frac{\mathrm{PRC}_1(\vartheta(x),h_1)}{h_1}, \ldots, \frac{\mathrm{PRC}_m(\vartheta(x),h_m)}{h_m}\right)\end{aligned}$$

$$\begin{aligned} & \text{(in the limit } h \to 0) \\ = & \left(\frac{Z_1(\vartheta(x))h_1}{h_1}, \ldots, \frac{Z_m(\vartheta(x))h_m}{h_m} \right) \\ = & (Z_1(\vartheta(x)), \ldots, Z_m(\vartheta(x))) = Z(\vartheta(x)) \; . \end{aligned}$$

7. (Brown et al. 2004, appendix A) Let x be a point on the limit cycle and z be an arbitrary nearby point. Let $x(t)$ and $z(t)$ be the trajectories starting from the two points, and $y(t) = z(t) - x(t)$ be the difference. All equations below are valid up to $\mathcal{O}(y^2)$. The phase shift $\Delta\vartheta = \vartheta(z(t)) - \vartheta(x(t)) = \operatorname{grad}\vartheta(x(t)) \cdot y(t)$ does not depend on time. Differentiating with respect to time and taking $\operatorname{grad}\vartheta(x(t)) = Z(\vartheta(t))$ (see previous exercise), results in

$$\begin{aligned} 0 &= (d/dt)\left(Z(\vartheta(t)) \cdot y(t)\right) = Z'(\vartheta(t)) \cdot y(t) + Z(\vartheta(t)) \cdot Df(x(t))y(t) \\ &= Z'(\vartheta(t)) \cdot y(t) + Df(x(t))^\top Z(\vartheta(t)) \cdot y(t) \\ &= \left(Z'(\vartheta(t)) + Df(x(t))^\top Z(\vartheta(t)) \right) \cdot y(t) \; . \end{aligned}$$

Since y is arbitrary, Z satisfies $Z'(\vartheta) + Df(x(\vartheta))^\top Z(\vartheta) = 0$, that is, the adjoint equation (10.10). The normalization follows from (10.7).

8. The solution to $\dot{v} = b - v$ with $v(0) = 0$ is $v(t) = b(1 - e^{-t})$ with the period $T = \ln(b/(b-1))$ determined from the threshold crossing $v(T) = 1$. From $v = b(1 - e^{-\vartheta})$ we find $\vartheta = \ln(b/(b-v))$, hence

$$\operatorname{PRC}(\vartheta) = \vartheta_{\text{new}} - \vartheta = \min\left\{\ln(b/(b\exp(-\vartheta) - A), T\right\} - \vartheta \; .$$

9. The system $\dot{v} = 1 + v^2$ with $v(0) = -\infty$ has the solution (the reader should check this by differentiating) $v(t) = \tan(t - \pi/2)$ with the period $T = \pi$. Since $t = \pi/2 + \operatorname{atan} v$, we find

$$\operatorname{PTC}(\vartheta) = \pi/2 + \operatorname{atan}\left[A + \tan(\vartheta - \pi/2)\right]$$

and

$$\operatorname{PRC}(\vartheta) = \operatorname{PTC}(\vartheta) - \vartheta = \operatorname{atan}\left[A + \tan(\vartheta - \pi/2)\right] - (\vartheta - \pi/2) \; .$$

10. The system $\dot{v} = b + v^2$ with $b > 0$ and the initial condition $v(0) = v_{\text{reset}}$ has the solution (the reader should check this by differentiating)

$$v(t) = \sqrt{b}\tan(\sqrt{b}(t + t_0))$$

where

$$t_0 = \frac{1}{\sqrt{b}} \operatorname{atan} \frac{v_{\text{reset}}}{\sqrt{b}} \; .$$

Equivalently,

$$t = \frac{1}{\sqrt{b}} \operatorname{atan} \frac{v}{\sqrt{b}} - t_0 \; .$$

From the condition $v = 1$ (peak of the spike), we find

$$T = \frac{1}{\sqrt{b}} \operatorname{atan} \frac{1}{\sqrt{b}} - t_0 = \frac{1}{\sqrt{b}} \left(\operatorname{atan} \frac{1}{\sqrt{b}} - \operatorname{atan} \frac{v_{\text{reset}}}{\sqrt{b}} \right) \; ,$$

Hence

$$\operatorname{PRC}(\vartheta) = \vartheta_{\text{new}} - \vartheta = \min\left\{ \frac{1}{\sqrt{b}} \operatorname{atan}\left[\frac{A}{\sqrt{b}} + \tan(\sqrt{b}(\vartheta + t_0)) \right] - t_0, T \right\} - \vartheta \; .$$

11. Let ϑ denote the phase of oscillator 1. Let χ_n denote the phase of oscillator 2 just before oscillator 1 fires a spike (i.e., when $\vartheta = 0$). This spike resets χ_n to $\mathrm{PTC}_2(\chi_n)$. Oscillator 2 fires a spike when $\vartheta = T_2 - \mathrm{PTC}_2(\chi_n)$, and it resets ϑ to $\mathrm{PTC}_1(T_2 - \mathrm{PTC}_2(\chi_n))$. Finally, oscillator 1 fires its spike when oscillator 2 has the phase $\chi_{n+1} = T_1 - \mathrm{PTC}_1(T_2 - \mathrm{PTC}_2(\chi_n))$.

12. [MATLAB] An example is the file `adjoint.m`

```
function Q=adjoint(F,t,x0)
% finds solution to the Malkin's adjoint equation Q' = -DF^t Q
% at time-points t with t(end) being the period
% 'x0' is a point on the limit cycle with zero phase
tran=3;         % the number of skipped cycles
dx = 0.000001; dy = 0.000001;   % for evaluation of Jacobian

Q(1,:)=feval(F,0,x0)';          % initial point;
[t,x] = ode23s(F,t,x0);         % find limit cycle

for k=1:tran
  Q(length(t),:)=Q(1,:);        % initial point;
  for i=length(t):-1:2          % backward integration
    L = [(feval(F,t(i),x(i,:)+[dx 0])-feval(F,t(i),x(i,:)))/dx,...
         (feval(F,t(i),x(i,:)+[0 dy])-feval(F,t(i),x(i,:)))/dy];
    Q(i-1,:) = Q(i,:) + (t(i)-t(i-1))*(Q(i,:)*L);
  end;
end;
Q = Q/(Q(1,:)*feval(F,0,x0));   % normalization
```

An example of a call of the function is `Q=adjoint('F',0:0.01:2*pi,[1 0]);` with

```
function dx = F(t,x);
z=x(1)+1i*x(2);
dz=(1+1i)*z-z*z*conj(z);
dx=[real(dz); imag(dz)];
```

13. [MATLAB] We assume that $\mathrm{PRC}(\vartheta)$ is given by its truncated Fourier series with unknown Fourier coefficients. Then, we find the coefficients that minimize the difference between predicted and actual interspike intervals. The MATLAB file `findprc.m` takes the row vector of spike moments, not counting the spike at time zero, and the input function $p(t)$, determines the sampling frequency and the averaged period of oscillation; and then calls the file `prcerror.m` to find PRC.

```
function PRC=findprc(sp,pp)
global spikes p tau n
% finds PRC of an oscillator theta'= 1 + PRC(theta)pp(t)
% using the row-vector of spikes 'sp' (when theta(t)=0)
spikes = [0 sp];
p=pp;
tau = spikes(end)/length(p) % time step (sampling period)
n=8;    % The number of Fourier terms approximating PRC
coeff=zeros(1,2*n+1); % initial approximation
coeff(2*n+2) = spikes(end)/length(spikes); % initial period

coeff=fminsearch('prcerror',coeff);
a = coeff(1:n)     % Fourier coefficients for sin
```

```
b = coeff(n+1:2*n) % Fourier coefficients for cos
b0= coeff(2*n+1)   % dc term
T = coeff(2*n+2)   % period of oscillation
PRC=b0+sum((ones(floor(T/tau),1)*a).*sin((tau:tau:T)'*(1:n)*2*pi/T),2)+...
       sum((ones(floor(T/tau),1)*b).*cos((tau:tau:T)'*(1:n)*2*pi/T),2);
```

The following program must be in the file `prcerror.m`.

```
function err=prcerror(coeff)
global spikes p tau n
a = coeff(1:n);     % Fourier coefficients for sin
b = coeff(n+1:2*n); % Fourier coefficients for cos
b0= coeff(2*n+1);   % dc term
T = coeff(2*n+2);   % period of oscillation
err=0;
i=1;
clf;
for s=2:length(spikes)
    theta=0;
    while i*tau<=spikes(s)
        PRC=b0+sum(a.*sin((1:n)*2*pi*theta/T))+...
               sum(b.*cos((1:n)*2*pi*theta/T));
        theta = theta + tau*(1+PRC*p(i));
        i=i+1;
    end;
    err = err + (theta-T)^2;
    subplot(2,1,1);
    plot(spikes(s),T,'r.',spikes(s),theta,'b.');hold on;
end;
axis([0 spikes(end) 0.75*T 1.25*T])
subplot(2,1,2);
PRC=b0+sum((ones(floor(T/tau),1)*a).*sin((tau:tau:T)'*(1:n)*2*pi/T),2)+...
       sum((ones(floor(T/tau),1)*b).*cos((tau:tau:T)'*(1:n)*2*pi/T),2);
plot(PRC);
err = (err/(length(spikes)-1))^0.5;  % normalization
text(0,mean(PRC),['err=' num2str(err)]);
drawnow;
```

14. *Winfree approach:* Using results of exercise 8,

$$\frac{\partial}{\partial A} \ln \frac{b}{be^{-\vartheta} - A} = \frac{1}{be^{-\vartheta} - A}$$

and setting $A = 0$, we obtain $Z(\vartheta) = e^{\vartheta}/b$.

Kuramoto approach: The solution is $v(\vartheta) = b(1 - e^{-\vartheta})$ with $T = \ln(b/(b-1))$ and $f(v(\vartheta)) = be^{-\vartheta}$. From the condition (10.7), $\text{grad}\,(\vartheta) = 1/f(v(\vartheta)) = e^{\vartheta}/b$.

Malkin approach: $Df = -1$; hence $\dot{Q} = 1 \cdot Q$ has the solution $Q(t) = Ce^t$. The free constant $C = 1/b$ is found from the normalization condition $Q(0) \cdot (b - 0) = 1$.

15. *Winfree approach:* Using results of exercise 10 and the relation PRC=PTC$-\vartheta$, we obtain,

$$\frac{\partial}{\partial A} \left(\pi/2 + \text{ atan}\,(A - \cot\vartheta) - \vartheta\right) = \frac{1}{1 + (A - \cot\vartheta)^2}$$

and, setting $A = 0$, $Z(\vartheta) = \sin^2\vartheta$.

Kuramoto approach: The solution is $v(\vartheta) = -\cot\vartheta$ with $T = \pi$ and $f(v(\vartheta)) = 1/\sin^2\vartheta$. From the normalization condition (10.7), $\operatorname{grad}(\vartheta) = 1/f(v(\vartheta)) = \sin^2\vartheta$.

Malkin approach: $Df = 2v$, hence $\dot{Q} = 2\cot(t)\cdot Q$ has the solution $Q(t) = C\sin^2 t$. The free constant $C = 1$ is found from the normalization condition $Q(\pi/2)\cdot(1+0^2) = 1$.

16. *Winfree approach:* Using results of exercise 4,

$$Z(\vartheta) = \frac{\partial}{\partial A}\ \operatorname{acos}\frac{1+A\cos\vartheta}{\sqrt{1+2A\cos\vartheta+A^2}} = -\sin\vartheta$$

at $A = 0$.

Kuramoto approach: Since $\operatorname{grad}\vartheta(x)$ is orthogonal to the contour line of the function $\vartheta(x)$ at x (i.e., the isochron of x) and the results of exercise 1 that isochrons are radial, we obtain $\operatorname{grad}(\vartheta) = (-\sin\vartheta, \cos\vartheta)$, using purely geometrical considerations. Since $p(t)$ is real, we need to keep only the first component.

Malkin approach: Let us work in the complex domain. On the circle $z(t) = e^{\mathrm{i}t}$ we obtain $Df = \mathrm{i}$. Since $Df^\top$ is equivalent to complex-conjugation in the complex domain, we obtain $\dot{Q} = \mathrm{i}\cdot Q$, which has the solution $Q(t) = Ce^{\mathrm{i}t}$. The free constant $C = \mathrm{i}$ is found from the normalization condition $Q(0)^*\mathrm{i} = 1$, where * means complex-conjugate.

Alternatively, on the circle $z(t) = e^{\mathrm{i}t}$, we have $f(z(t)) = f(e^{\mathrm{i}t}) = \mathrm{i}e^{\mathrm{i}t}$. From the normalization condition $Q(t)^* f(z(t)) = 1$ we find $Q(t) = \mathrm{i}e^{\mathrm{i}t} = -\sin\vartheta + \mathrm{i}\cos\vartheta$.

17. Rescaling the state variable $z = \sqrt{b}u$ and the time, $\tau = \epsilon t$, we obtain the reduced system

$$u' = (1+\mathrm{i})u + (-1+d\mathrm{i})u|u|^2\ + \varepsilon p(t)\ .$$

We can apply the theory only when ε is small. That is, the theory is guaranteed to work in a very weak limit $\epsilon \ll b\sqrt{b} \ll 1$. As is often the case, numerical simulations suggest that the theory works well outside the guaranteed interval. Substituting $u = re^{\mathrm{i}\theta}$ into this equation,

$$r'e^{\mathrm{i}\theta} + re^{\mathrm{i}\theta}\mathrm{i}\theta' = (1+\mathrm{i})re^{\mathrm{i}\theta} + (-1+d\mathrm{i})r^3e^{\mathrm{i}\theta} + \varepsilon p(t)\ ,$$

dividing by $e^{\mathrm{i}\theta}$, and separating real and imaginary terms, we represent the oscillator in polar coordinates

$$\begin{aligned} r' &= r - r^3 \quad + \varepsilon\operatorname{Re} p(t)e^{-\mathrm{i}\theta} \\ \theta' &= 1 + dr^2 \ + \varepsilon\operatorname{Im} r^{-1}p(t)e^{-\mathrm{i}\theta}\ . \end{aligned}$$

When $\varepsilon = 0$, this system has a limit cycle attractor $r(t) = 1$ and $\theta(t) = (1+d)t$, provided that $d \neq -1$. On the attractor, the solution to Malkin's adjoint equation (10.10),

$$Q' = -\begin{pmatrix} -2 & 0 \\ 2d & 0 \end{pmatrix}^\top Q \quad \text{with} \quad Q(t)\cdot\begin{pmatrix} 0 \\ 1+d \end{pmatrix} = 1\ ,$$

is $Q(t) = (d,\ 1)/(1+d)$. Indeed, the normalization condition results in $Q_2(t) = 1/(1+d)$. Hence, unique periodic solution of the first equation, $Q_1' = 2Q_1 - 2d/(1+d)$, is $Q_1(t) = d/(1+d)$. One can also use Kuramoto's approach and the results of exercise 2. The corresponding phase model,

$$\vartheta' = 1 + \varepsilon\{d\operatorname{Re} p(t)e^{-\mathrm{i}(1+d)\vartheta} + \operatorname{Im} p(t)e^{-\mathrm{i}(1+d)\vartheta}\}/(d+1)\ ,$$

can be simplified via $\theta = (1+d)\vartheta$ (notice the font difference) to get the result.

18. (Delayed coupling) Let $\vartheta(t) = t + \varphi(\tau)$, where $\tau = \varepsilon t$ is the slow time. Since $\vartheta(t-d) = t - d + \varphi(\tau - \varepsilon d) = t - d + \varphi(\tau) + \mathcal{O}(\varepsilon)$, we have $x_j(\vartheta_i(t-d_{ij})) = x_j(t - d_{ij} + \varphi(\tau))$, so that we can proceed as in section 10.2.5, except that there is an extra term, $-d_{ij}$, in (10.16). See also Izhikevich (1998).

19. Let $\chi = \varphi_2 - \varphi_1$; then we have
$$\dot\chi = \omega - c\sin\chi\ .$$
If $|\omega/c| \le 1$, then there are two synchronized states, $\chi = \arcsin(\omega/c)$ and $\chi = \pi - \arcsin(\omega/c)$, one stable and the other unstable.

20. From the theorem of Hoppensteadt and Izhikevich (1997), presented in section 10.3.3, it follows that Kuramoto's model is a gradient system when $c_{ij} = c_{ji}$ and $\psi_{ij} = -\psi_{ji}$. From Ermentrout's theorem presented in the same section, it follows that the synchronized state $\varphi_i = \varphi_j$ is stable if, for example, all $\psi_{ij} = 0$ and $c_{ij} > 0$.

21. Since the probability density function $g(\omega)$ is symmetric, the averaged frequency deviation of the network is zero, and, rotating the coordinate system, we can make the cluster phase $\psi = 0$. The network is split into two populations: One oscillating with the cluster ($|\omega| < Kr$), thereby forming the cluster, and one drifting in and out of the cluster. The latter does not contribute to the Kuramoto synchronization index, because contributions from different oscillators cancel each other on average. In the limit $n \to \infty$, the sum (10.21) becomes the integral
$$r = \int e^{\mathrm{i}\varphi(\omega)} g(\omega)\, d\omega \approx \int_{|\omega|<Kr} e^{\mathrm{i}\varphi(\omega)} g(\omega)\, d\omega\ .$$
Next, since there are as many oscillators with positive φ as with negative, the imaginary parts of $e^{\mathrm{i}\varphi(\omega)}$ cancel each other, so that
$$r = \int_{|\omega|<Kr} \cos\varphi(\omega) g(\omega)\, d\omega\ .$$
Using the condition for locking with the cluster, $\omega = Kr\sin\varphi$, we change the variables in the integral and obtain (10.22).

22. Let $\chi = \varphi_2 - \varphi_1$; then $\chi' = (c_2 - c_1)H(\chi)$. The in-phase state $\chi = 0$ exists when either $c_1 = c_2$ or $H(0) = 0$. Since $H(\chi)$ is even, $H'(0) = 0$, and hence it is neutrally stable in either case. The anti-phase state $\chi = T/2$ exists when $H(T/2) = 0$, and it can be exponentially stable or unstable, depending on the sign of $H'(T/2)$.

23. See Izhikevich (1999), Sect IVB.

24. The exponential stability requirement is $G'(0) = -2H'(0) < 0$. Since $x'(t) = f(x(t))$, we have
$$TH'(0) = \int_0^T \frac{g'(x(t))f(x(t))}{f(x(t))}\, dt = \int_0^T g'(x(t))\, dt = \int_{\mathbb{S}^1} \frac{g'(x)}{f(x)}\, dx > 0$$
Integrating the latter equation by parts, or differentiating
$$H(\chi) = \frac{1}{T}\int_0^T \frac{g(x(t))}{f(x(t-\chi))}\, dt \qquad \text{at } \chi = 0, \text{ we obtain} \qquad \int_{\mathbb{S}^1} \frac{f'(x)}{f^2(x)}\, g(x)\, dx > 0\ .$$

25. (Brown et al. 2004) The solution of $x' = \lambda x$ with $x(0) = x_0$ is $x(t) = x_0 e^{\lambda t}$. The period $T = \log(\Delta/x_0)/\lambda$ is found from the condition $x(T) = \Delta$. Hence, $Q(\vartheta) = 1/(\lambda x(\vartheta)) = 1/(\lambda x_0 e^{\lambda\vartheta}) = e^{\lambda(T-\vartheta)}/(\Delta\lambda)$.

26. Let us first consider the SNIC case $\dot{x} = 1 + x^2$. The solution starting with $x(0) = x_{\text{reset}}$ has the form (the reader should check by differentiating) $x(t) = \tan(t + t_0)$, where $t_0 = \operatorname{atan} x_{\text{reset}}$. The period should be found from the condition $\tan(T + t_0) = +\infty$, and it is $T = \pi/2 - t_0$. Hence, $x(t) = \tan(t + \pi/2 - T) = -\cot(t - T)$. Now, $Q(\vartheta) = 1/(1 + x(\vartheta)^2) = 1/(1 + \cot^2(\vartheta - T)) = \sin^2(\vartheta - T)$.

    The homoclinic case $\dot{x} = -1 + x^2$ is quite similar. The solution starting with $x(0) = x_{\text{reset}} > 1$ has the form (the reader should check by differentiating) $x(t) = -\coth(t + t_0)$, where $t_0 = \operatorname{acoth}(-x_{\text{reset}}) = -\operatorname{acoth}(x_{\text{reset}})$. The period is found from the condition $-\coth(T + t_0) = +\infty$ resulting in $T = -t_0$. Hence, $x(t) = -\coth(t - T)$. Finally, $Q(\vartheta) = 1/(-1 + x(\vartheta)^2) = 1/(1 + \coth^2(\vartheta - T)) = \sinh^2(\vartheta - T)$.